BIOLOGICAL APPLICATIONS OF NANOPARTICLES PRODUCED BY LASER ABLATION METHOD

A DISSERTATION SUBMITTED TO

THE GRADUATE SCHOOL OF ENGINEERING AND SCIENCE

OF BILKENT UNIVERSITY

IN PARTIAL FULFILLMENT OF THE REQUIREMENTS FOR

THE DEGREE OF

DOCTOR OF PHILOSOPHY

IN

MATERIALS SCIENCE AND NANOTECHNOLOGY

By

Canan Kurşungöz

February 2017

Biological Applications of Nanoparticles Produced by Laser Ablation Method
By Canan Kurşungöz
February 2017

We certify that we have read this dissertation and that in our opinion it is fully adequate, in scope and in quality, as a dissertation for the degree of Doctor of Philosophy.

Bülend Ortaç(Advisor)

Mehmet Yıldırım Sara

Urartu Özgür Şafak Şeker

Şaban Remzi Erdem

Emine Yegan Erdem

Approved for the Graduate School of Engineering and Science:

Ezhan Karaşan
Director of the Graduate School

ABSTRACT

BIOLOGICAL APPLICATIONS OF NANOPARTICLES PRODUCED BY LASER ABLATION METHOD

Canan Kurşungöz
Ph.D. in Materials Science and Nanotechnology
Advisor: Bülend Ortaç
February 2017

Pulsed laser ablation in liquid (PLAL) is a promising top-down approach for nanoparticle production and it allows production of wide variety of nanoparticles such as metal, metal oxide, nitride and semiconductor nanocrystals. PLAL has numerous advantages compared to other nanoparticle production methods such as successful production of colloidal, pure and contamination-free nanoparticles. Pulsed laser ablation method was used for the production of a number of different nanoparticles both in liquids and gas environments. Moreover, both powder and bulk starting materials were employed for nanoparticle production. In the context of nanoparticle production and characterization, a systematic study for indium nitride nanocrystal (InN-NC) production was completed. The road-map for the production of ultra-smal hexagonall InN-NCs (<5 nm in diameter) was demonstrated to be produced from InN powder target in ethanol by using PLAL technique.

A real time nanoparticle exposure setup was designed and developed to reveal the health risks of laser material processing in the industry. In our study, adolescent rats were exposed to copper, tin and aluminum nanoparticles (CuNP, SnNP and AlNP, respectively) in the real-time exposure setup. We aimed to demonstrate the distribution of nanoparticles in the body by exposing the rats to the laser material processing environment. For this purpose, we defined the amount and characteristics of nanoparticles released during material processing by laser ablation. We also showed the effect of nanoparticles on learning-memory and mood of rats exposed to those nanoparticles via behavioral tests, electrophysiological and molecular methods. ICP-MS and TEM analysis revealed the presence of nanoparticles in almost all organs, including different regions of brain, indicating nanoparticles gained access to systemic circulation by inhalation. Both behavioral tests and in vivo electrophysiology experiments revealed that 3 months of CuNP, SnNP and AlNP exposure did not lead to any alterations in the learning and memory process of the rats. In hippocampi collected from rats

exposed to SnNP and AlNP, the expression levels of NMDA receptor subunits, namely NMDAR1 and NMDAR2a, were found to be increased, and the protein levels of NMDAR1 decreased upon CuNP exposure.

On the other hand, the toxicity of nanoparticles produced by pulsed laser ablation method in liquids was investigated for silver nanoaparticles (AgNPs) in hippocampal slices and CuNP, SnNP and AlNP nanoparticles in SH-SY5Y cell line in *in vitro* conditions. The cellular uptake mechanism of pure AgNPs was demonstrated as phagocytosis. Furthermore, AgNP led to dose-dependent toxicity in hippocampal slices. laser ablation is a considerably useful method for studying nanoparticle toxicity since it provides pure nanoparticles mimicking the ones encountered in the industry. Finally, it was shown that CuNP, SnNP and AlNP led to a dose-dependent cytotoxicity in SH-SY5Y cells. Moreover, it was shown that NMDAR subunits NMDAR1 and NMDAR2a mRNA expressions and NMDAR1 protein levels were altered after CuNP, SnNP and AlNP administration.

This study showed, for the first time in the literature, that the nanoparticles produced during the laser material processing in the atmospheric environment are taken into the body via inhalation. These nanoparticles are distributed to a number of organs including lung, heart, liver, kidney, testis and so on. Moreover, these nanoparticles were detected in different brain regions, which indicates the severity of the risk for the people working in these industrial fields. We did not observe significant alterations in behavioral and electrophysiological evaluations in 3 months. However, in long-term exposures, accumulation of nanoparticles in brain may impose a high risk for dementias and mental disorders since these nanoparticles are made up of heavy metals which were shown to cause neurodegeneration.

Keywords: Nanoparticle Generation, Nanotoxicity, Laser Ablation in Liquid, Laser Ablation in Atmospheric Environment, Laser Material Processing.

ÖZET

LAZER ABLASYON YÖNTEMİYLE ÜRETİLEN NANOPARÇACIKLARIN BİYOLOJİK UYGULAMALARI

Canan Kurşungöz
Malzeme Bilimi ve Nanoteknoloji, Doktora
Tez Danışmanı: Bülend Ortaç
Şubat 2017

Darbeli lazer ablasyonu nanoparçacık üretimi için sık kullanılan ve metaller, metal oksitler, nitritler ve yarı iletken nano kristaller gibi birçok farklı malzemenin üretilmesi için uygun bir yöntemdir. Darbeli lazer ablasyonunun diğer nanoparçacık üretim yöntemlerine göre birçok avantajı vardır. Koloidal, saf ve kontaminasyon içermeyen nanoparçacıkların üretimine olanak sağlaması avantajlarından birkaçı olarak sayılabilir. Bu yöntem, hem sıvı hem de hava ortamında çok çeşitli nanoparçacıkların üretilmesi için kullanılmıştır. Ayrıca, hem toz hem de katı hedefler nanoparçacık üretiminde başlangıç materyali olarak kullanılabilirler. Nanopartikül üretimi ve karakterizasyonu bağlamında, indiyum nitrit nanokristal (InN-NC) üretimi için sistematik bir çalışma tamamlandı. Yapılan çalışmada, küçük, altıgen InN-NC'lerinin (<5 nm) etanolde InN toz hedefi kullanılarak darbeli lazer ablasyonu yöntemi ile üretildiği gösterildi.

Endüstride lazerle malzeme işlemenin sağlık risklerini ortaya çıkarmak için gerçek zamanlı bir nanoparçacık maruziyet sistemi tasarlanmış ve geliştirilmiştir. Çalışmamızda, adölesan sıçanlar gerçek zamanlı maruziyet sisteminde bakır, kalay ve alüminyum nanoparçacıklara (sırasıyla CuNP, SnNP ve AlNP) maruz bırakıldı. Sıçanları lazerle malzeme işleme ortamına maruz bırakarak, bu esnada ortaya çıkan nanoparçacıkların vücuttaki dağılımını göstermeyi amaçladık. Bu amaçla, bu nanoparçacıkların miktarlarını ve özelliklerini belirledik. Ayrıca, bu nanoparçacıkların sıçanların öğrenme-bellekleri ve ruh halleri üzerindeki etkilerini davranışsal testler, elektrofizyolojik ve moleküler yöntemlerle gösterdik. ICP-MS ve TEM analizleri inhalasyon yoluyla vücuda giren nanoparçacıkların sistemik dolaşıma ve farklı beyin bölgeleri de dahil neredeyse tüm organlara ulaştığını ortaya koymuştur. Davranış testleri ve *in vivo* elektrofizyoloji deneyleri, 3 aylık CuNP, SnNP ve AlNP maruziyetinin, sıçanların öğrenme ve bellek sürecinde herhangi bir değişime yol açmadığını ortaya koymuştur. SnNP ve AlNP'ye

maruz bırakılan sıçanlardan alınan hipokampüs örneklerinde, NMDA reseptör alt birimleri olan NMDAR1 ve NMDAR2a'nın ekspresyon seviyelerinin arttığı, CuNPye maruz kalan sıçanların hipokampüs örneklerinde ise NMDAR1'in protein seviyesinin azaldığı gösterilmiştir.

Öte yandan, sıvılarda darbeli lazer ablasyonu yöntemi ile üretilen nanoparçacıkların toksisitesi, hippokampal dilimlerde gümüş nanoparçacıkları (AgNPs) ve *in vitro* koşullarda SH-SY5Y hücre hattında CuNP, SnNP ve AlNP nanoparçacıkları için araştırılmıştır. Çalışmamızda, saf AgNP'lerin hücresel alım mekanizması fagositoz olarak gösterilmiştir. Ayrıca, AgNPnin hipokampal dilimlerde doz bağımlı toksisiteye yol açtığı belirlenmiştir. Endüstride saf nanoparçacıklarla karşılaşıldığı için lazer ablasyonu nanoparçacık toksisitesini
incelemek için oldukça uygun bir yöntemdir. CuNP, SnNP ve AlNP'nin SH-SY5Y hücrelerinde doz bağımlı bir sitotoksiteye yol açtığı gösterilmiştir. Ayrıca, NMDAR alt birimlerinin NMDAR1 ve NMDAR2a mRNA ekspresyonlarının ve NMDAR1 protein seviyelerinin CuNP, SnNP ve AlNP uygulamasından sonra değiştiği gösterilmiştir.

Bu çalışmada, literatürde ilk defa, atmosferik ortamdaki lazerle malzeme işleme sırasında üretilen nanoparçacıkların inhalasyon yoluyla vücut içine alındığı gösterilmiştir. Bu nanoparçacıkların akciğer, kalp, karaciğer, böbrek, testis de dahil olmak üzere birçok organa ulaştığı gösterilmiştir. Ayrıca, bu nanoparçacıkların farklı beyin bölgelerinde tespit edilmesi endüstride lazer ile malzeme işleme alanlarında çalışan kişilerin ne kadar büyük risk altında olduğunu ortaya koymaktadır. Üç aylık maruziyet sonucunda davranışsal ve elektrofizyolojik değerlendirmede önemli değişiklikler gözlenmemiştir. Ancak, bu nanoparçacıklar nörodejenerasyona neden olduğu gösterilen ağır metallerden oluştuğu için, uzun süreli maruziyetlerde, nanoparçacıkların beyinde birikmesi demans ve zihinsel bozukluklar için yüksek bir risk oluşturabilir.

Anahtar sözcükler: Nanoparçacık, Nanotoksisite, Sıvı Ortamda Lazer Ablasyon, Atmosferik Ortamda Lazer Ablasyon, Lazer ile Malzeme İşleme.

Acknowledgement

The success and the existence of this PhD study depends not only on my efforts but also on the encouragement and guideness of many other people who were always with me in this long and challenging way. Firstly, I would like thank my advisor Assist. Prof. Dr. Bülend Ortaç for his support, encouragement, guidance, and supervision. Also, I would like to express my gratitude to Prof. Dr. Yıldırım Sara for his contribution, useful advice and guidance throughout this thesis study. Besides, I would like to thank the rest of my thesis committee; Assist. Prof. Dr. Urartu Özgür Şafak Şeker, Prof. Dr. Şaban Remzi Erdem and Assist. Prof. Dr. Yegan Erdem for their insightful comments and encouragement. I would also like to acknowledge Prof. Dr. Mustafa F. Sargon due to his collaboration and support in the TEM analysis of tissues.

A number of people from Ortaç Research Group were always with me through my long journey. I would like to thank my current labmates Elif Uzcengiz Şimşek, Bartu Şimşek, Yakup Midilli, Uğur Teğin and Levent Ersoy for their friendship and support in my experiments. Moreover, I am greatful to the former lab members Elif Gül özkan Arsoy, Fehmiye Keleş Yıldız, Merve Yağmur Yardımcı, Refik Tuzaklı, Ahmet Sönmez and Orhun Kaya for their encouragement, support, and deep friendship for all these years. Apart from Ortaç Research Group, the members of Sara Lab Sadık Taşkın Taş, Barış Alten and Metin Yeşiltepe, we run a long way together and I am thankful for you not only being my labmates but also my supportive friends.

A number of engineers in National Nanotechnology Research Center (UNAM) helped in my thesis studies; I would like to thank to Mustafa Güler for his help in TEM, Dr. Gökçe Çelik and Seda Kutkan for their support in ICP-MS, Zeynep Erdoğan for her training in zeta potential measurements and Enver Kahveci for his help in XPS analyses. I would like to express my gratitude to Assist. Prof. Dr. Ebru Erbay for giving me the opportunity to use her lab facilities. Moreover, I would also like to thank Erbay group members for their friendship and support during my studies in their lab.

I would like to thank to Deniz Sezlev Bilecen and Dr. Menekşe Ermiş Şen who were always there for me with their deep friendship and encouragement in these

difficult days. We started to this long journey together and we came to the end together, thank you Melike Sever and Gülistan Tansık for your friendship and support during these years. My deepest gratitude is for my dearest friend Dr. Gülhas Solmaz. Although she was far away from me, her supportive and relaxing calls meant a lot for me.

I would like to express my special thanks to Dr. Tolga Bağcı for his deep love, patience, endless scientific and emotional support and friendship. Since the first day, you are the happiness on my face. I would also like to thank to İnci Bağcı for keeping the house always open for me and her support.

I am indebted to my parents Kadriye and Hüsnü and my dear sister Candan for their unconditional support, patience and love throughout my life and my education. Although we were all in different cities during this PhD study, I always felt their support and love in my heart. Thus, this thesis is dedicated to my dear family.

I would like to acknowledge UNAM for using the infrastructure, TÜBA-GEBİP and The Scientific and Technological Research Council of Turkey (TÜBİTAK) for funding this research with the project 113S223 and providing me scholarship in Doctorate Fellowship for prior research theses 2211-C.

Contents

List of Figures

List of Tables

Chapter 1

Introduction

Pulsed laser ablation in liquid (PLAL) is a promising top-down approach for nanoparticle production and it allows production of wide variety of nanoparticles such as metal, metal oxide, nitride and semiconductor nanocrystals [2, 3]. Moreover, PLAL has numerous advantages compared to other nanoparticle production methods [4]. It leads to successful production of colloidal, pure and contamination-free nanoparticles [5, 6]. In this thesis, pulsed laser ablation was shown to be a suitable method for the production of a number of different nanoparticles both in liquids and gas environment. Furthermore, both powder and bulk starting materials were employed for nanoparticle production. In one of these studies, ultra-small hexagonal InN-NCs (<5nm in diameter) was shown to be produced from InN powder target in ethanol by using PLAL technique. Lower laser energy and lower ablation duration were demonstrated to result in much smaller nanoparticles.

Besides the production and characterization of nanoparticles, the toxicological effects of them were also represented throughout this study. Nanoparticles were shown to be produced as a result of various methods applied in industry, and one of the most important examples of these methods is cutting or drilling of materials using lasers [7]. As these nanoparticles are able to move freely in the

air, workers are exposed to these nanoparticles constantly. Materials used in industry are mostly comprise heavy metals such as nickel and lead, and processing of these materials causes the release of nickel and lead nanoparticles. Respiration of these nanoparticles by the workers poses a great danger on health of the workers. Blood brain barrier (BBB) was shown to be disrupted upon nanoparticle exposure, which indicates the potential risk of these nanoparticles in the industry on central nervous system [8]. Firstly, real time nanoparticle exposure setup was designed by using a nanosecond laser marking system and rats were exposed to material processing environment where copper, tin and aluminum plates were marked for 3 months. To our knowledge, this is the first time in the literature using this kind of real time exposure setup, mimicking the real industrial working environment, for the investigation of nanoparticle distribution in the body. At the end of the exposure period, the effect of these nanoparticles on the learning and memory process were analyzed with behavioral tests, electrophysiology experiments and molecular analyzes. It was shown that CuNP, SnNP and AlNP were produced in the environment during the marking of respective metal plates. Both behavioral tests and *in vivo* electrophysiology experiments revealed that 3 months of CuNP, SnNP and AlNP exposure did not lead to any alterations in the learning and memory process of the rats. However, it was demonstrated that N-methyl-D-aspartate receptor (NMDAR) subunits NMDAR1 and NMDAR2a mRNA expressions were significantly increased in SnNP and AlNP exposed groups. Moreover, NMDAR1 protein levels were shown to decrease after CuNP and SnNP exposure compared to controls. It might be concluded that CuNP, SnNP and AlNP produced during laser materials processing might lead to changes in mRNA and protein levels of NMDAR after three months of exposure. Although this change was not reflected to the synaptic transmission and behavior, it might be suggested that in long term exposure there is a high risk to alter the learning and memory functions, together with neurodegeneration.

Cu, Sn and Al were also analyzed in terms of body distribution after 3 month of exposure with the real time laser material processing setup. These nanoparticles were detected in a number of organs throughout the body upon inhalation. The lack of these elements in the intestine demonstrates that the route of exposure

was only inhalation, but not digestion. Lungs, the primary target organs after the inhalation, were detected with the high element concentrations indicating the accumulation of these nanoparticles in the lungs. The nanoparticles also reached to a number of organs through systemic circulation, such as heart, liver, kidney, spleen, and testis. Moreover, nanoparticles were shown to reach a number of brain parts either by passing through the BBB or via olfactory bulb. The body distribution results indicate that nanoparticles produced during laser materials processing might lead to a number of health risks in human upon inhalation. These significant results reveal the high risk of the nanoparticles generated during the laser material processing for the people working in these industrial fields. Besides the risks for a number of organs, detection of these nanoparticles in different brain parts shows the severity of risk in terms of neurodegeneration and the apoptosis of neuron cells

On the other hand, the distribution and the toxicity of the pure AgNPs produced by laser ablation method was also demonstrated in the rat hippocampal slices. The cellular uptake mechanism of pure AgNPs was demonstrated to depend on their sizes. No AgNPs were detected in synaptic vesicles following stimulation of synaptic vesicular recycling, thus, it was concluded that phagocytosis is the type of endocytotic pathway that dominates the entry of pure AgNPs into the hippocampal neurons. Moreover, AgNP led to dose-dependent toxicity in hippocampal slices. The data provide significant information for the further cellular and molecular research about the neurotoxicology of nanoparticles since exposure to silver nanoparticles might result in neurodegeneration. Furthermore, this study showed that laser ablation is a considerably useful method for studying nanoparticle toxicity since it provides pure nanoparticles mimicking the ones encountered in the industry.

Finally, the effects of CuNP, SnNP and AlNP exposure were studied on SH-SY5Y human neuroblastoma cell line for the first time in the literature. It was shown that these nanoparticles led to a dose-dependent cytotoxicity in SH-SY5Y cells. Moreover, it was shown that NMDAR subunits NMDAR1 and NMDAR2a mRNA expressions and NMDAR1 protein levels were altered after CuNP, SnNP and AlNP administration.

Chapter 2

Nanoparticle Production with Pulsed Laser Ablation Method

2.1 Introduction

In this chapter, pulsed laser ablation mechanism will be introduced. The use of pulsed laser ablation for the nanoparticle production both in the liquid and in the atmospheric environment will be presented together with experimental results.

2.1.1 Pulsed Laser Ablation Method

When materials are 100 nm or smaller, characteristics due to this nano-scale size become evident. Due to the changes of physicochemical properties of particles when they reach to nanoscale dimensions, they exhibit different characteristics than their bulk counterparts. While these changes allowed the nanotechnology field to grow rapidly with the wide range of advantages of nanoparticles used in various fields from electronics to biomedicine, the effects of particles on the human health are also significantly different than the bulk materials [9]. Nanoparticles, basically, are examined in two groups. The first group consists of nanoparticles

produced in laboratory environment for a specific aim, and the second group consists of nanoparticles generated in the environment or industry incidentally. Nanoparticles of the first group can be produced by various physical and chemical methods [10]. One of these methods is the method of nanoparticle production with pulsed laser ablation. With pulsed laser ablation method, nanoparticles can be used in different environments, namely solid, liquid and gas. The most important advantage of this method is the capability of producing pure nanoparticles as no chemical agent is used during the production. In other words, this method is free from any chemical agent, which ensures that nanoparticles can be produced more simply and more easily compared to other methods. Another advantage is that a wide variety of materials (namely metals, semiconductors, alloys and magnetics materials) can be processed with this method to produce nanoparticles. However, the size distribution of the nanoparticles produced by pulsed laser ablation method is in a wide range from a few nanometers to microns, which might be accepted as the disadvantage of this method [11].

2.1.2 Mechanism of Pulsed Laser Ablation Method

During the ablation of a solid target in a liquid environment, a number of consecutive processes are observed. Firstly, as a result of reaching the laser light to the solid target, the plasma plume is generated. After the plasma plume generation, it is transformed and condensed. The plasma plume is significantly affected from the liquid confinement due to its thermodynamic and kinetic properties. The liquid confinement results in the shock wave formation due to the adiabatic expansion of the laser-induced plasma at a supersonic velocity in the plasma plume. The material is removed from the solid target in a continuous manner as a result of vaporization because of the incoming laser pulse. The shock-wave leads to the induction of an extra pressure in the laser-induced plasma and it is called plasma-induced pressure. Meanwhile, the temperature in laser-induced plasma increases. As a result, the thermodynamic state of the laser-induced plasma changes to the state with higher temperature, higher pressure and higher density, which allows the formation of the metastable phases [12].

Four types of chemical reactions are detected in the laser-induced plasma and the interface between the liquid and the laser-induced plasma while it is in the transformation process. The first reaction is observed inside the laser-induced plasma owing to the high temperature and high pressure state of the laser-induced high-density plasma and new phase can originate by these chemical reactions between the ablations from the target. The second reaction occurs inside the laser-induced plasma, again. This time, the liquid molecules at the interface are excited and evaporated due to the high temperature and high pressure in the laser-induced plasma. Therefore, a new plasma from the liquid molecules are formed at the interface, which is called plasma-induced plasma. The laser-induced plasma and plasma-induced plasma are mixed and the laser-induced plasma includes a number of species from the plasma-induced plasma inside. The species generated from the laser ablation of the target and the species formed due to the excitation of the liquid molecules are engaged in the chemical reactions in this part. The third chemical reaction occurs at the interface of the laser-induced plasma and the liquid due to the high temperature, pressure and density. The forth reaction is observed inside the liquid when the ablated species from the solid target is affected by the high pressure of laser-induced plasma. In the chemical reactions where two species, namely the ones from the solid target and the ones from the confining liquid, are involved, the generation of new materials in nanoscale by the combination of the target and the liquid takes place. Finally, the plasma plume cools down and condenses in the confining liquid in two different ways. It can either condenses and deposits back on the target solid or condenses and become dispersed in the liquid by forming nanoscale materials [12]. When we explain the nanoscale material formation mechanism in detail, we should first assume the clusters and the surrounding plasma have the same temperature T, then isothermal nucleation time is given by;

$$\tau = \sqrt{2\pi \mathrm{mkT}} \times \frac{\mathrm{kT}\gamma}{p_s(T)(\Delta\mu)^2)} \tag{2.1}$$

where m is the mass of a single atom, k is the Boltzmann's constant, T is the absolute temperature, γ is the surface energy density of the material, $p_s(T)$

is saturated vapor pressure of nuclei at the temperature of T, and $\Delta\mu$ is the atom chemical potential difference. With the decrease in the nucleation time, the pressure is elevated. However, the temperature and the nucleation time are inversely related to each other because of the saturated vapor pressure effect of nuclei. Thus, the diameter of nanomaterials could be expressed as;

$$d = V(2\tau_d - \tau) + 2r^* \tag{2.2}$$

where τ_d and r^* are the laser pulse duration and the size of critical nuclei of the material, respectively. These theoretical calculations were also shown to be in good agreement with the experimental results [13, 12].

2.2 Nanoparticle Production with Pulsed Laser Ablation in Liquids

Throughout the thesis study, a number of different nanoparticles (silver, gold, titanium, $MoSe_2$ and so on)were produced by pulsed laser ablation method in liquid both from solid and powder targets for different applications [14, 15, 16]. Besides, a recent study was conducted, in which indium nitride nanocrystals were produced.

The promising optoelectronic properties of Group III nitrides (InN, GaN, AlN) led to an increasing attention due to their potential applications [17]. Among them, due to its smallest effective mass, high electron mobility, superior electron transport properties and direct band gap structure, InN is a promising candidate for high speed optoelectronic devices, broad-spectrum solar cells, high electron mobility transistors, near infrared light emitting diodes (LEDs) and high speed laser diodes [18, 19, 20]. Furthermore, its nontoxic nature and infrared emission properties enable InN to be used in biological and medical applications [21]. Besides these advantageous properties of InN material, its nanostructures have

been widely studied due to their different characteristics depending on the dimensionality and size, which allow the applications in nanoscale electronic and optoelectronic devices [22, 23]. InN crystallizes in two different structures; stable hexagonal (wurtzite) structure and metastable cubic structure. When compared to hexagonal InN, cubic InN possesses smaller band gap and superior electronic properties due to its isotropic lattice and lower phonon scattering [24]. However, the production of cubic InN-NCs is quite a challenging process due to its thermodynamically unstable nature [25]. Previous studies showed a number of techniques viable for the synthesis of InN-NCs mainly having hexagonal structure. Ambient pressure and low temperature liquid phase was proposed as a suitable method for the synthesis of nanoparticles having low decomposition temperatures. It was shown that wurtzite InN-NCs having 6.2 nm average diameter are successfully produced using this method. These colloidal wurtzite InN-NCs were post-treated with nitric acid to get rid of the metallic indium byproduct and finally InN nanopowder was obtained [26]. Moreover, activated reactive evaporation and nitrogen plasma annealing methods were proposed for the successful production of wurtzite InN-NCs and InN nanorods, respectively. It was suggested that the technique is applicable to produce InN-NCs by using low temperatures from indium nanostructures obtained by different techniques [27]. Xiao et al. demonstrated the synthesis of 10 30 nm InN-NCs from sulfide precursor using a novel thermal conversion method at low temperatures and suggested that this method can be applied for the production of all group III nitrides [28]. The synthesis of wurtzite InN nanobelts was also performed by using guided-stream thermal chemical vapor deposition (GSCVD) technique [4]. Qaeed et al. proposed a chemical synthesis method not requiring high temperatures for large-scale nanoparticle production. These InN-NCs were shown to be cubic in structure and to have a grain size between 11.4 and 21.4 nm [29]. On the other hand, rapid thermal ammonolysis was shown as a method for production of InN-NCs in hexagonal crystal structure [30]. Single crystalline InN-NCs having an average diameter of 15 nm and hexagonal structure were successfully produced using vapor-liquid-solid process [31]. Furthermore, single-crystalline hexagonal structured InN-NCs having 9.8 36.0 nm grain size were obtained by the reaction of InI3 and NaNH2 in benzene-thermal system [32]. In recent years, the most commonly used method is the production

of nanoparticles in liquids by using pulsed laser ablation. The most important advantage of this method is that it does not require the use of vacuum systems. Since nanoparticles are trapped in the liquid, this method is cheaper and easier to proceed when compared to other methods. In pulsed laser ablation method, high energy laser beams pulsing with nano- or femtoseconds are focused on materials inside the liquid and make the material transform to its plasma form, creating ions and electrons via very high temperatures produced in this liquid environment or direct ionization of the material itself (Figure 2.1) [33]. As the plasma form of the material is getting cooler in the liquid environment, nucleation of ions and electrons yields nanoparticles [34]. Highly pure nanoparticles produced with this method are used in various fields of nanotechnology field such as sensors, transistors and biology [35]. As produced nanoparticles are trapped in the liquid environment, they do not pose any hazard. Our group previously showed that pulsed laser ablation in liquid (PLAL) is a suitable method for the production of InN-NCs with hexagonal crystalline structure. Colloidal InN-NCs were produced in ethanol by ablating the HPCVD-grown InN thin film sample with different energies using a nanosecond pulsed laser. The average diameter of the produced InN-NCs was 10 nm [36]. These InN-NCs were shown to have applications such as a near infrared range photodetector [37] and charge trapping memory cells [38]. However, the starting material was HPCVD-grown InN thin film and the starting material, either a bulk target or a suspension, affects the final nanoparticle size in PLAL. It was previously shown that pulsed laser ablation of suspensions results in much smaller nanoparticle sizes compared to the ablation of bulk target. It was suggested that the particles in the suspension absorb all the laser energy since the particles encounter multiple pulses during all the ablation process due to continuous stirring. On the other hand, the laser energy is absorbed only by the target in case of ablation of bulk target and results in larger nanoparticles. Furthermore, the particle size of the nanoparticles at the end of the ablation process depends on the initial size of the suspended particles [39, 40].

In this study, we aimed to produce ultra-small InN-NCs by using suspension of micron-sized InN powder in ethanol with PLAL method and, to our knowledge, we reached the smallest nanocrystal size for InN-NCs in the literature. For

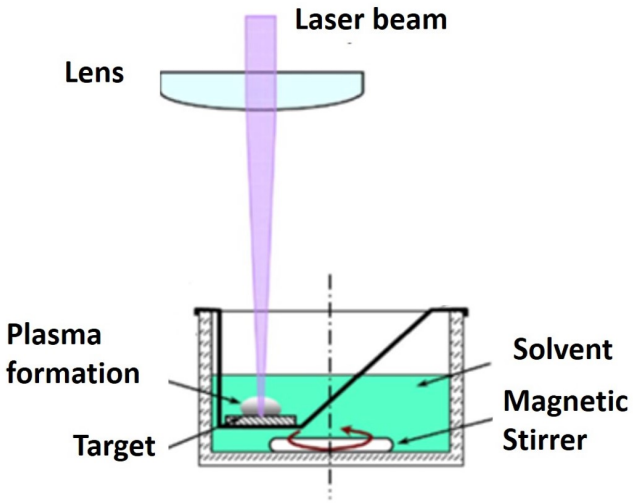

Figure 2.1: Nanoparticle production setup with pulsed laser ablation method in liquid. Adapted from [33]

this purpose, we performed series of PLAL processes with different solvents (isopropanol, ethanol and water), different laser energies (3 mJ, 4 mJ and 5 mJ) and different ablation times (up to 300 min). The formation of InN-NCs was confirmed by using scanning electron microscope (SEM) and transmission electron microscope (TEM). Moreover, we used X-ray diffraction (XRD) to confirm the crystal structure of InN-NCs. Absorption, zeta potential and RAMAN analyses were performed for further characterization of the nanocrystals. We showed that formation mechanism of InN-NCs was through pulsed laser fragmentation and melting by analyzing the SEM. We successfully demonstrated the presence of fragmented/molten particles and nanoparticles in the SEM images. Moreover, the hexagonal crystalline structure of the powder target was preserved after the nanoparticle formation. Overall, we proposed a roadmap for the generation of ultra-small (<5 nm) InN-NCs by combination of PLAL and suspension of micron-sized target after optimizing the laser parameters such as liquid environment, laser ablation time, laser energy and applying centrifugation with appropriate time and speed as a post-synthesis treatment.

2.2.1 Materials and Method

2.2.1.1 Nanocrystal Synthesis

InN-NCs were generated by using a commercial nanosecond pulsed ND:YLF laser (Empower Q-Switched Laser, Spectra Physics) operating at 527 nm with a 100 ns pulse duration and 1 kHz repetition rate. InN target was purchased as powder (Santa Cruz Biotechnology, USA) and 1 mg powder was dissolved in 10 ml of pure solvent (isopropanol, ethanol and water). To obtain a well dispersed InN-NC solution, the colloidal nanomaterial solution was continuously stirred by a magnetic stirrer at 1000 rpm during the laser ablation process. The colloidal solution was light orange after nanoparticle formation for all experiments. In all laser ablation procedures, the laser beam was focused on InN solution by the help of a plano-convex lens with a focal length of 50 mm. The laser power for the ablation process varied in different processes as 3W, 4W and 5W with corresponding pulse energies of 3mJ, 4mJ and 5mJ, respectively. As another parameter to test, different ablation durations starting from 1 min to 300 min were studied. 15 minutes of centrifugation at 4.000 xg was also performed for two samples obtained with 3mJ pulse energy (15 and 60 min ablation time) to make the nanocrystals smaller than 5 nm isolated in high resolution TEM (HR-TEM) images.

2.2.1.2 Nanocrystal Characterization

Different characterization methods were utilized throughout this study. The high-resolution transmission electron microscope (HR-TEM) imaging of the InN-NCs was carried out by using the FEI-Tecnai G2 F30 TEM instrument at an operating voltage of 300 kV. All samples were prepared by drop-casting the solutions onto separate carbon-coated TEM grids. Each histogram data were obtained by counting 100 particles from the TEM images and using Image J Image Processing and Analysis software. The morphology and the time course of the nanoparticle generation was monitored by using scanning electron microscope (SEM, Quanta

200 FEG, FEI Instruments, USA). For the stability analyses, zeta potential measurement was carried out (Malvern Instruments Ltd, Malvern, UK). Absorption analysis of the InN-NCs was performed in 200 nm 800 nm range (Varian Cary 100 UV/Vis spectrophotometer). To determine the crystalline structure and the composition of the InN-NCs, X-ray diffraction (XRD) analysis was performed (PANalytical XPert PRO multipurpose diffractometer, Netherlands). The operation voltage was 45 kV and the current was 40 mA with a CuK radiation source. The sample was prepared by depositing and drop-casting the InN-NCs on quartz substrate. Raman spectroscopy was performed by using a Witec Alpha 300S Micro Raman spectrometer with a Nd:YAG laser at an excitation wavelength of 532 nm (laser power: 10 mW, laser spot size $\approx$ 4 m, unpolarized) and a Nikon 100x (N.A. = 0.9) air objective. The integration time was 1.035 second and we obtained the data in 3.5 hours. The sample was dropcasted onto a Si substrate with $< 111 >$ orientation.

2.2.2 Results and Discussion

2.2.2.1 Stability issue of InN-NCs in different solvents

Stability of the produced nanoparticles is a challenging issue and PLAL has the advantage of production of stable nanoparticles even without using any stabilizers or surfactants [41]. It was shown that the solvent plays a significant role in the stability of produced nanoparticles with PLAL [42]. Thus, we first aimed to determine the most appropriate solvent in which InN-NCs is stable. For this purpose, we used ethanol, isopropanol and distilled water and performed laser ablation for 30 minutes at 3mJ laser energy. SEM (Figure 2.2a, b, c) and TEM (Figure 2.2d, e, f) images showed that InN-NCs smaller than 50 nm were successfully produced in all of three solvents and no aggregation was observed in freshly synthesized samples. Although the nanocrystals seem to be aggregated in TEM figures, they are isolated nanoparticles in the solution. Since drop-casting method is used in the TEM sample preparation, these nanocrystals prefer to stay together during evaporation of the solvent. Therefore, the nanocrystals TEM

images might appear as they are aggregated. On the other hand, zeta potential measurement of these samples (Figure 2.3) demonstrated that InN-NCs produced in ethanol has the highest zeta potential value (42.40 ± 1.08 mV) compared to the InN-NCs in isopropanol and water (37.73 ± 5.38 mV and 35.83 ± 1.48 mV, respectively). Thus, ethanol was determined as the most appropriate solvent for InN-NCs to be produced in terms of stability.

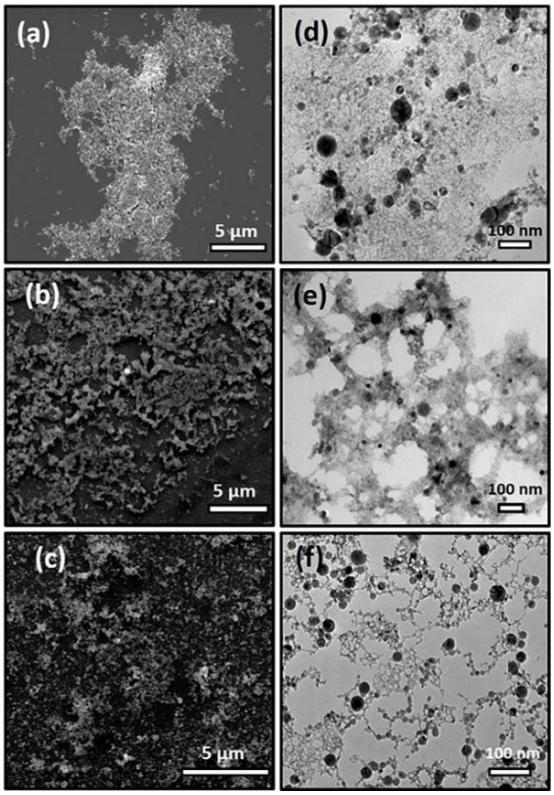

Figure 2.2: SEM and TEM images of InN-NCs produced in (a, d) ethanol, (b, e) isopropanol and (c, f) water. InN-NCs smaller than 50 nm were successfully produced in all of three solvents.

2.2.2.2 Effects of laser energy and ablation duration on InN-NCs

Laser energy was shown to be a significant parameter for nanoparticle production with PLAL method, specifically for the size distribution of the nanoparticles [43]. Hence, we focused on the effect of laser energy on the InN-NC particle size. 3 mJ, 4 mJ and 5 mJ laser energies were investigated in 60 minute ablation

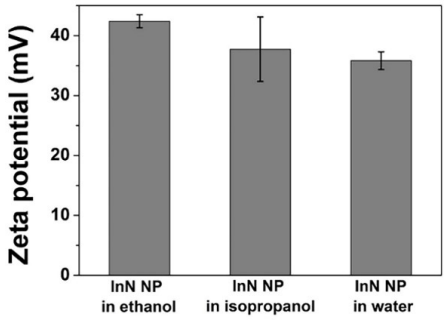

Figure 2.3: Zeta potential graph for InN-NCs produced in ethanol, isopropanol and water. Zeta potential values were 42.40 ± 1.08 mV, 37.73 ± 5.38 mV and 35.83 ± 1.48 mV for the InN-NCs produced in ethanol, isopropanol and water, respectively. The most stable InN-NCs were produced in ethanol.

duration. TEM images were obtained for InN-NCs produced with each laser energy (Figure 2.4 a, b, c) and the average diameter of InN-NCs was calculated using the histogram data (Figure 2.4 d, e, f). The histogram data were obtained by measuring the diameters of single isolated InN-NCs from the TEM images. The smallest mean size of the InN-NCs was observed with in ablation with 3 mJ laser energy (10.84 ± 0.71 nm) while ablation with 4mJ and 5mJ resulted in 16.27 ± 0.68 nm and 16.06 ± 0.59 nm, respectively. Thus, smaller InN-NCs were obtained by using lower laser energy in ablation procedure. In a previous study, we showed that the lower pulse energies with nanosecond laser ablation of InN thin-film led to a decrease in the nanoparticle size distribution but the smaller nanoparticles were obtained with larger energies [37]. The target material has a great importance since the laser pulse with higher energy result in much more ablation process on the solid target while the increase in the energy did not affect the nanoparticle sizes after a certain value with the continuously stirred sample powder sample.

It was demonstrated that nanoparticles start to aggregate and precipitate when the ablation duration increases [44]. Therefore, we used different laser ablation durations at 3mJ laser energy to optimize the ablation duration and to observe the formation mechanism of InN-NCs. SEM images were analyzed in terms of ablation durations (5, 15, 30, 60, 90, 120, 180 minutes) (Figure 2.5 b-h) starting from the InN powder samples consisting of micron sized InN flakes (Figure

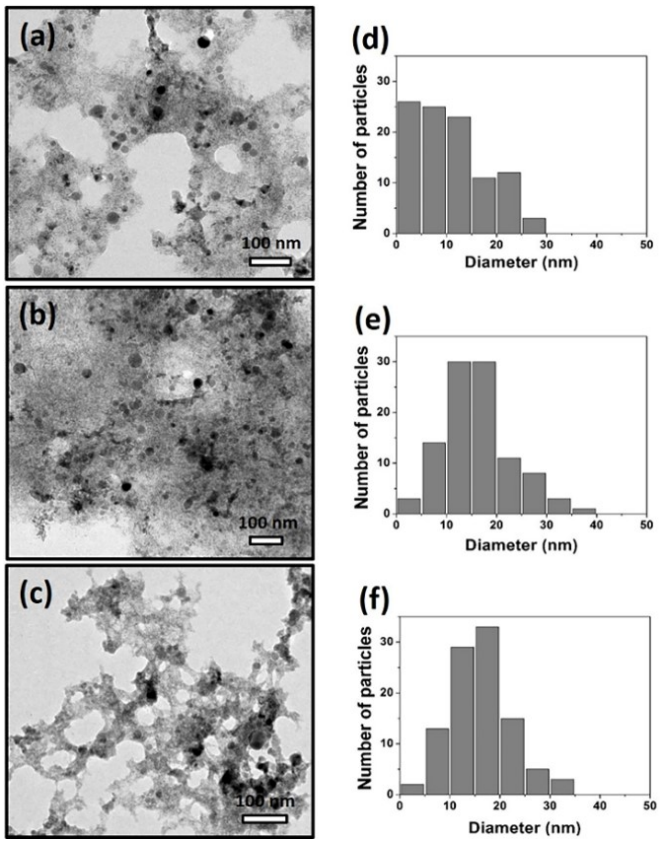

Figure 2.4: TEM images and histogram data of InN-NCs produced with (a, d) 3mJ, (b, e) 4mJ and (c, f) 5mJ laser energies. The average InN-NC diameters were determined as 10.84 ± 0.71 nm, 16.27 ± 0.68 nm and 16.06 ± 0.59 nm for the laser energies of 3mJ, 4mJ and 5 mJ, respectively. 3mJ laser energy resulted in the smallest nanoparticle diameter and narrower size distribution

2.25a). When laser interacted with the InN powder, it caused melting in the interacted area. On the other hand, increased temperature in the non-interacted area resulted in formation of nanoparticles and molten particles on the powder surface as shown in the inset of Figure 2.5b. Nanoparticle production began at 15 minutes ablation duration. The SEM image of 15 min ablated sample clearly showed that there were also fragmented particles together with molten spherical particles. Furthermore, with increasing ablation durations, firstly micron particles (powder, fragmented, molten particles) disappeared and nanoparticles seemed to be decreasing in size. However, the decrease in size led to aggregation after 60 minutes ablation.

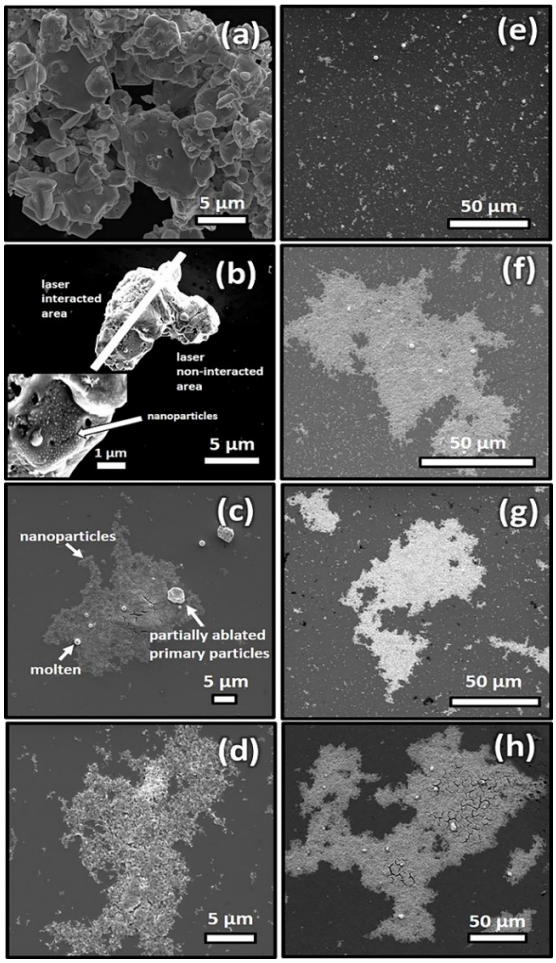

Figure 2.5: SEM images of InN (a) powder, and nanoparticles after (b) 5 min, (c) 15 min, (d) 30 min, (e) 60 min, (f) 90 min, (g) 120 min and (h) 180 min ablation durations.

After a topographical analysis with SEM, TEM images were obtained to evaluate the size distribution of the InN-NCs. As depicted in TEM images (Figure 2.6a-d), we obtained smaller nanoparticles with a narrower size distribution with increasing ablation duration. This was also confirmed with the aforementioned SEM analysis. However, after 15 minute ablation, the size distribution got broader and the mean size of the InN-NCs increased. This might be because of the fact that the smaller the nanoparticles, the more aggregation is observed. The micron sized particles were not included in the histogram analysis for 15 min ablation process.

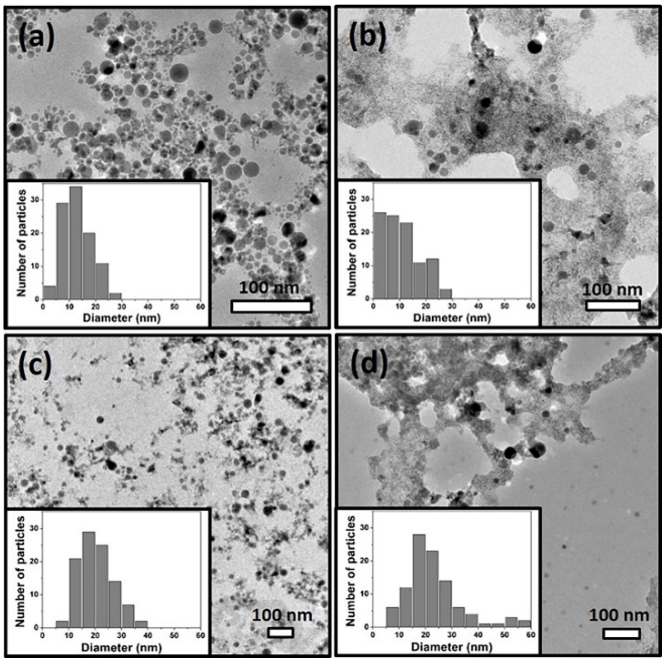

Figure 2.6: TEM images of InN-NCs at (a) 15 min, (b) 60 min, (c) 120 min, (d) 180 min laser ablation durations. As the ablation duration increases, the size distribution of the InN-NCs increases.

2.2.2.3 Post-synthesis treatment

One of the interesting property of InN-NCs is the optical behavior of nanoparticles produced with different ablation times that lead to different particle sizes. To analyze the optical properties of InN-NCs, we further determined the absorption behavior in UV-Vis spectra from 200 nm to 800 nm (Figure 2.7). InN-NCs demonstrated an increased absorption intensity in two main UV regions (200 nm and 300 nm) after 15 min ablation time. When the ablation duration increased, the intensity in the spectra increased since the concentration of the nanoparticles increased. On the other hand, the shoulder of the peak in 300 nm region became more pronounced after 60 min ablation due to the aggregation of the nanoparticles. This aggregation led to larger nanoparticle size and a red shift in the UV-Vis spectra. We further analyzed the optical behavior of nanoparticles up to 300 min and observed that there was no significant change on the optical behavior providing the stable particle sizes.

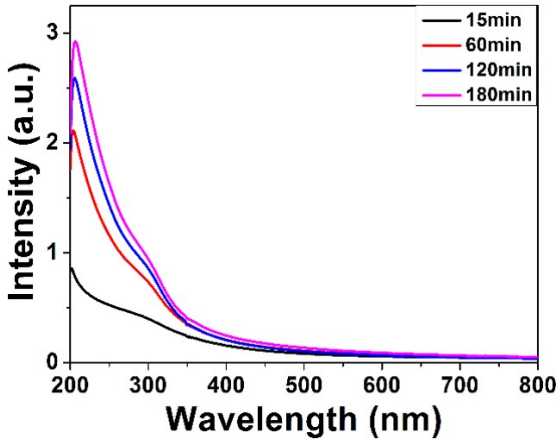

Figure 2.7: Absorption of InN-NCs produced at different ablation durations. The intensity throughout the UV region increases with increasing ablation duration. Moreover, the aggregation of InN-NCs after a certain ablation duration, namely 60 min, leads to a shoulder with a red shift in the peak at around 300 nm (a.u.: arbitrary units in all figures).

Although we were able to obtain the histogram data, much smaller nanoparticles distinguished by TEM images (Figure 2.6) might not be easily detected in UV-Vis spectra due to the larger nanoparticles. To determine the size and behavior of these smaller nanoparticles, we used centrifugation technique. For this purpose, we focused on two different ablation durations, 15 minutes and 60 minutes. After the centrifugation process, we checked the absorption behavior of the nanoparticles (Figure 2.8a and b). When compared to the samples before centrifugation, the spectra shifted to UV region demonstrating that centrifugation process was successful in selecting the smaller nanoparticles. The intensity also decreased for the InN-NCs produced at 60 min laser ablation duration, which might be due to the unoptimized centrifugation process. However, zeta potential analysis (Figure 2.8c) revealed that when the samples were centrifuged, the stability was conceded since the zeta potential values decreased after centrifugation. The decrease in the stability is consistent with the previous data indicating that smaller nanoparticles have the tendency of faster aggregation [45].

Moreover, as discussed previously, the centrifugation of 60 min ablated sample resulted in a higher zeta potential value when compared to that of 15 min ablated and centrifuged sample. This is also consistent with the size analysis since 15 min

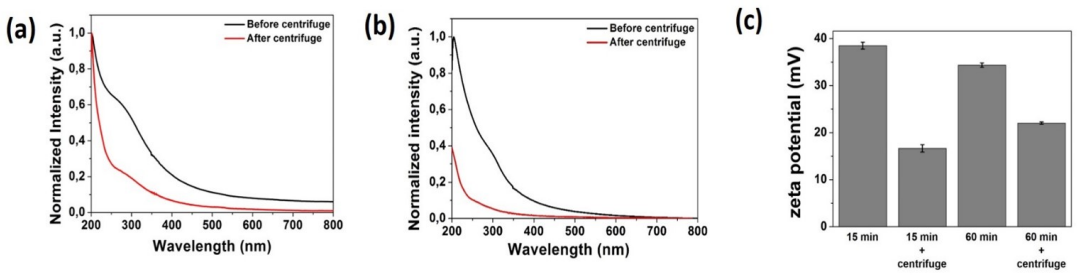

Figure 2.8: Absorption of InN-NCs produced at (a) 15 min and (b) 60 min ablation duration before and after centrifugation. Centrifugation process results in the elimination of the larger nanoparticles in the colloidal suspension, thus leading to the disappearance of the peak around 300 nm wavelength. Smaller nanoparticles display the absorption through the UV region. (c) The zeta potential values of InN-NCs produced at 15 min and 60 min ablation duration before and after centrifugation. The zeta potential of InN-NCs produced at 15 min and 60 min ablation duration are 38.5 ± 0.72 mV and 34.36 ± 0.46 mV, respectively. However, after centrifugation the zeta potential values decreased to 16.66 ± 0.79 mV and 22.03 ± 0.24 mV for the nanoparticles produced at 15 min and 60 min ablation duration, respectively.

ablation led to much smaller InN-NC sizes and a faster aggregation as inferred from the zeta potential values. To obtain a more stable colloidal nanoparticle solution produced by PLAL, it was suggested in some previous studies that surfactants and stabilizers can be used [46, 47]. TEM and HR-TEM images were obtained for 15 minutes and 60 minutes ablated samples (Figure 2.9). TEM data showed that after centrifugation, much smaller InN-NCs, which were previously observed as a background, became noticeable due to the disappearance of larger nanoparticles. Moreover, it was demonstrated with HR-TEM analysis that the InN-NCs had crystalline structure. Both single crystalline and polycrystalline InN-NCs were observed in TEM analysis. The HR-TEM image of the single crystalline InN-NC in the inset of Figure 8c reveals the crystalline lattice fringes having a lattice spacing of 0.28 nm, corresponding to (002) plane of hexagonal InN-NC [32, 36, 48]. TEM images from centrifuged samples allowed us to determine the size of nanoparticles smaller than 5 nm. The histogram analysis (Figure 2.10) showed that we obtained InN-NC smaller than 5 nm in both 15 minutes and 60 minutes ablated samples.

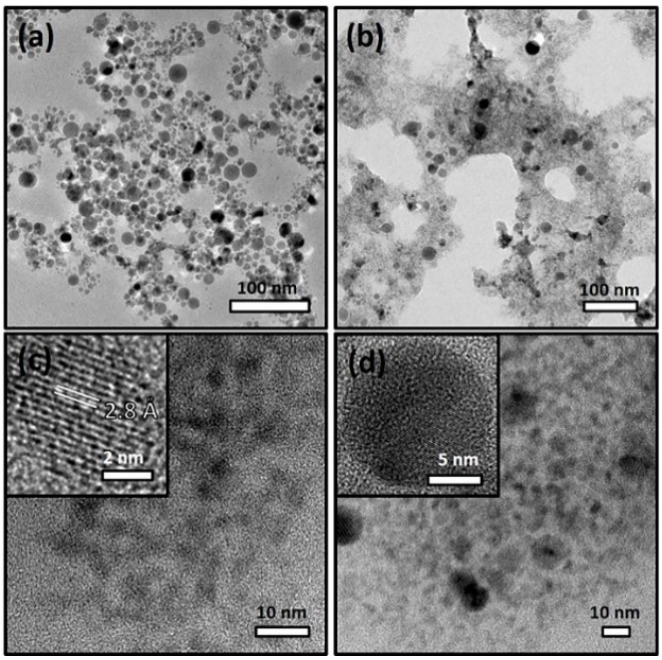

Figure 2.9: TEM images of InN-NCs produced at (a) 15 min and (b) 60 min laser ablation durations. To determine the size of InN-NCs smaller than 5 nm, a centrifuge process was performed and TEM images of the centrifuged samples of (c) 15 min and (d) 60 min ablated InN-NCs are represented. The inset images demonstrate the crystalline structure of InN-NCs. The 0.28 nm lattice fringe confirms the (002) plane of hexagonal InN-NC.

2.2.2.4 Crystal structure analysis

After the InN NCs were confirmed to be in crystalline form from the HR TEM images, we studied the crystal structure in detail by using XRD. XRD analysis results of the powder target, 15 minutes and 60 minutes ablated samples are shown in figure 2.11. The peaks of 15 minutes and 60 minutes ablated samples at two theta degrees of 28.92, 31.14, 32.96, 36.10, 43.13, 51.46 and 56.82 indicated that InN-NCs had hexagonal crystal structure. Moreover, there were In_2O_3 diffraction peaks at two theta degrees of 30.38, 32.72, 35.22, 38.93, 54.23 as shown in the figure. Since we used ethanol as the solvent, In_2O_3 was generated in the solution as a byproduct, together with In metal which had a quite small peak at two theta degrees of 36.10. In_2O_3 peaks became more intense in the sample ablated for 60 minutes indicating that increased ablation times resulted in more oxidation of the nanoparticles. The same hexagonal InN peaks also appeared in the XRD

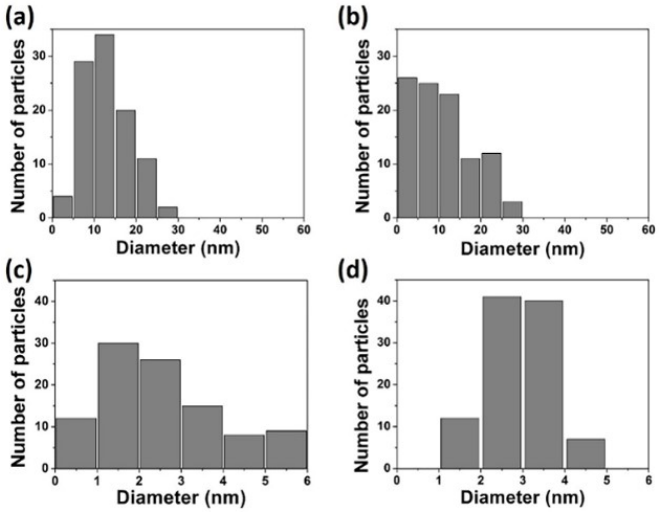

Figure 2.10: Histogram of InN-NCs produced at (a) 15 min and (b) 60 min. After centrifugation of (c) 15 min and (d) 60 min ablated InN-NCs, the ones smaller than 5 nm could be determined.

analysis of the target powder confirming that the process included pulsed laser fragmentation, thus the crystalline phase of the nanoparticles did not change during the production process. Moreover, the molten nanoparticles observed in SEM images do not seem to be modified in terms of crystal structure, which shows that melting did not have any effect on the crystallinity of InN-NCs. The XRD peaks are in a good agreement with the XRD data presented in the literature for the InN-NCs produced or grown with different techniques [22, 26, 27]. Furthermore, In metal and In_2O_3 peaks, except for the one at the 2 theta degree of 30.38, were also present in the XRD analysis of InN powder suggesting that a purer starting material consisting of only InN would result in a colloidal InN-NC solution with less In_2O_3.

2.2.2.5 RAMAN Investigation

Another characterization method for InN-NCs is the Raman spectroscopy analysis. 15 minutes and 60 minutes ablated samples were analyzed and it was found that the sharp peaks at 481.68 cm^{-1} and 479.85 cm^{-1}, respectively, correspond to E_2 mode of the hexagonal InN-NCs (Figure 2.12). The InN-NC RAMAN peaks

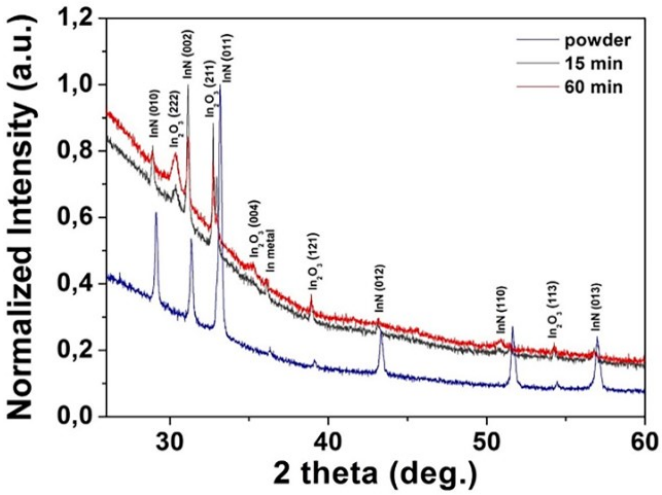

Figure 2.11: XRD analysis of InN powder as the starting material and InN-NCs after 15 min and 60 min laser ablation process. InN powder was shown to be consisting of hexagonal InN together with In metal and In_2O_3. After 15 min and 60 min laser ablation, the hexagonal phase of the nanoparticles did not differ from the phase of the InN powder, which indicated the formation mechanism was through fragmentation. Moreover, the intensity of In_2O_3 peaks increase in 60 min ablated samples when compared to the 15 min samples, implying that longer ablation durations lead to more oxidation of the sample.

and XRD data confirmed the hexagonal phase of the InN-NCs, which is also consistent with the literature [22, 28]. The peak at 516.46 cm^{-1} show the RAMAN spectrum of Si substrate.

2.2.3 Conclusion

We showed for the first time that ultra-small InN-NCs (<5nm in diameter) can be produced from InN powder target by using PLAL technique. We demonstrated that lower laser energy and shorter ablation duration result in much smaller nanoparticles since even if the ablation time increased and the smaller nanoparticles were produced, they tended to aggregate. Hexagonal InN-NCs smaller than 5 nm in diameter were produced in ethanol with optimized ablation conditions successfully. We showed that PLAL is a suitable technique for production of InN-NCs, which is a Group III nitride. Thus, other nitrides in the same group

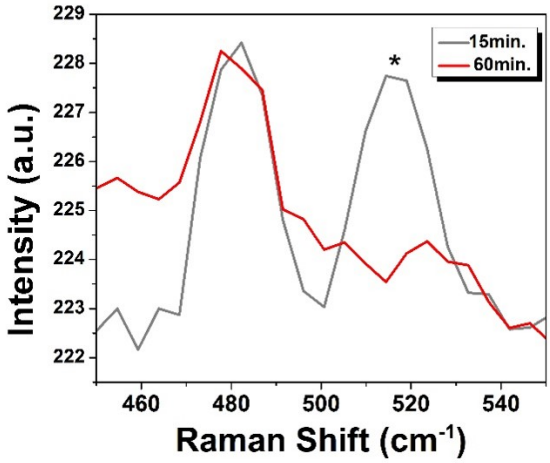

Figure 2.12: RAMAN spectra of InN-NCs produced at 15 min and 60 min. Sharp peaks at 481.68 cm^{-1} and 479.85 cm^{-1} correspond to E_2 mode of the hexagonal InN-NCs. The peak at 516.46 cm^{-1} shows the RAMAN spectrum of Si substrate, which has a $< 111 >$ orientation.

might be successfully produced with this technique. As an outlook of InN-NC production with PLAL method, ablation with femtosecond laser pulses might be studied to overcome the low decomposition temperature disadvantage of InN material.

2.3 Nanoparticle Production with Pulsed Laser Ablation in Atmospheric Environment

2.3.1 Introduction

Although a number of nanoparticles were generated by pulsed laser ablation method in the liquids, it was demonstrated that nanoparticles can also be produced in air or in vacuum (Figure 2.13) by focusing of laser beams onto materials. In a study, it was shown that the ratio of laser ablation in air was 100 times greater than that of in liquid environment, so that the amount of nanoparticles produced in gaseous environment was a lot higher than the liquid environment [49]. This

phenomenon reveals the health risk of these nanoparticles for the people working in laser material processing areas. To our knowledge, no study in the literature has shown the effects of nanoparticles generated in the air as the byproduct of laser material processing. Thus, the main aim of this thesis study was to demonstrate the production of nanoparticles in the atmospheric environment during laser material processing by mimicking the working environment in the industry and to evaluate their health risks on rats upon exposure to these nanoparticles. For this purpose, a material marking laser was purchased and a chamber around this laser was designed and developed to mimic the working environment.

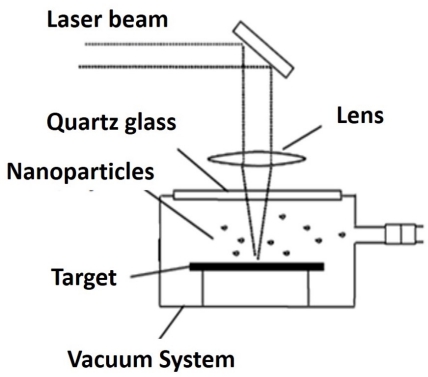

Figure 2.13: Nanoparticle production setup with pulsed laser ablation method in the atmospheric environment. Adapted from [49].

2.3.2 Materials and Method

2.3.2.1 Integration of the Laser System

A nanosecond laser marking system was purchased for the processing of metal plates. For the inhalation experiments, which will be explained in next chapter, an acrylic cabinet around the laser system was also designed and developed so that the rats are effectively exposed to the environment where nanoparticles are produced during the laser material processing. The stability, impermeability and transparency properties were considered while designing the cabinet. Moreover,

two different doors were designed for placing and taking out the materials to be processed and the rats' cage, respectively (Figure 2.14).

Figure 2.14: The laser cabinet which is integrated to the laser marking system and which provides the environment for the nanoparticle exposure of rats during the laser material processing.

The working parameters of the laser system are given in Table 2.1.

2.3.2.2 Optimization of the Nanoparticle Production During Material Processing

In this study, copper, tin and aluminum plates were determined to be used for materials processing. In preliminary studies, the laser parameters were optimized as 1.5 kHz repetition rate, 3W power, 25 mm/sec laser scan speed and 17.25 cm focal length.

10 ml distilled water was placed into the cabinet to collect and characterize the nanoparticles, which are predicted to be produced in the environment during material processing. Scanning electron microscope (SEM) (FEI Quanta 200 FEG) and energy dispersive X-ray spectroscopy (EDX) were used to characterize these nanoparticles. For SEM analysis, nanoparticle sample was drop-casted onto the Si $< 111 >$ wafer.

Table 2.1: Working parameters of marking laser system.

Laser Type	Nd:YAG Diode Laser
Wavelength	1064 nm
Repetition Rate	0-50 kHz
Laser Power	50W
Pulse Duration	100 ns
Pulse Generation Technique	Acoustooptic Q Switch
Focus Diameter	0.3 mm
Cooling System	Water Cooling

2.3.2.3 The Distribution of Copper Nanoparticles in the Cabinet and Their Characterization

After determining and analyzing the marking parameters, the distribution of nanoparticles in the cabinet was evaluated. Moreover, these nanoparticles were characterized. For this purpose, four beakers with 10 ml distilled water inside were placed into four different locations in the cabinet. Beaker 1 was placed just near the marking area, beaker 2 was placed to the area where the rat cage is planned to be placed. Beaker 3 and beaker 4 were placed into the backside and front side corners of the cabinet, respectively (Figure 2.15).

Moreover, the Cu element concentration in the distilled water collected in beaker 2 was determined with Inductively Coupled Plasma Mass Spectrometry (ICP-MS). For this purpose, 1 ml water sample was dissolved in 7 ml of HNO_3.

2.3.2.4 Marking of the Copper, Tin and Aluminum Plate with Laser System and Characterization of the Plates and Nanoparticles

The marking parameters for the copper plate (18 cm in diameter) were determined as 10A current, 1.5 kHz repetition rate, 4W power, 25 mm/sec laser scan speed and 18.5 cm focal length. Moreover, to determine the marking depth of the

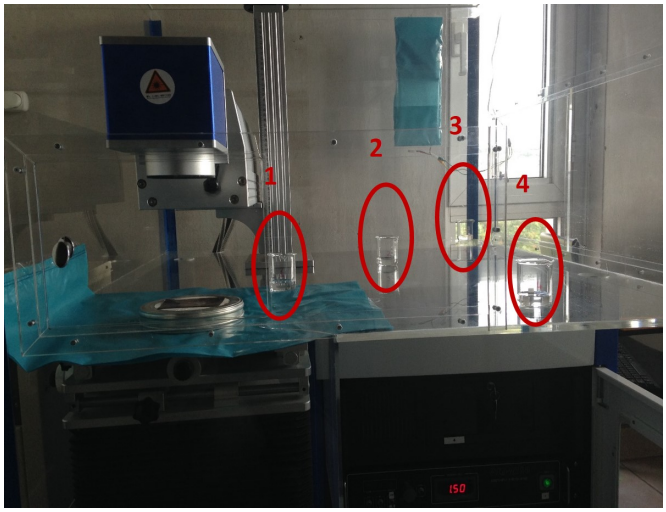

Figure 2.15: Four beakers containing 10 ml distilled water was placed into the laser cabinet to determine the nanoparticle distribution. The laser worked in the pre-determined parameters to mark the copper plate and the nanoparticles collected into the water samples were analyzed.

laser and to make this depth measurable with atomic force microscopy (AFM), a part of the copper plate was marked for 10 times, it was analyzed with SEM and the depth was measured with AFM in a 15 μm x 15 μm area.
The copper nanoparticles (CuNP) which were generated during the marking of copper plate were collected into 10 ml distilled water in a beaker and characterized with X-ray photoelectron spectroscopy (XPS) and transmission electron microscopy (TEM).

The marking parameters for the tin plate (14 cm in diameter) were determined as 10A current, 1.5 kHz repetition rate, 4W power, 25 mm/sec laser scan speed and 18.5 cm focal length. Moreover, to determine the marking depth of the laser and to make this depth measurable with SEM, a part of the tin plate was marked for 5 times, it was analyzed with SEM in 45°. The tin nanoparticles (SnNP), which were generated during the marking of tin plate, were collected in 10 ml distilled water in a beaker, placed into the cabinet. SnNP were characterized with XPS and TEM.

The marking parameters for the aluminum plate (16x14 cm) were determined as 10A current, 1.5 kHz repetition rate, 4W power, 25 mm/sec laser scan speed

and 18.5 cm focal length. To determine the marking depth of the laser and to make this depth measurable with SEM, a part of the aluminum plate was marked for 20 times, it was analyzed with SEM in 45°. The aluminum nanoparticles (AlNP), which were generated during the marking of aluminum plate, were collected in 10 ml distilled water in a beaker, placed into the cabinet. AlNP were characterized with XPS and TEM.

2.3.3 Results and Discussion

2.3.3.1 The Distribution of Copper Nanoparticles in the Cabinet and Their Characterization

Four beakers with 10 ml distilled water inside were placed inside the cabinet to determine the distribution of CuNP in the cabinet. CuNP were shown in beakers 1 and 2, but, no CuNP were demonstrated in beakers 3 and 4. The TEM image of the CuNP collected from beaker 2 was shown in figure 2.16 and it was shown that CuNP has crystalline structure.

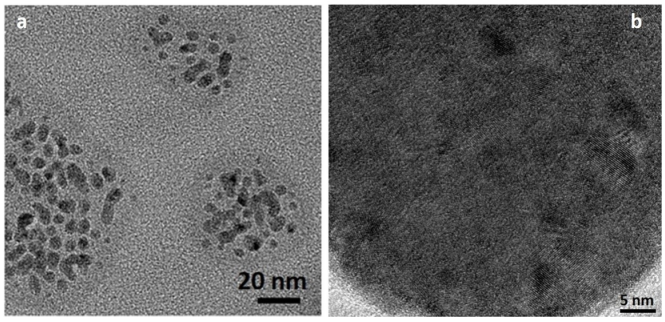

Figure 2.16: TEM analysis of CuNP in beaker 2. (a) TEM image and (b) the crystal structure of CuNP.

Besides the CuNP detected in the sample taken from beaker 2, there were also micron-sized particles, which were demonstrated with the SEM image in figure 2.17a. On the other hand, figure 2.17b reveals that these particles, either nano- or micron-sized, are copper as a result of EDX analysis.

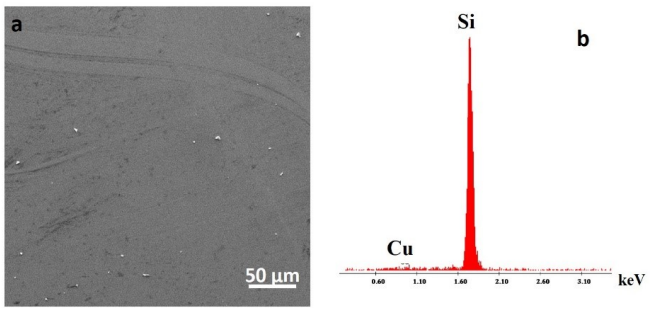

Figure 2.17: (a) SEM and (b) EDX analyses of the sample taken from beaker 2. Si element is found in EDX analysis since the substrate in the characterization is Si wafer.

The distribution profile of nanoparticles generated during laser material processing was determined such that they are mainly distributed near the marking area and the central area, where the rat cage is planned to be placed for the inhalation experiments.

At the end of two hours marking of copper plate, the concentration of Cu element in the distilled water was determined as 0.241 μg/g. Moreover, the same sample was characterized with XPS and the analysis data confirmed that the CuNP is present in the water sample (Figure 2.18).

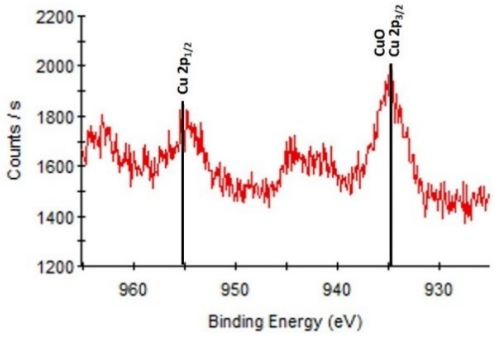

Figure 2.18: XPS analysis of CuNP in beaker 2. The presence of Cu $2p_{1/2}$ and Cu $2p_{3/2}$ are shown with the consistence of the literature (ref).

2.3.3.2 Marking of the Copper, Tin and Aluminum Plate with Laser System and Characterization of the Plates and Nanoparticles

SEM and AFM analyses of copper plate after 10 times marking are shown in figures 2.19 and 2.20, respectively. It was determined that the depth of the one marking step was 160 nm.

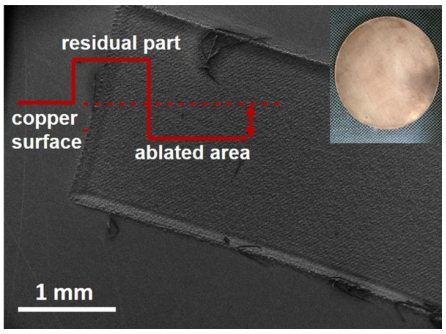

Figure 2.19: The laser marked part of the copper plate. The copper plate is shown as an inset in the figure.

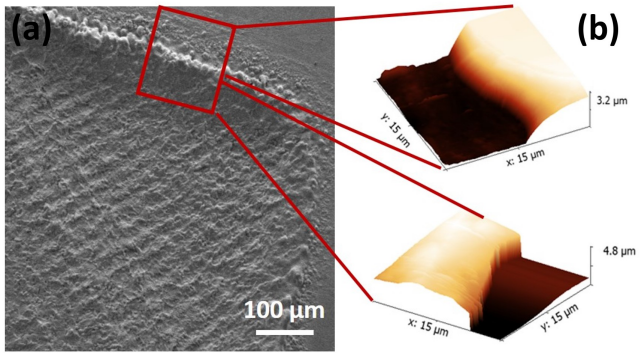

Figure 2.20: (a)Ten times laser marked part of the copper plate and (b) the AFM analysis of a 15 μm x 15 μm area. It was determined that the depth of the one marking step was 160 nm.

The pure tin plate with a 14 cm diameter and the marked area on the plate are shown in Figure 2.21. To be able to determine the marking depth, SEM analysis was performed and it was found that one time laser marking results in a 71.9 μm depth (Figure 2.22).

To collect the SnNP samples for further characterization, SEM, XPS and TEM analyses were performed by using the 10 ml distilled water placed into the cabinet.

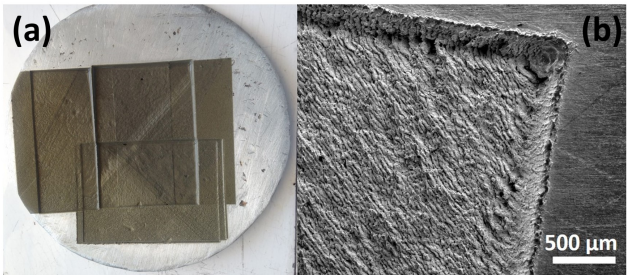

Figure 2.21: (a) Tin plate used in the marking process and (b) the SEM image of the marked area.

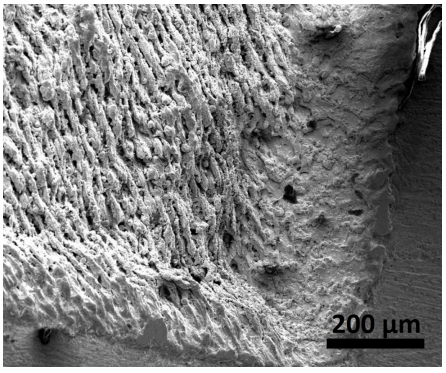

Figure 2.22: To be able to determine the marking depth, the tin plate was marked for five times and the measurement was performed with an angle of 45° with SEM. The depth was calculated from this image and determined as 71.9 μm.

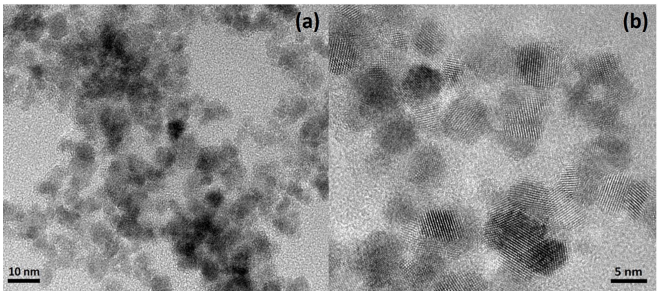

Figure 2.23: (a) TEM image and (b) cyrstaline structure of SnNP generated during the tin plate marking.

TEM images demonstrated that the SnNP had a crystalline structure (Figure 2.23). SEM analysis confirmed that the SnNP were spherical in shape (Figure 2.24). In SEM images, it was revealed that micron-sized particles are also present in the environment, together with the nanoparticles. Moreover, the particles were confirmed as tin with the XPS analysis and shown in figure 2.25.

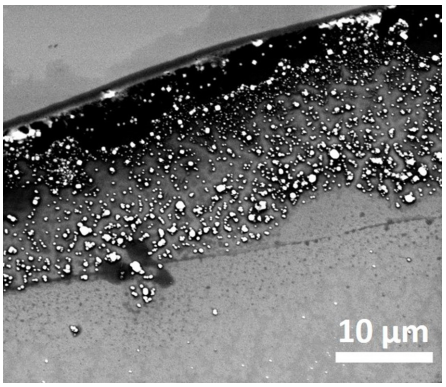

Figure 2.24: The SEM analysis of SnNP generated during the tin plate marking.

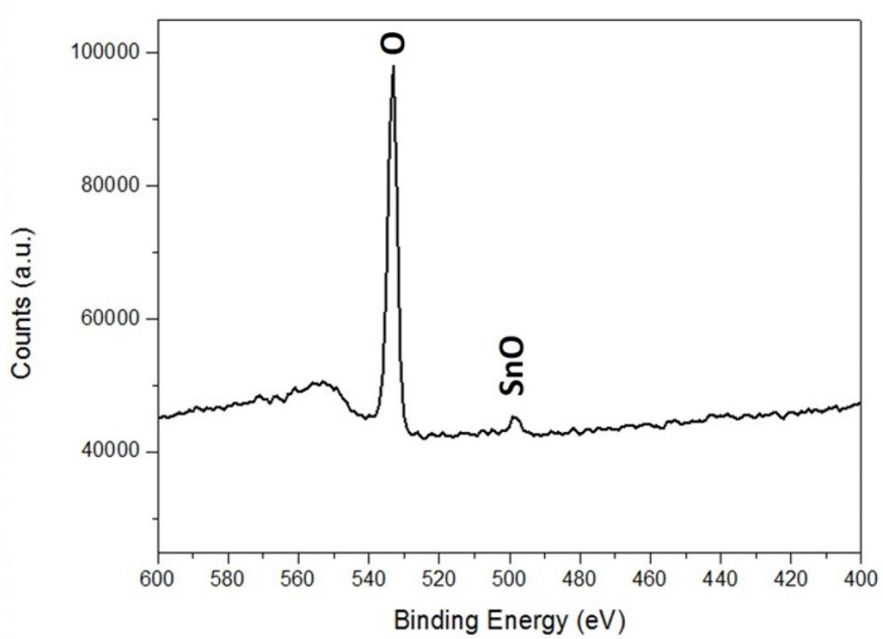

Figure 2.25: The XPS analysis of SnNP generated during the tin plate marking. SnO and O peaks were confirmed with the literature.

The pure aluminum plate (16x14 cm) and the SEM image of the marked area on the aluminum plate are shown in figure 2.26. To determine the marking depth,

the SEM image with an angle of 45° was employed and the depth was measured as 5.13 μm in a single marking step (Figure 2.27).

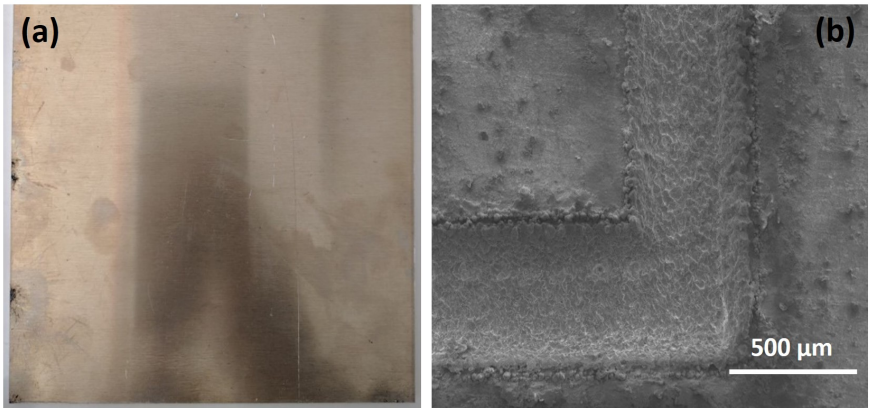

Figure 2.26: (a) Aluminum plate used in the laser marking process and (b) the SEM analysis of the marked area.

For the characterization of AlNP generated during the aluminum plate marking process, AlNP were collected in 10 ml distilled water in the beaker located in the same location as the beaker 2 in previous analyses. TEM analysis showed that AlNPs had crystalline structure (Figure 2.28). It was confirmed that the nanoparticles are AlNP and its oxide form since the analysis was performed in distilled water (Figure 2.29).

2.3.4 Conclusion

It was shown that CuNP, SnNP and AlNP were successfully produced in the environment during the marking of respective metal plates. With the TEM analyses, it was demonstrated that all nanoparticles were crystalline in the structure. Moreover, a wide range of size distribution was obtained for all the nanoparticles produced in laser material processing setup. There were nanoparticles smaller than 10 nm but the particles larger than a few microns were also detectable in SEM images. This data indicate that laser material processing in the industry constitutes high risk for the workers since they expose to the nanoparticles without any protective material and we achieved a successful mimicking environment for the exposure studies, which will be described in the next chapters.

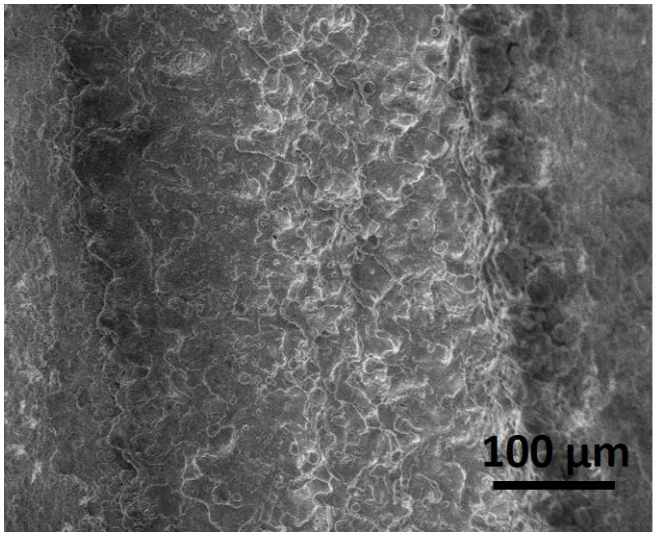

Figure 2.27: To be able to determine the marking depth, the aluminum plate was marked for twenty times and the measurement was performed with an angle of 45° with SEM. The depth was calculated from this image and determined as 5.13 μm.

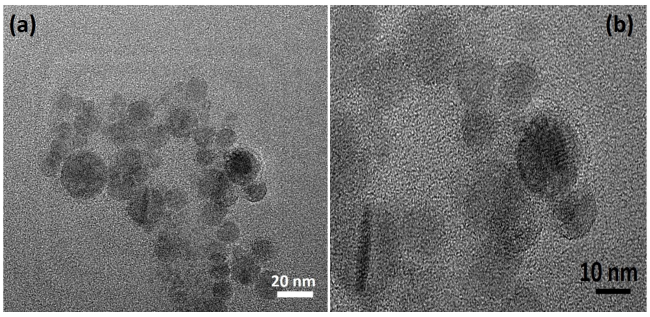

Figure 2.28: (a)TEM analysis and (b) their crystalline structure of AlNP generated during the laser marking of tin plate.

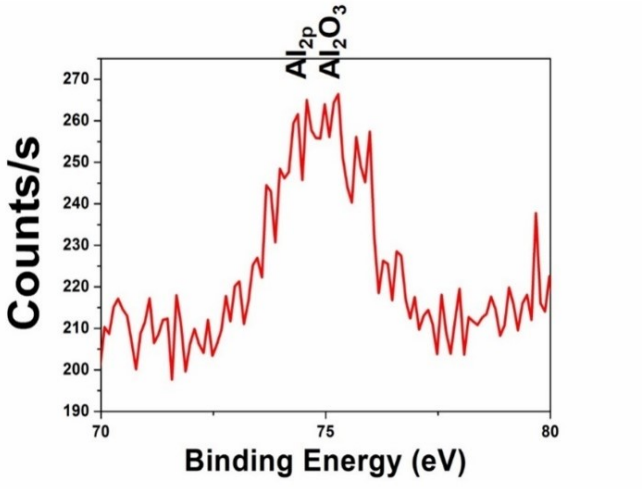

Figure 2.29: XPS analysis of AlNP generated during the laser marking of tin plate. Al and Al_2O_3 peaks were confirmed with the literature.

2.4 Conclusion

In this chapter, the production of nanoparticles in liquids and in atmospheric environment was introduced. Firstly, the mechanism of pulsed laser ablation was defined. A number of nanoparticles were generated throughout this thesis study and among them, a systematic study, the production of ultra-small InN-NCs, was presented in detail in this chapter. We showed for the first time that hexagonal, ultra-small InN-NCs (<5 nm in diameter) can be produced from InN powder target by using PLAL technique. We also suggested that the laser parameters are important factors affecting the size distribution of the nanoparticles.

Besides the nanoparticle production by pulsed laser ablation in liquid, the production of nanoparticles by pulsed laser ablation in the atmospheric environment was also described in this chapter. It was demonstrated that both nano- and micron-sized particles are generated in the environment during the laser material processing. These nanoparticles were characterized and it was shown that laser material processing environments have the potential of the health risks for people working in these fields.

Chapter 3

Nanoparticle Exposure to Rats in Laser Material Processing Environment Mimicking the Real Industrial Exposure

3.1 Introduction

In the previous chapter, it was investigated that CuNP, SnNP and AlNP were produced in the environment during laser material processing in the setup designed and developed to mimic the industrial applications. In this chapter, the effects of these nanoparticles on the learning and memory behavior and the moods of the rats will be investigated. Firstly, the learning and memory concept will be introduced in detail and the nanotoxicity concept will be explained. Then, the experimental setup for the exposure of rats to the laser material processing environment, the behavioral and electrophysiological experiments and molecular analyses will be mentioned along with the results and discussion.

3.1.1 Learning and Memory

3.1.1.1 Hippocampus

Learning can be defined as the process which functions upon getting new information. Memory, on the other hand, is retaining this acquired information. Memory can be categorized as explicit and implicit memory, where someone recalls the information consciously (e.g. information about the places or people) or unconsciously (e.g. motor skills), respectively. Brain parts responsible for the explicit memory are temporal lobe, hippocampus, subiculum, and entorhinal cortex while cerebellum and basal ganglia are responsible for the implicit memory [50].

Table 3.1: Brain areas responsible for different types of learning/memory. Adapted from [1].

Type of Learning/Memory	**Brain Areas Involved**
Spatial Learning	Hippocampus
	Parahippocampus
	Subiculum
	Cortex
Emotional Memory	Amygdala
Recognition Memory	Hippocampus
	Temporal Lobe
Working Memory	Hippocampus
	Prefrontal Cortex
Motor Skills	Striatum
	Cerebellum
Sensory (visual, auditory,tactile)	Various cortical areas
Classical conditioning	Cerebellum
Habituation	Basal Ganglia

A number of brain parts were shown to be significant for the integrity of several learning and memory forms as shown in Table 3.1. However, hippocampus was shown to be playing a significant role in the declarative memory formation. It was demonstrated for the first time in 1957 that when the hippocampus is removed bilaterally, the patient suffered from anterograde amnesia, indicating

the importance of hippocampus in the memory process [51]. A number of neuropsychological studies conducted with the amnesic patients, together with the functional imaging analyses on the normal human subjects further revealed that hippocampus is the main brain part for the learning and memory formation process [52, 53, 54].

The major neuron type found in the hippocampus is pyramidal cells, which have a basal dendritic tree and an apical tree extensions. The hippocampus can be divided into three main regions according to the different characteristics of these pyramidal cells as CA3, CA2 and CA1 regions [55]. CA3 and CA2 pyramidal cells display variability depending on their dendritic length, organization and the location of the cell body [56]. On the other hand, CA1 pyramidal cells are much more homogenous in terms of their dendrites and they are much smaller than CA3 cells [57].

The term "trisynaptic circuit" in the hippocampus was introduced by Andersen et al. [58]. In this circuit, the excitatory synaptic pathway in the hippocampus consists of entorhinal cortex (EC), dentate gyrus, CA3 neurons, CA1 neurons and EC. Through the perforant pathway, which includes the lateral perforant pathway (LPP) and medial perforant pathway (MPP), the axons of layer II neurons located in EC reaches to the dentate gyrus. The projections from the dentate gyrus extend to the pyramidal cells in CA3 region through the mossy fibers. Schaffer collaterals lead to the transfer of the information from CA3 pyramidal cells to the CA1 pyramidal neurons, which send the projections back to the EC neurons located in the deep-layers (Figure 3.1).

The excitatory neurons form a three-layer circuit in the hippocampus. The input from EC enters the hippocampus via granular cells in dentate gyrus, connecting through the mossy fiber synapses to CA3 pyramidal cells. After the processing to input in CA3 pyramidal cells, the output is sent to Schaffer collaterals and then to the CA1 pyramidal cells through the synaptic connections. CA1 pyramidal cells send the output information to the cortex via subiculum. Throughout this circuit, the fast excitatory synaptic transmission is mediated

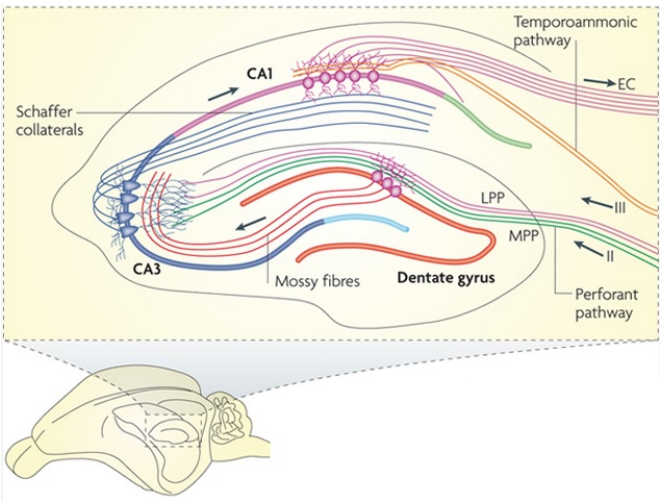

Figure 3.1: The detailed structure and the neural network of hippocampus. Adapted from [59]. EC: entorhinal cortex.

by excitatory postsynaptic potentials (EPSPs) flowing through the ionotropic α-amino-3-hydroxy-5-methyl-4-isoxazolepropionate (AMPA) and kainate types of glutamate receptors to a lesser extent. On the other hand, the slow EPSPs are mediated by the N-methyl-D-aspartate (NMDA) receptors and certain subtypes of metabotropic glutamate receptors. Besides the excitatory system, hippocampus is also controlled by an inhibitory system, which is mainly mediated by γ-aminobutyric acid (GABA)ergic interneurons located in the hippocampus. Two types of GABA receptors, ionotropic $GABA_A$ and metabotropic $GABA_B$, are responsible for the inhibitory postsynaptic potentials (IPSPs), respectively. Moreover, some of the metabotropic glutamate receptors are responsible for the IPSPs rather than EPSPs. Besides, muscarinic and nicotinic receptors also have roles in the excitatory or inhibitory roles upon binding of different neurotransmitters, such as acetylcholine, noradrenaline, dopamine, serotonin and histamine, depending on the receptor type [60].

3.1.1.2 NMDA Receptors

NMDA receptors (NMDARs) are glutamate-gated cation channels and they have a permeability for Ca^{2+}. They have a number of important roles in the central

nervous system (CNS) such as locomotion, learning, memory, and neuroplasticity. Thus, alterations in the expression and/or function of NMDAR are found to be related to a number of neurological disorders and pathological conditions. The decrease in NMDAR functioning might lead to cognitive defects while overstimulation results in excitotoxicity and neurodegeneration. Thus, NMDARs can be considered as the significant targets for many CNS disorders such as Huntington's, Parkinson's, and Alzheimer's diseases, epilepsy, schizophrenia, and mood disorders [61, 62, 63, 64].

Functional NMDARs in mammals consist of heterotetramers of three different subunits encoded by three different gene families. These subunits are NMDAR1, NMDAR2, and NMDAR3 [65, 66, 67]. NMDAR1 subunit is expressed from one gene while NMDAR2a subunit is expressed from four genes (from A to D) [65]. Also, NMDAR3 gene family includes two genes (A and B) [66]. NMDAR1 is the essential subunit which are found in all tetramers but NMDAR2 is included into the structure depending on the age and the location of the neuron. On the other hand, NMDAR3 subunit has role as negative components in the receptor structures, which means that NMDAR3, by binding to NMDAR1 and NMDAR2, reduces the whole-cell current and single-channel conductance [68]. There are eight different variants of NMDAR1, which is transcribed with alternative splicing and distributed throughout the different regions of the nervous system [69, 70]. So, there is a huge functional diversity among NMDARs due to the different splice variants and the composition of the subunits [**?**]. The studies about the expression profiles of NMDARs demonstrated that the expression depends on the cell or the tissue. Moreover, the expression was shown to be regulated by different physiological, pharmacological, and pathological factors. As the initial and the most sensitive step, transcription of the NMDAR is the major mechanism on the gene expression control [71]. The transcription of each NMDAR subunit is controlled in coordination to the cell or tissue but it is also affected by the cell type, developmental stage and environmental stimuli [72, 73]. The 5' end structures of NMDAR1, NMDAR2a and NMDAR2b with the key elements in their expression are represented in figure 3.2. A number of cis-acting regulatory elements with the interaction of transcription factors were shown to be responsible

for the NMDAR gene expression in different conditions [**?**].

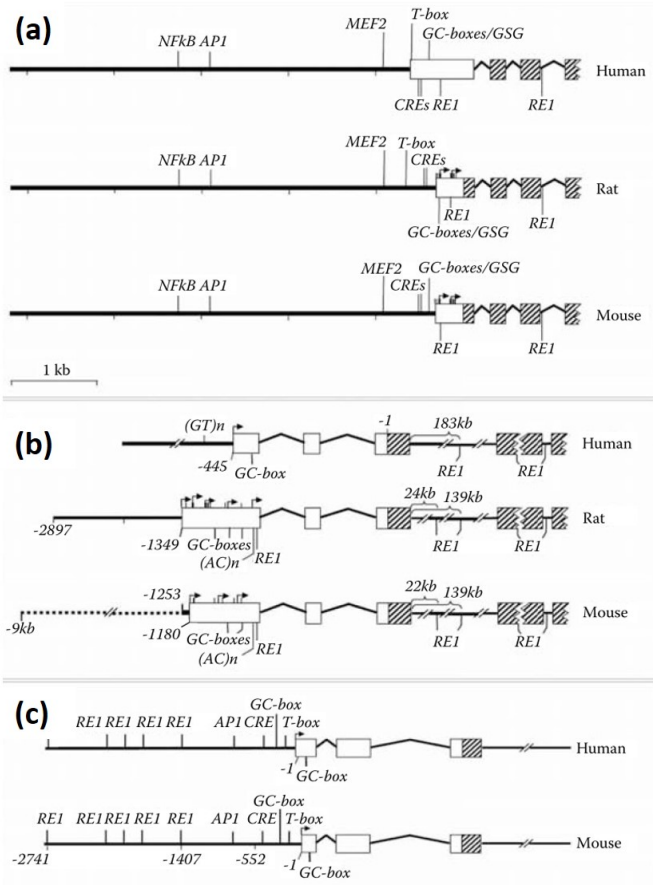

Figure 3.2: The 5 end structures of NMDAR1, NMDAR2a and NMDAR2b genes. (a) NMDAR1, (b) NMDAR2a, (c) NMDAR2b. Adapted from [74].

Upon activation of NMDAR, a number of downstream pathways are activated within the cell. Upon NMDAR activation, Ca^{2+} influx into the neuron is observed. Besides, other secondary messenger molecules such as cAMP, diacylglyercol (DAG), and inositol-3,4,5-trisphosphate (IP3), are promoted in the cell as a result of NMDAR activation and its association to G-protein signaling to adenylate cyclase (AC) and calcium activated phospholipase (PLC). The promoted secondary messengers trigger the activation of different types of kinases such as cAMP-dependent kinase (PKA) and protein kinase C (PKC). Calcium release from the internal stores is achieved by the increased intracellular Ca^{2+} and IP3 (Figure 3.3a). Moreover, NMDAR can activate the translational elongation processes. The extracellular Ca^{2+}, which entered into the cell

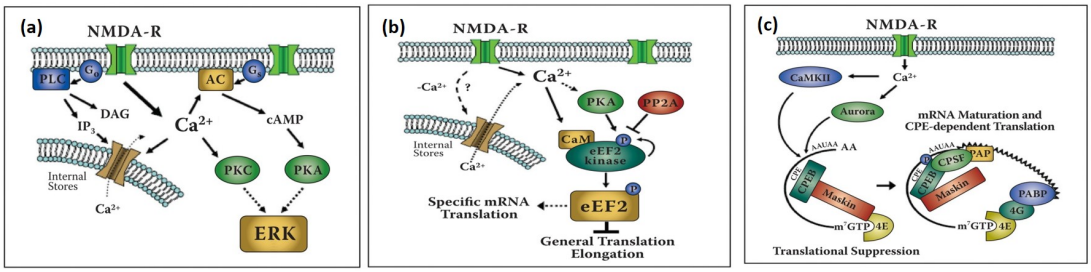

Figure 3.3: NMDAR Downstream Pathways. (a) Increase in the intracellular Ca^{2+}, (b) Activation of translational elongation process, (c) regulation of mRNA maturation Adapted from [**?**].

upon NMDAR activation, triggers the cAMP-dependent protein kinase (PKA). eEF2 kinase (CaMKIII) is activated by PKA-dependent phosphorylation Ca^{2+}-calmodulin complex. After the autophosphorylation of eEF2 kinase (p-eEF2), the translational elongation is suppressed. This leads to a general protein synthesis suppression in the neuron but it might also lead to the enhancement in the translation of some mRNAs which has a low translation profile under normal conditions. eEF2 kinase can be dephosphorylated by protein phosphatase 2A (PP2A) and the translation elongation continues. Thus, NMDAR activation leads to the promotion of eEF2 kinase suppression pathway as a result of Ca^{2+} influx (Figure 3.3b). NMDAR activation also results in the regulation of mRNA maturation with cytoplasmic polyadenylation element-binding protein (CPEB), which shows the transcriptional control of NMDAR on the gene expression profile of the neuron (Figure 3.3c) [**?**].

3.1.1.3 Long Term Potentiation

Long term potentiation (LTP) can be described as the constant increase in the size of the synaptic component of the evoked response, which can be recorded from an individual neuron or a neuron population. It is generally induced with repeated high frequency stimuli [75]. LTP has three major characteristics, namely, cooperativity, associativity and input-specificity. For the induction, there is a need for the stimulation having the necessary intensity higher than the threshold. Any stimulus lower than the threshold would activate a few neurons, which will

not induce LTP. Thus, LTP show cooperativity property [76]. Moreover, LTP shows associativity since a weak input can also induce LTP if it is accompanied by another strong and convergent stimulus [77, 78]. Furthermore, since the stimuli which are not active during the specific repeated stimuli are not included in the same pathway, indicating the input-specificity of LTP [76, 79]. These three characteristics can be explained on the basis of the assumption that a synapse is potentiated if, and only if, it is active at a time when the dendrite on which it terminates sufficiently depolarized.

The most important receptor type having a role in LTP induction is NMDA receptor. When the neuron cell membrane is sufficiently depolarized to discharge the Mg^{2+} NMDA channels after the L-glutamate binding to NMDA receptor to open these channels, LTP induction is observed [80]. Moreover, the permeability of NMDA channels to Ca^{2+} provides the necessary Ca^{2+} signal for the LTP induction [81]. The LTP induction pathway is shown in detail in Figure 3.4. Low-frequency stimulation of Schaffer collaterals results in the formation of EPSP, mediated by L-glutamate acting on AMPA receptors. After the formation of EPSP, an IPSP is formed due to the glutamatergic excitation of GABAergic interneurons. The Cl^- permeable ionotropic $GABA_A$ receptors are activated and the early phase of IPSP is observed. On the other hand, $GABA_B$ receptors, which are indirectly coupled to K^+ channels, are also activated as a part of the slow IPSP component. Thus, NMDA receptor cannot contribute to the EPSP at low frequency stimulation that much due to blocking of the channels with Mg^{2+} ions (Figure 3.4a). On the other hand, when a high-frequency stimulation is triggered, Mg^{2+} is relieved from the NMDA receptor channel due to strong depolarization and this removal lead to Ca^{2+} influx into the cell [60].

The signal transduction pathway for the early phases of LTP is shown in Figure 3.5. After the Ca^{2+} influx into the cell through NMDA receptor, the Ca^{2+} concentration increases by the release from Ca^{2+}/IP3- sensitive stores. Increased Ca^{2+} concentration, together with the other protein kinase activators, result in the phosphorylation of substrate proteins, such as NMDA and AMPA receptors. The phosphorylated AMPA receptors, which are not inserted into the cell membrane, are also inserted into the postsynaptic membrane after LTP induction, leading to

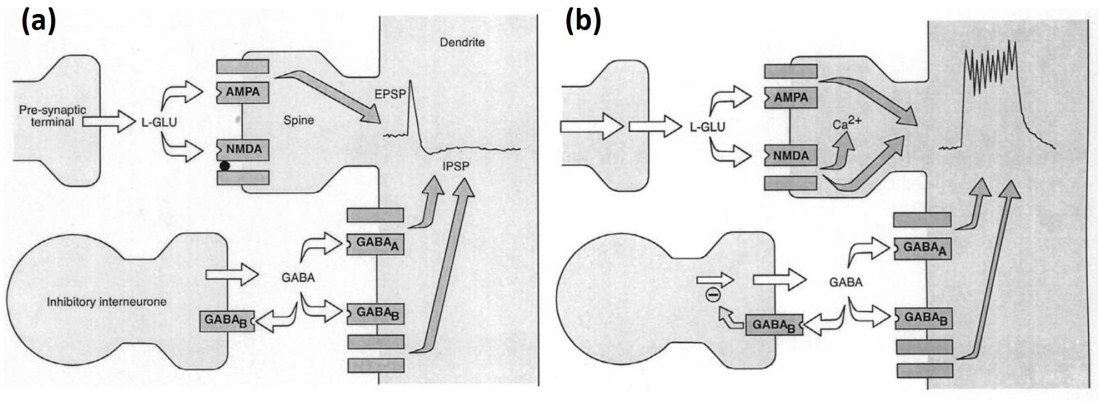

Figure 3.4: The induction of LTP is triggerred by the activation of NMDA receptors, which is controlled by other ionotropic amino acid receptors. (a) Low frequency stimulation and (b) high frequency stimulation in LTP process. Adapted from [75].

an increase in AMPA receptor number and synaptic efficiency. While the post-translational processes are observed in early phase of LTP, the protein synthesis-dependent mechanism are seen in the late phases of LTP [60].

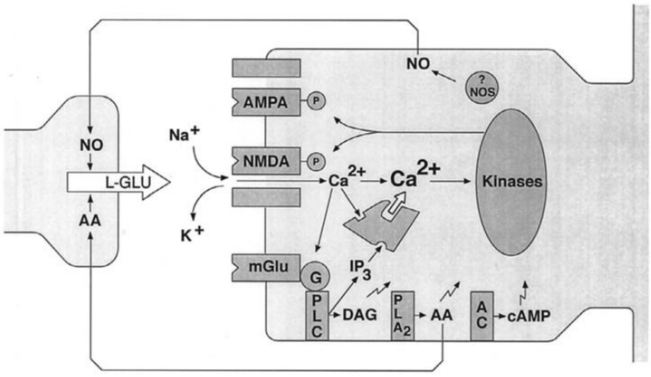

Figure 3.5: NMDA Receptor Pathway in Early Phases of LTP. NO: nitric oxide, AA: arachidonic acid. Adapted from [75].

The "trisynaptic circuit" defined in the hippocampus and LTP processes mediates the cognitive processes of declarative memory. A number of experimental protocols are performed for determination of LTP and the spatial memory process. One of the spatial memory test approaches is Morris water maze, in which the rodent should find out the hidden platform submerged below the surface of the water in a tank after releasing from different points of the pool. After a

number of trials, the animal learns the location of the hidden platform and remembers it by the help of spatial contextual cues. An intact hippocampus is responsible for this task. It was shown that when NMDAR is blocked by antagonist injections, the animal can find the place of the hidden platform but it cannot remember its place in the other trial [82]. Moreover, the passive avoidance test, in which the animal is trained so that it avoids the entrance to a shock-associated compartment, is used for the determination of the avoidance learning, which is related to the hippocampal learning procedure [83]. Besides the behavioral tests, electrophysiology measurements can be performed from the hippocampus. Since the pyramidal neurons and their dendrites are orderly arranged in CA3 and CA1 regions of hippocampus, electrical field recordings give significant information about the temporal arrangement of neuronal responses. When Schaffer collaterals are stimulated via a stimulating electrode, the action potentials from the presynaptic fibers are recorded as the small negative potentials with the extracellular recording electrode located in stratum radiatum. A slow negative potential, which corresponds to population EPSP, is also recorded and it demonstrates the postsynaptic membrane depolarization. This implies that the stimulation reached to CA1 neurons from CA3 neurons. When the recording electrode is placed to the stratum pyramidale, the current in the dendrites is measured and it displays a positive deflection. One or more action potentials are fired when the depolarization is above the threshold of the pyramidal cells. The recording will include a negative potential overlapping a positive potential and it is called as population spike (PS). PS is affected by three different factors; EPSP amplitude, the passive properties of CA1 pyramidal cell and the inhibition level due to the GABAergic interneurons in CA1 region. The alteration of the PS provides information about the number and excitability of the neurons contributed to the process in the hippocampus [60] (Figure 3.6).

3.1.2 Blood-Brain Barrier

Blood-brain barrier (BBB) is an endothelial barrier found in the capillaries surrounding the brain [84]. The endothelial cells in the brain is different from the

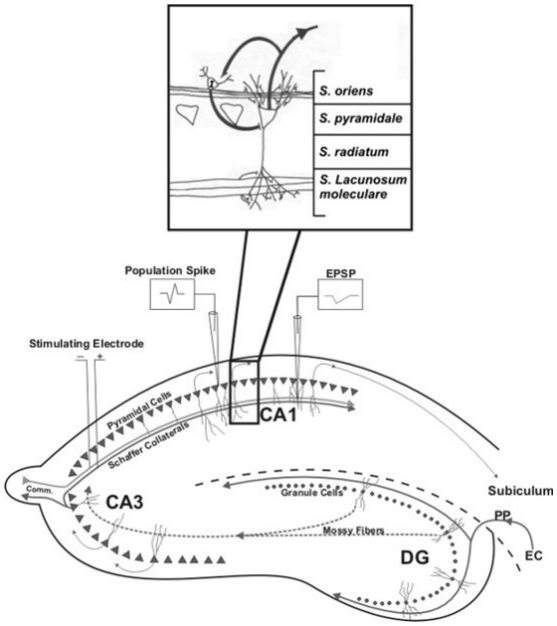

Figure 3.6: EPSP and population spike recordings in the hippocampus. Adapted from [60].

ones in the peripheral tissues such that they have few endocytotic vesicles and they are coupled to tight junctions. These two significant properties lead to the limitation of the transcellular flux and restriction of paracellular flux [85] (Figure 3.7). BBB blocks the entrance of all molecules from blood to brain, except for the small and lipophilic ones. However, some small or large hydrophilic molecules can also pass from BBB through active transport [86]. Moreover, there are certain membrane transport proteins in high concentrations in brain endothelial cells to allow the passage of essential nutrients, such as glucose and certain amino acids. Furthermore, there are certain receptor mediated systems for the passage of macromolecules, such as transferrin receptor [87]. In a number of studies, it was shown that the disruption of BBB results in the accumulation of blood-originated neurotoxic proteins in the CNS such as fibrin, thrombin, hemoglobin, free iron, and/or plasmin. As a result, neuronal toxicity, oxidative stress and/or detachment of the neurons from extracellular matrix lead to the progressive neurodegeneration in the brain [88, 89, 90, 91].

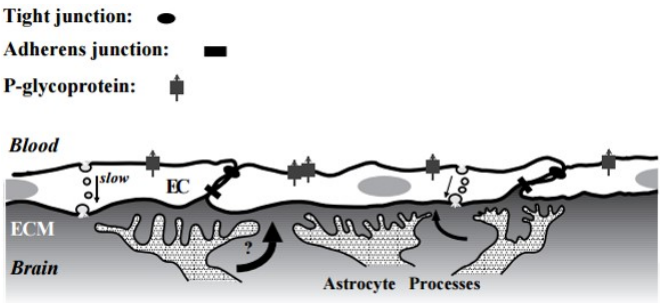

Figure 3.7: Blood Brain Barrier. Adapted from [85].

3.1.3 Nanotoxicity

Nanoparticles are produced as a result of various methods applied in industry, and one of the most important examples of these methods is cutting or drilling of materials using lasers. The use of lasers for this purpose is getting more common every day [92]. Laser ablation of materials are frequently used in automobile, aviation, seafaring and material processing industries [93]. Besides, another application of lasers in industry is drilling, which is the removal of the material where the laser beams are focused [94]. Drilling via laser is defined as a thermal and ionic process in which the high density laser beams are focused on a single point with enough energy to vaporize the material on its way [95]. During both cutting and drilling of materials with lasers, this thermal process operates and material leftovers are removed from the area of process. As the removed particles are nucleated, nanoparticles are produced [7]. As these nanoparticles are able to move freely in the air, workers are exposed to these nanoparticles constantly. Materials used in industry are mostly comprise heavy metals such as nickel and lead, and processing of these materials causes the release of nickel and lead nanoparticles. Respiration of these nanoparticles by the workers poses a great danger on health of the workers. Amount of nanoparticles produced by laser ablation of brass plates for one hour is enough to cover a 1 cm^2 surface area [96]. This demonstrates the supremacy of the amount of nanoparticles exposed and severity of damage that they bring.

Nanoparticles are environmental pollutants when produced in nature and in industry. When these nanoparticles are inhaled, they are distributed throughout

the body after they enter the systemic circulation from the lungs. There are lots of *in vitro* studies examining the toxic effects of nanoparticles on cell lines. It was shown that, nanoparticles cause reactive oxygen species (ROS) in cells, resulting in disruption of metabolic pathways via oxidative stress [97]. Toxic effects of nanoparticles on lung cell lines are especially researched to this day [97]. Apart from lung cell lines, there have been studies on certain cell lines, as well. In one of these studies, manganese (Mn) and Cu nanoparticles were found to increase ROS in cells and disrupt dopamine biosynthesis in neuronal cell lines [98]. In addition, similarly, cadmium selenite (CdSe) and zinc sulphur (ZnS) nanoparticles were shown to decrease catecholamine synthesis in mouse chromaffin cells [99]. Furthermore, in a study to show effects of nanoparticles on heart tissue in vitro, titanium dioxide (TiO_2) and silisium dioxide (SiO_2) nanoparticles caused rhythm abnormalities in hearts perfused with these nanoparticles [100]. Aluminum nanoparticles were also led to the induction of ROS production in human neuron cell line and decreased the cell survival [101].

As a result of a wide variety of *in vivo* studies in which rats or mice were exposed to nanoparticles via various methods, data about in which organs the nanoparticles accumulate and how they are disposed from the body, was obtained. In these studies, animals are exposed to nanoparticles via unnatural methods such as instillation of prepared and commercially available nanoparticles into nostrils or loading onto aerosol droplets [102]. It was shown that silver nanoparticles were detected in brain, liver, kidney and olfactory bulb of the rats which were exposed to the nanoparticles via inhalation [103]. Moreover, similar exposure studies were performed by using titanium nanoparticles and similar results were observed [104, 105]. The silver and gold nanoparticles taken into body were shown to pass the BBB and resulted in various neurotoxic effects in the brain [106]. Moreover, in the rats exposed to silver, gold and aluminum nanoparticles, BBB was shown to be disrupted [8]. The gold nanoparticles dropped into the noses of monkeys were detected in olfactory bulb due to the network of olfactorial neurons [107]. After one day of silver nanoparticle inhalation to the rats, high concentration of silver nanoparticles were observed in the olfactory nerve, indicating that the passage to central nervous system might be through this route

[108]. It was indicated that the nanoparticles that reach to brain activate the microglia and increase the expression levels of proinflammatory cytokines and chemokines, resulting in the inflammation [109]. The mice exposed to TiO_2NPs displayed an increase in the proinflammatory cytokine levels in the hippocampus, which are associated with neuroinflammation [110]. Moreover, since the nanoparticles lead to oxidative stress in the cells due to ROS production, the risk for a number of neurodegenerative conditions emerges such as Parkinson's, Alzheimer's and Huntington's. When the silver nanoparticles are administered to mice intranasally, Hmox1 gene expression, which is associated to the oxidative stress, was shown to increase only in the hippocampus region [111]. These mice also exhibited impairment in their memory. The rats were exposed to the exhaust gas, in which there are a number of nanoparticles, and it was demonstrated that there are neurotoxic effect in these animals. Moreover, alterations in the expression levels of NMDAR subunits and kinases and transcription factors in the downstream pathway of the NMDAR [112]. It was suggested that the neurotoxic and behavioral effects of the nanoparticles might be related to the type and the characteristics of the nanoparticles. Zinc oxide nanoparticles were administered to the rats intraperitoneally for 8 weeks and they exhibited impairment in long term plasticity and cognitive functions [113]. TiO_2 nanoparticles were shown to have negative effects on the spatial learning and memory behavior of the rats, which were administered the nanoparticles for 60 days via intragastric route [114]. Gold nanoparticles were administered intraperitoneally to the rats and after 21 days of administration, a decline in the learning and memory processes was observed. Moreover, the nanoparticles were found to be accumulated in the CA1 region of the hippocampus [105]. In two different studies, silver nanoparticles were administered to rats by dropping to the nose and intraperitoneal injection, respectively, impairements in the learning and memory of the rats were observed [115, 116].

Moreover, there are a few human studies related to the nanotoxicity in the literature. Brains of the people living in Mexico city and exposing to severe air pollution displayed the accumulation of beta amyloid plaques, which indicate the Alzheimer disease pathology [117]. Furthermore, in another clinical study, the

neurophysiological signals were disrupted in the electroencephalography measurements after exposure to exhaust gas for one hour [118].

Copper (Cu) has a number of roles for the normal physiological pathways in the body, such as the formation of hemoglobin, metabolism of drugs and carbohydrates, catecholamine biosynthesis and antioxidant defense mechanism [119, 120]. However, if the concentration of copper in the body surpasses the biological limit, it might result in a number of adverse effects such as hemolysis, gastrointestinal problems, and damage to liver and kidney [121, 122]. Copper nanoparticles (CuNP) and copper oxide nanoparticles are frequently used as lubricants for metallic coating, additives in livestock and poultry feed and polymers/plastics [123]. Moreover, CuNP possess exceptional thermophysical properties, which result in an increasing interest in electronics applications, such as electronic chips, heat transfer nanofluids and semiconductors [123, 124]. Besides, CuNP has an antimicrobial activity against a number of pathogenic microorganism, which makes it a good candidate for antimicrobial agent in biomedical applications [125, 126, 127]. Although CuNP has a great potential in these applications, due to the novel characteristics that nanoparticles gain at the nano-size level, CuNP was shown to exert a number of toxicological effects *in vivo* when compared to the bulk copper [128, 129, 130].

Chen et al. (2006) suggested that CuNP (23.5 nm) is more toxic than copper micron particles (17 μm) in mice since nanoparticles gain access to body via contact, inhalation and digestion more easily compared to micron sized particles [128]. Moreover, in the same study, CuNPs were shown to cause pathological damage in various organs such as liver, kidney, and spleen [128]. Besides these important organs, central nervous system has a high risk of nanoparticle exposure since the nanoparticles can reach the brain both by systemic circulation and through the olfactory bulb via the olfactory mucosa [131, 132]. It was shown that intraperitoneal (i.p.) injection of CuNP to rats resulted in blood brain barrier (BBB) disruption and edema formation in the brain [133].

Tin nanoparticles (SnNP) are highly used as corrosion-resistant covering of

food cans, in metal alloys, photovoltaic materials and next-generation rechargeable Li-ion batteries [134]. Although it has a number of applications in the fields that humans can encounter, there are no toxicological studies for SnNP in the literature.

Aluminum and alumina nanoparticles (AlNP and Al_2O_3) was reported as one of the mostly produced nanoparticles in the world [135]. AlNP is widely used as catalysts [136], in the reinforcement [137], modification of the polymers [138], functionalization of textile products [139], and waste water treatment [140]. Moreover, AlNPs are proposed to be used in a number of biologicak applications such as biosensors [141], drug delivery [142], biofiltration and antigen delivery [143]. Since they have a number of different applications, the toxicological studies on AlNP has a great importance.

It was demonstrated that alumina nanoparticles results in an increase in the adhesion of activated monocytes in human endothelial cell line. The nanoparticles aggregated in the physiological pH and conditions, resulting in the micron sized particles. Thus, alumina nanoparticles were shown to have a high risk for atherosclerosis and cardiovascular disease [144]. Moreover, in another cell line study, AlNP resulted in a toxicity depending on its chemical composition. AlNP were shown as more toxic than Al_2O_3 NP and they significantly affected the phagocytosis ability of rat alveolar macrophages [145]. Lin et al. (2008) demonstrated that Al_2O_3 NPs results in a significant cellular toxicity in a dose and time dependent manner in human lung epithelial cells. They suggested that the toxicity might be due to the cell membrane depolarization induced by the nanoparticles [146]. Nanosized alumina was shown to induce apoptosis and disrupt the spatial learning behavior in mice due to the mitochondrial impairment [147]. In a study conducted by Shah et al. (2015), the mice exposed to AlNP displayed the induction amyloid beta accumulation, which is the major sign of the Alzheimer's disease. Moreover, neurodegeneration was observed in the cortex and hippocampus of these animals [148].

As indicated specifically, although there are a number of studies related to nanoparticle toxicity, most of them are conducted by using cell lines in vitro

conditions. The *in vitro* studies, on the other hand, are mainly conducted on the nanoparticles which are candidates for drug delivery applications. However, there are no studies assessing the risks of copper, tin and aluminum nanoparticles on the health of workers working in the industry in laser material processing field. To our knowledge, for the first time in the literature, a real-time nanoparticle generation and exposure set up with a material processing laser was designed and the environment was exposed to the rats in real-time.

3.2 Materials and Method

3.2.1 Animals

Four weeks old 35 male Wistar rats were used for this study. Rats were housed under a 12-hour light/dark cycle (lights on at 8 a.m.), in a room maintained at a temperature of 21°C 2°C and a humidity of 60% with free access to water and routine food *ad libitum* daily. All the experimental procedures were approved by Hacettepe University Animal Experimentations Local Ethics Board (B.30.2.2HAC.0.05.06.00/55).

The rats were randomly divided into four groups as CuNP exposure group (n=9), SnNP exposure group (n=9), AlNP exposure group (n=9) and control group (n=8). Control group were exposed to same environment (in the same room with the marking laser system, outside of the cabinet) as the experimental groups except for the nanoparticle exposure. The nanoparticle exposure was performed as 2 hours/day for consecutive 3 months for each material. The exposure duration was determined based on the literature [149, 150]. The exposure setup is shown in figure 3.8 for the CuNP exposure group. During the exposure periods, rats were weighed for once a week. They were also followed up for any weight loss, alteration in food and water consumption, weakness and similar pathologies and none of the animals showed these types of negative symptoms. The weights of the rats are represented in Appendix Figure A.1.

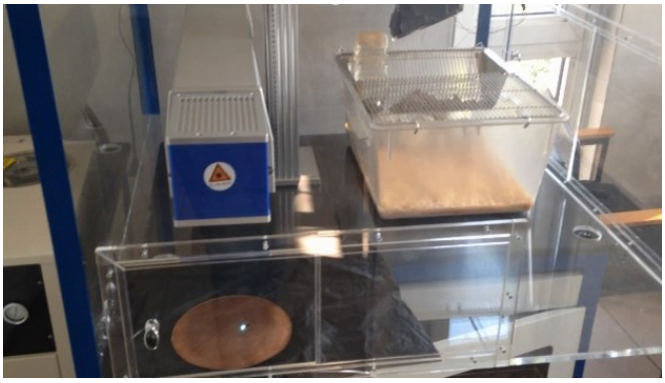

Figure 3.8: The experimental setup where rats were exposed to the laser material processing environment.

3.2.2 Behavioral Tests

After the exposure experiments were completed, the rats were subjected to certain behavioral experiments.

3.2.2.1 Open Field Test

Open field test (OFT) aims to evaluate the locomotor activity, exploration, anxiety and recognition of the spatial novelty recognition parameters [151]. A 50 cm high square glass wall was placed onto a large square black base (45x45 cm size) in our experiments (Figure 3.9).

The black base led to a contrast with the Wistar rats in the data evaluation part. A camera was placed 1.5 meter above the base for the recording. The base was divided into two parts as the 22.5x22.5 cm central part and the side part outside of the central part. In the experiments, the rats were placed into the middle of the system as the face is looking against the certain wall for each time. The rats were allowed to freely explore the chamber for the duration of the test. The recording for each rat was performed for 60 minutes in 24 hours intervals for two times. These recordings were evaluated by using Eyesweb Development Environment (InfoMus, Italy) programme. In the evaluation part, the total distance moved by the rat and the total time spent in the central part and in the

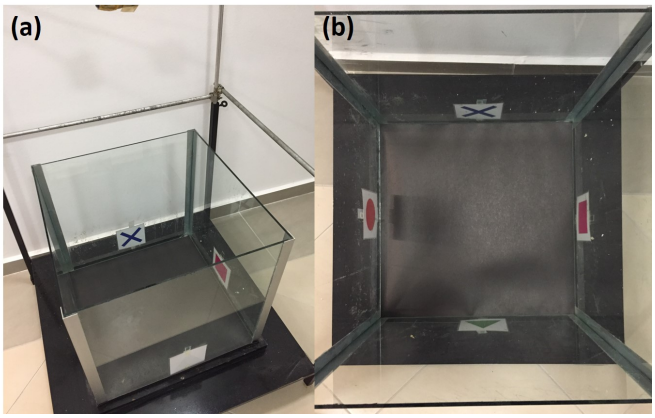

Figure 3.9: Open field test setup to evaluate the locomotor activity, exploration, anxiety and recognition of the spatial novelty recognition parameters of rats after exposure to CuNP, SnNP and AlNP produced during laser material processing. A 50 cm high square glass wall was placed onto a large square black base (45x45 cm size) in our experiments. A camera was placed 1.5 meter above the base for the recording.

side part. The setup was cleaned with 70% ethanol and the base was changed between each experiment.

3.2.2.2 Elevated Plus Maze Test

Elevated plus maze (EPM) test is a standard method used for the determination of stress and anxiety level of the animals [152]. The apparatus used in the experiments consists of two sets of opposing arms 15x40 cm extending from a central region (Figure 3.10).

Two arms are enclosed with 40 cm high walls and the other two arms are open. The platform is 75 cm high from the ground. The recordings were performed with a camera placed to the 2.4 m above the platform. Each rat was placed in the central area of the maze as facing towards the certain open arm. The movement of each rat was recorded for 5 minutes in consecutive 24 hours for two times. The total arm crosses between the open and closed arms and the time spent in the open arms were determined in the data analysis part. The platform was cleaned with 70% ethanol after each test.

Figure 3.10: Elevated plus maze setup to evaluate the stress and anxiety level of the rats after exposure to CuNP, SnNP and AlNP produced during laser material processing. The apparatus used in the experiments consists of two sets of opposing arms 15x40 cm extending from a central region. Two arms are enclosed with 40 cm high walls and the other two arms are open. The platform is 75 cm high from the ground. The recordings were performed with a camera placed to the 2.4 m above the platform.

3.2.2.3 Porsolt's Forced Swim Test

The forced swim test (FST) is a standard behavioral test used for evaluation of the behavioral despair related to the depression [153]. The cylindrical tank (45 cm height x 20 cm diameters) made of transparent glass was used for the rat FST in our experiments (Figure 3.11).

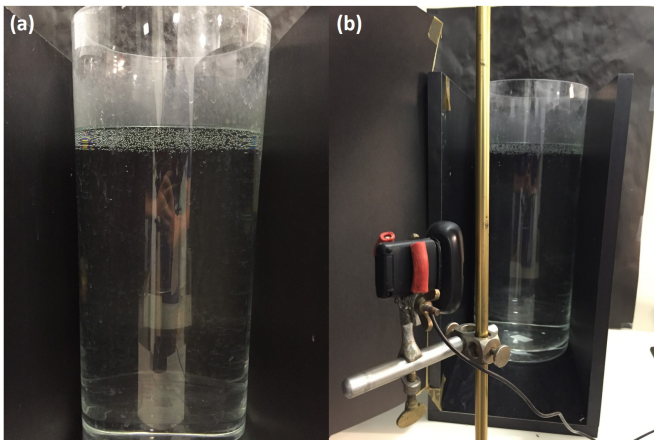

Figure 3.11: Forced swim test setup to evaluate the behavioral despair related to the depression of the rats after exposure to CuNP, SnNP and AlNP produced during laser material processing. The cylindrical tank (45 cm height x 20 cm diameters) made of transparent glass was used for the rat FST in our experiments. The tank was filled with the water up to 35 cm height from the bottom.

The tank was filled with the water up to 35 cm height from the bottom. All the experimental procedures were followed and recorded with a camera and a computer. In the first day, after placing the rat into the water 15 minute recording was performed. After 24 hours, another 5 minute recording was done. In the data analysis part, the 5 minute recording in the second day was evaluated in terms of the immobility duration of the rats.

3.2.2.4 Passive Avoidance Test

Passive avoidance behavior was shown in hippocampal lesions and functional abnormalities [154, 83]. The test depends on the innate preference of rodents for the dark compartment of the passive avoidance test apparatus, and the suppression

of this innate preference after being exposed to an inescapable foot shock. Thus, passive avoidance is an adaptive response to a stressful experience that is used for the evaluation of learning and memory [155]. A two-compartment passive avoidance apparatus was used for our experiments. The apparatus is divided into light (26x30x30 cm) and dark compartments (26x30x30 cm) by a wall with a guillotine door. The bright compartment was illuminated by a halogen lamp (2800 K 1980 lm). The base of the apparatus consisted of steel rods which were located in 15 mm gaps (Figure 3.12)

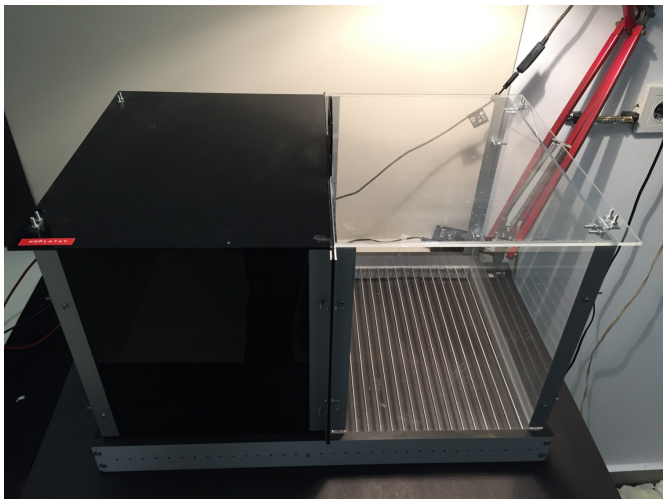

Figure 3.12: Passive avoidance test setup to evaluate the learning and memory process of the rats after exposure to CuNP, SnNP and AlNP produced during laser material processing. A two-compartment passive avoidance apparatus was used for our experiments. The apparatus is divided into light (26x30x30 cm) and dark compartments (26x30x30 cm) by a wall with a guillotine door. The bright compartment was illuminated by a halogen lamp (2800 K 1980 lm). The base of the apparatus consisted of steel rods which were located in 15 mm gaps.

The experiments were conducted in three phases, namely habituation, training and test. In the first day of the test, the rat was placed into the light compartment and 5 s after placing the rat, the door was opened. The duration for the rat to pass to the dark compartment was recorded. If the rat could not pass to the dark compartment within 300 s, the rat placed to its cage and the test was terminated. When the rat passed to the dark compartment, the door was closed, and the rat was placed into its cage. After 5 minutes, training phase started and the same procedure as in the habituation phase was applied to the rat. However, in this

phase, when the rat passed to the dark compartment, the door was closed and a foot shock (square waves of 3 s duration, 50 Hz frequency and 1mA amplitude) was applied. After the shock, the rat was placed into its cage. The test phase was conducted after 24 hours and in this phase the rat was subjected to the same procedure as in the habituation phase. The cut-off was 300 s for test phase.

3.2.3 *In vivo* Electrophysiology

After behavioral tests were completed, *in vivo* electrophysiology experiment were performed as described in Çarçak et al. [156]. Rats were anesthetized with 1.2 g/kg urethane which was injected i.p.. The anesthetized rat was positioned in the stereotaxic instrument. The rat's body temperature was kept constant thoruoghout the experiment at 37°C with the help of a homoeothermic blanket control unit (Harvard Apparatus, USA). Firstly, the skull was exposed with a scalp incision. Burr holes for the stimulation (bipolar wires, made of tungsten, insulated except for the tips; 0.5 mm tip separation) and recording electrodes (made of borosilicate glass) were positioned at the coordinates with reference to bregma [157]. Stimulation electrodes were placed at fimbria-commissure with coordinates of 1.4 mm caudal, 0.5 mm lateral to bregma and 3.8 mm ventral from dura. The field potential recordings were performed from CA1 region. For this purpose, glass microelectrodes (25 M; sharp borosilicate, filled with NaCl 0.9%) were positioned at 4.3 mm caudal, 2.3 mm lateral to bregma and 2.2-2.4 mm ventral from dura. The recording electrode was advanced into the right hippocampus and was aligned to obtain the maximum response in CA1 pyramidal layer. Furthermore, a ground electrode was positioned onto the skull in alignment with the cerebellum. Rectangular pulses with 50 s duration were applied to evoke the field potentials in every 20 s (S44; Grass Instruments, USA) and the stimulation was performed from Schaffer collaterals. The evoked field potential responses were amplified (P16 DC microelectrode amplifier, Grass Instruments), and digitized by using a data acquisition system (PowerLab/8sp, Australia). Before each experiment, to be able to assess the excitability of CA1 neurons, the input/output (I/O) curves in response to stimulation intensities changing between 1 and 15V were

constructed. By using borosilicate glass electrodes, the hippocampal field potential recordings were obtained from stratum radiatum and stratum pyramidale of the hippocampus CA1 region. By using these graphics, the field excitatory postsynaptic potential (fEPSP) threshold and the maximum values were obtained. These data were used in the quantitative evaluation of synapse excitability. In all recordings, the stimulus intensity was adjusted to the value composing the 50% of fEPSP curves. Short term plasticity was evaluated by using paired pulsed stimuli within interpulse intervals of 201000 ms. Long term synaptic plasticity was evaluated from the hippocampal long term potentiation (LTP). Besides LTP induction, CA1 neurons were stimulated in each 20 seconds. After obtaining the baseline recording from stratum radiatum for 10 minutes, LTP was induced with high frequency stimuli (3 times of 100 Hz, 1 second stimuli) and the fEPSP were recorded for the next sixty minutes. The data recordings and evaluation was performed by using Chart 7 (Powerlab, Autralia) programme.

3.2.4 RNA Isolation from Hippocampus Tissue

The hippocampus tissue from the opposite hemisphere of the brain, where *in vivo* electrophysiology was not performed, was isolated from the rats after they were decapitated with guillotine. The isolated hippocampus tissue was placed into RNA*later* solution for the protection of RNA samples. For this purpose, hippocampus tissue were incubated overnight at 4°C in RNA*later* solution. After the overnight incubation, the tissues were removed from RNA*later* and transferred into new microcentrifuge tubes. These hippocampus samples were incubated at -80°C until the RNA isolation. For the determination of the NMDA receptor mRNA expression alterations in the hippocampus upon nanoparticle exposure, the total RNA were isolated. The RNA isolation was performed as described in the literature [158, 159]. 1x phosphate buffered saline (PBS) (Sigma Aldirch, Germany) was prepared by dissolving one tablet into 200 ml of distilled water. Before thawing the tissues removed from -80°C, 1 ml of PBS was added onto the tissues. 1X PBS solution had a 7.4 pH value at room temperature and included phosphate buffer (0.01 M), potassium chloride (0.0027 M), sodium chloride (0.137

M). Tissue samples were centrifuged at 12.000 x g for 40 seconds to remove the RNA*later* solution penetrated into the tissue samples. At the end of the centrifugation process, tissues were transferred to new tubes and 1 ml of TRI reagent (Sigma Aldrich, Germany) was added onto each sample. Glass-teflon homogenizer was used to homogenize the tissue samples and this process was performed on ice. After the homogenization procedure, the samples were incubated at room temperature for 10 minutes and they were centrifuged at 12.000 x g for 10 minutes at 4°C.At the end of centrifugation, the pellet contained the cell debris and it was discarded. The supernatant was taken to another microcentrifuge tube. Each sample was vortexed after the addition of 200 μl of chloroform (Sigma Aldrich, Germany) and they were incubated for 3 minutes at room temperature with the chloroform. The incubated samples were centrifuged at 12.000 x g for 15 minutes at 4°C. Three layers were observed at the end of the centrifugation. Proteins were in the lower layer; DNA was in the interphase and RNA was in the upper aqueous phase. For the successful isolation of total RNA free from any protein and/or DNA contamination, the upper aqueous phase was taken to a new microcentrifuge tube carefully. The samples were incubated at -20°C for 40 minutes with the addition of 500 μl of isopropanol (Sigma Aldrich, Germany) and 2 μl of glycogen for each sample. Following the incubation, samples were centrifuged at 12.000 x g for 25 minutes at 4°C. At the end of the centrifugation, the supernatant was discarded and the pellet was washed with 1ml of 75% ethanol. The samples were centrifuged at 7.500 x g for 5 minutes at 4°C. After the removal of ethanol, 30μl of nuclease free water was added to dissolve isolated total RNA in the pellet. Finally, the isolated RNA samples were incubated at 65°C for 10 minutes to eliminate the possible protein or DNA clusters due to RNA*later* to eliminate their interference to subsequent procedures. The concentrations of the RNA samples were detected with the NanoDrop 2000 (Thermo Scientific, US). 2 μl of the samples were dropped on to the NanoDrop equipment, and the concentrations, A_{260}/A_{280} and A_{260}/A_{230} ratios were measured by the software programme of NanoDrop 2000.

3.2.5 cDNA Preparation

3.2.5.1 Primer Synthesis

The primer design and synthesis was performed according to NCBI gene accession numbers. The primers were designed as they bypass the intronic sequences, and as they bind to end of the previous exon and the beginning of the next exon. Thus, the possibility of these primers to bind to intronic sequences which can be found in a potential contaminating DNA was eliminated with high specificity. The selected primers are listed in Appendix Table A.1 with their corresponding the NCBI accession numbers, oligonucleotide sequences, Tm values, and the volumes of distilled water to prepare 100 μM stock primers. These primers were both used for cDNA synthesis, which was performed with gene specific primers, and the quantitative real time polymerase chain reaction. A 25 μM stock was also prepared from the 100 μM main stock by adding 75 μl of dH_2O to 25 μl of stock primer. Moreover, a 5 μM working solution was prepared by adding 80 μl of distilled water to 20 μl of 25 μM stock. 5 μM working primer solution was used for all the experiments by diluting to desired concentration.

3.2.5.2 cDNA Synthesis

cDNA synthesis was achieved by using the commercailly available RevertAid First Strand cDNA Synthesis Kit (Thermo Scientific, Germany). The concentrations of the RNA samples for cDNA synthesis was adjusted as represented in Appendix Table A.2. Some RNA samples had lower concentrations, thus, the final concentrations showed variety during cDNA synthesis part. However, they were adjusted to equal concentrations in qRT-PCR experiments.

The cDNA synthesis was performed according to the manufacturers protocol. The reagent volumes used in cDNA synthesis reaction are represented in Table 3.2. When all mixtures were prepared for each sample, they were incubated at 42°C for 60 minutes and at 70°C for 5 minutes. Gene-specific primers were used

for cDNA synthesis to increase the specificity.

Table 3.2: cDNA synthesis reagents

The reagent	**Volume**
Template RNA	As in Table 3.2
Gene-specific Forward Primer (5 μM)	2 μl
Gene-specific Reverse Primer (5 μM)	2 μl
5X Reaction Buffer	4 μl
RNase Inhibitor	1 μl
10 mM dNTP solution	2 μl
Reverse Transcriptase Enzyme (M-Mul-V)	1 μl
Nuclease-free water	Complete to 20 μl
Total Volume	**20 μl**

3.2.6 Quantitatve Real Time Polymerase Chain Reaction (qRT-PCR)

SybrGreen Quantitative RT-PCR kit (Sigma Aldrich, Germany) was used for the qRT-PCR reactions and the reactions were performed manufacturers instructions. The reactions were run by using the Corbett Rotor-Gene 6000 (Qiagen, Germany) and the results were reported with the instrument's software. To make sure that the reactions were specific for each gene, melting curves were analyzed in each reaction. Moreover, all reactions were performed in duplicates. Besides the samples, each reaction also included no template control. The final concentrations of all cDNA samples were adjusted to 100 ng final concentration in all qRT-PCR reactions. The optimized qRT-PCR conditions are represented at the following table (Table 3.3).

Table 3.3: Solution volumes and reaction conditions for qRT-PCR

Sybr Green	10 μl
Forward Primer (5 μM)	1.6 μl
Reverse Primer (5 μM)	1.6 μl
MgCl{2}	2.4 μl
cDNA	2 μl
Water	2.4 μl
Total	20 μl

Reaction Conditions

94°C	2 min	
94°C	15 sec	30
60°C	60 sec	cycle
melt		
60°C - 90°C		

The threshold cycles (Cts) for each sample were determined after the qRT-PCR reactions were performed. The expression levels of the NMDAR1 and NMDAR2a were evaluated relative to GAPDH. For this purpose, the described equation for the relative quantification in qRT-PCR was used [160]. This equation allows the calculation even if the efficiencies are not equal in the reactions for the housekeeping gene and the gene of interest in qRT-PCR experiments:

$$Ratio = \frac{(E_{target})^{\Delta \text{Ct Gene of Interest (control - sample)}}}{(E_{housekeeping})^{\Delta \text{Ct Housekeeping (control - sample)}}} \tag{3.1}$$

where E_{target} is the reaction efficiency for gene of interest; $E_{housekeeping}$ is the reaction efficiency of housekeeping gene (GAPDH); Δ Ct is the difference between the Ct values of the control and samples. This efficiency corrected equation was used for the calculation of all changes in mRNA expression levels.

3.2.7 Protein Isolation from Hippocampus Tissue

Since NMDA receptor is located on the membrane fraction of the cell, the total protein isolation from hippocampus tissue was performed by using a commercially available membrane protein isolation kit and according to the manufacturer's procedure (Thermo Scientific, USA). Before the isolation procedure, a commercially available protease and phosphatase inhibitor (Sigma Aldrich, Germany)

was added to the permeabilization and solubilization buffers. The hippocampus tissues, stored in RNA*later*, were removed from -80°C and weighed. 4 mL of cell wash solution was added to approximately 20 mg tissue, vortexed and the wash solution was discarded. 1 mL of permeabilization buffer was added and the tissue was homogenized with the glass-teflon homogenizer system on ice. After obtaining an even homogenization, 1 ml of permeabilization buffer was added onto the homogenized tissue sample and incubated for 30 minutes on ice with constant mixing. After the incubation, the solution was centrifuged at 16.000 x g for 15 minutes at 4°C to pellet the permeabilized cells. The supernatant, containing the cytosolic protein fraction, was transferred to a new microcentrifuge tube. Then, the pellet was dissolved in 1 mL of solubilization buffer and incubated for 30 minutes on ice with constant mixing. After the incubation, the solution was, again, centrifuged at 16.000 x g for 15 minutes at 4°C. At the end of the centrifugation process, the supernatant was containing membrane and membrane-associated proteins. The pellet was discarded. Both cytosolic and membrane-associated proteins were stored at -20°C in aliquots until the western blot analyses.

3.2.8 Determination of Protein Concentrations

Protein concentrations were determined by using the commercially available DC Protein Assay Kit (Bio-Rad) as described in the manufacturer's procedure. DC protein assay kit depends on the reaction of protein samples with an alkaline copper tartrate solution and Folin reagent. The protein samples react with the copper in alkaline medium and then, the copper-treated protein reduces the Folin reagent, as described in Lowry method [161]. The color development is primarily observed because of the tyrosine and tryptophan residues. Also, cystine, cysteine and histidine amino acids lead to color development in a lesser extent [161, 162]. The reduction of Folin reagent happens with the loss of 1, 2 or 3 oxygen atoms and several possible reduced species having a characteristic blue color with a maximum absorbance at 750 nm and minimum absorbance at 405 nm [162].

To determine the concentrations of isolated protein samples, firstly, a bovine serum albumin (BSA) standard was prepared in different concentrations (0.2, 0.4, 0.8, 1.0, and 1.2 mg/ml). Then, the reagent A$'$ was prepared by adding 20 μl reagent S to 1 ml reagent A. 96 well plate was used for the measurement. 5 μl standard and sample were added to the wells. Then, 25 μl reagent A$'$ was added to each well. After the addition of 200 μl reagent B, the plate was mixed for 5 seconds, incubated for 15 minutes at room temperature and the absorbance was measured at 750 nm.

3.2.9 Sodium Dodecyl Sulfate Polyacrylamide Gel Electrophoresis (SDS-PAGE)

SDS-PAGE of the proteins was performed by using a 10% polyacrylamide gel with a Bio-Rad Mini-Protean system (Bio-Rad, USA). The gels were prepared according to Bio-Rad Cell system manufacturers protocol (Table 3.4). The electrophoresis was performed with a constant voltage of 90 V per gel in 1X running buffer (Bio-Rad, USA).

Table 3.4: SDS-PAGE gel preparation

	Resolving Gel	**Stacking Gel**
Resolver A	3 ml	
Resolver B	3 ml	
Stacker A		1 ml
Stacker B		1 ml
10 % Ammonium persulfate	30 μl	10 μl
TEMED	3 μl	2 μl

3.2.10 Western Blot

Proteins were transferred to a PVDF membrane for 30 minutes at 1.3mA/cm2 in semi-dry blotting system (Bio-Rad, USA) using a semi-dry blotting system (Cleaver Scientific Ltd, UK). After the transfer, the membrane was blocked for 1 h with 5% skim milk in Tris buffered saline - Tween 20 (TBS-T) at room temperature. After rinsing for 10 min with TBS-T for three times, the membrane was incubated with the corresponding primary antibody at a dilution of 1:1000 in TBS-T containing 5% skim milk overnight at 4°C. The membrane was rinsed for 10 min for three times with TBS-T and incubated with anti-rabbit IgG-alkaline phosphatase in TBS-T containing 5% skim milk for 1 h at room temperature. The membrane was then washed with TBS-T and developed with substrate (EMD Millipore, USA).

3.2.11 Statistical Analysis

All the data are represented as mean ± SEM. For the statistical analysis of behavioral tests and electrophysiology measurements, one-way ANOVA was used. The one-way ANOVA analysis was further assessed with post-hoc Tukey test. For the mRNA expression and protein level analyses unpaired, two-tailed Student's t test was used. $p<0.05$ was considered as statistically significant.

3.3 Results and Discussion

3.3.1 Behavioral Tests

3.3.1.1 Open Field Test

The locomotor activity, exploration and recognition of the spatial novelty recognition parameters were evaluated with OFT. As a result of this test, in terms of

the total distance moved and the time spent in the central area, there were no statistically significant difference between the CuNP, SnNP or AlNP group when compared to control group (Figure 3.13 a and b, respectively). While CuNP and AlNP group moved less than control group and spent less time in the central part when compared to control group, this difference did not reach to a statistical significance. It can be inferred that the locomotor activity of CuNP and AlNP groups have a tendency to decrease, while the locomotor activity of SnNP is likely to increase after 3 months of nanoparticle exposure. It was shown that acute administration of silver nanoparticles (s.c.) did not affect the locomotor activity of rats tested in OFT [163]. The rats exposed to particulate matter smaller than 2.5 μm for five days in a mobile trailer exposure system displayed increased anxiety-like behavior by spending less time in the center when tested with OFT [164]. Exposure of rats to zinc oxide nanoparticles, on the other hand, did not affect the exploratory behaviors and did not lead to anxiety-related behaviors in rats [165]. When the time spent in the center is considered in this study, CuNP and AlNP treated groups were demonstrated to spend less time in this area compared to control group. This might indicate the anxiety like behavior of these animals. However, it was suggested that OFT is not a primary anxiety test but it might be used as the initial screen of anxiety [166]. Thus, elevated plus maze test was performed to measure the level of anxiety in these nanoparticle treated animals.

3.3.1.2 Elevated Plus Maze

EPM was performed to determine the stress and anxiety level of the rats after CuNP, SnNP and AlNP exposure. In EPM, when the time spent in the open arm for the nanoparticle exposed groups is compared to the control group, AlNP group showed a statistically significant increase ($^{***}p<0.001$) (Figure 3.14a). Although CuNP group, also, spent more time in the open arms than control group, the difference is not statistically significant. The time spent in the open arms and the number of entry to open arm indicate the decreased anxiety-like behavior in elevated plus maze [167]. It might be speculated that AlNP group show less

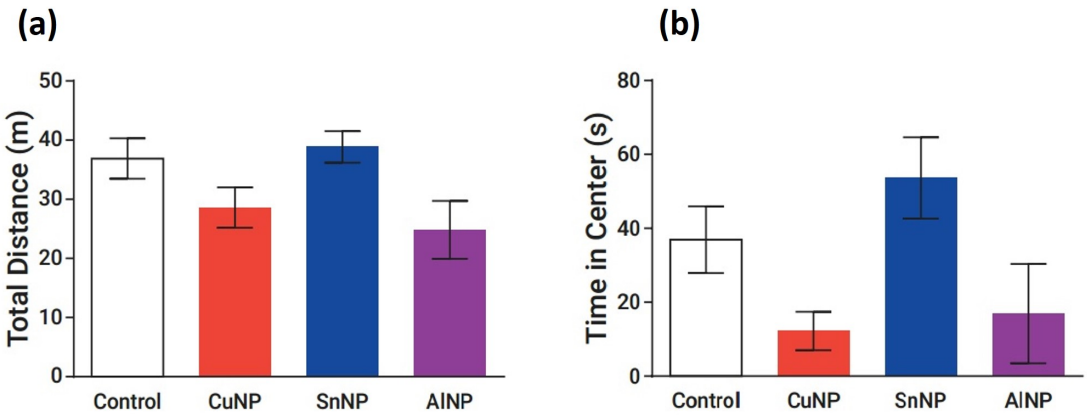

Figure 3.13: CuNP, SnNP and AlNP produced during the laser material processing did not alter the locomotor activity of rats exposed to these nanoparticles. There is no statistically significant difference between the CuNP, SnNP or AlNP group when compared to control group in terms of (a) total distance moved and (b) time spent in the central part. However, the decrease in the time spent in the central area in CuNP and AlNP exposed rats might indicate the increased anxiety like behavior in these rats.

anxiety-like behavior compared to control. On the other hand, in total arm crosses data, there is no statistically significant difference between any of the nanoparticle exposed group and the control group, in accordance with the OFT results (Figure 3.14b). In the literature, there are anxiety studies upon exposure to different nanoparticles. One such study showed that exposure to particulate matter smaller than 2.5 μm did not lead to anxiety-like behaviors in rats tested with elevated plus maze [164]. Similarly, silver nanoparticle exposure did not result in anxiety in rats [163]. On the other hand, it was shown that TiO_2 injection led to a decrease in the time spent in the open arms and in the number of crosses, indicating their increased anxiety behavior, compared to control [168]. Furthermore, nanoscale particulate matters were collected from vehicular gases and mice were exposed to these particles in aerosols. The study demonstrated that these vehicular-derived nanoparticles did not cause the anxiety in mice [169]. In this study, it was also demonstrated that CuNP, SnNP and AlNP did not result in anxiety like behavior in rats exposed to these nanoparticles. Moreover, AlNP exposed rats displayed decreased anxiety in EPM compared to control group.

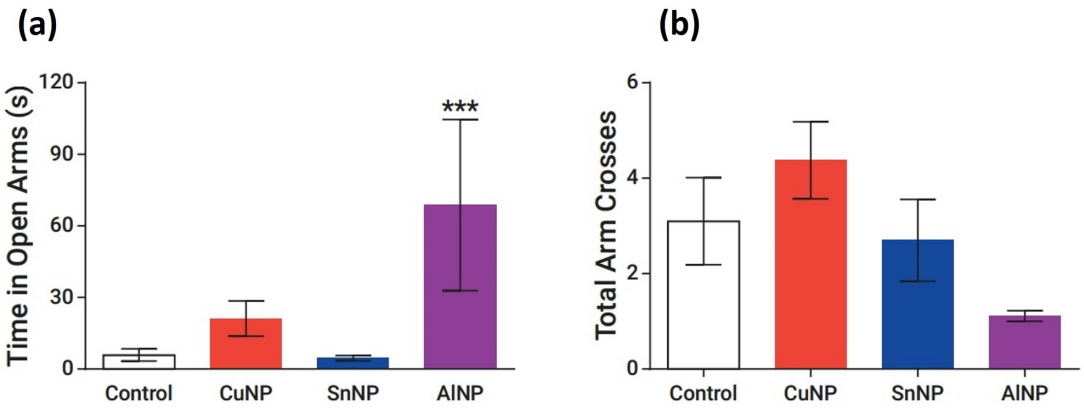

Figure 3.14: CuNP and SnNP did not lead to anxiety of rats exposed to these nanoparticles while AlNP resulted in a decrease in anxiety behavior of the rats after exposure. (a) Time spent in the open arms and (b) the total arm crosses were evaluated in the EPM test for each group. AlNP group spent statistically significantly more time in the open arms when compared to control group ($^{***}p<0.001$), which indicates that AlNP exposure led to decrease in the anxiety. No statistically significant difference was detected in the total arm crosses.

3.3.1.3 Porsolt's Forced Swim Test

Porsolt's FST was performed for the evaluation of behavioral despair in the rats after CuNP, SnNP and AlNP exposure. For this purpose, the immobility duration of the rats was analyzed [170]. None of the nanoparticle exposed groups demonstrated statistically significant difference when compared to control group (Figure 3.15). However, CuNP and AlNP groups showed less immobility behavior when compared to control group. In the literature, there are not much studies about the effects of nanoparticles on behavioral despair and depression-like behavior. It was shown that zinc oxide administration led to positive changes in forced swim test of the rats, which had high immobility durations before the administration [165]. In this study, on the other hand, no significant change was observed after CuNP, SnNP and AlNP exposure in the rats compared to control group in terms of immobility duration. Thus, it might be concluded that CuNP, SnNP and AlNP exposure did not result in the depression-like behavior in nanoparticle exposed rats.

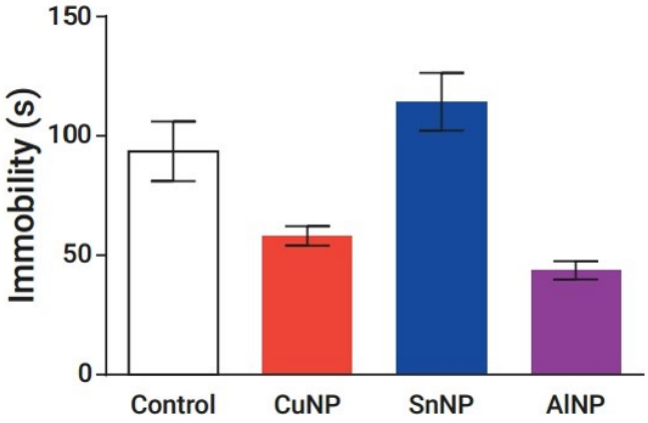

Figure 3.15: CuNP, SnNP and AlNP produced during the laser material processing did not result in behavioral despair in the rats exposed to these nanoparticles. Although CuNP and AlNP groups showed less immobility than controls, there is no statistically significant difference in any of the nanoparticle exposed groups when compared to control group.

3.3.1.4 Passive Avoidance Test

Passive avoidance test was performed for the evaluation of learning and memory in rats after CuNP, SnNP and AlNP exposure. The latency period in the test phase was evaluated. None of the nanoparticle exposed groups demonstrated difference when compared to control groups in terms of latency duration in the light compartment (Figure 3.16). Ghaderi et al. (2015) demonstrated that subcutaneous silver nanoparticle injections to rats, similarly, did not affect their performance in passive avoidance test [163]. It was demonstrated that the offsprings of the rats which were administered TiO_2 in pregnancy via gavage, displayed altered memory at the 48^{th} hour of passive avoidance test [171]. Moreover, intraperitoneally injected gold nanoparticles were shown to cause an impairment in the memory ability of the rats [105]. In our study, on the other hand, it was shown that CuNP, SnNP and AlNP did not alter the learning and memory of the rats after three months of exposure.

It was shown that CuNP, SnNP and AlNP did not affect the learning memory ability of the exposed rats. However, there are some minor changes in their mood compared to control group, as shown by OFT, elevated plus maze and forced

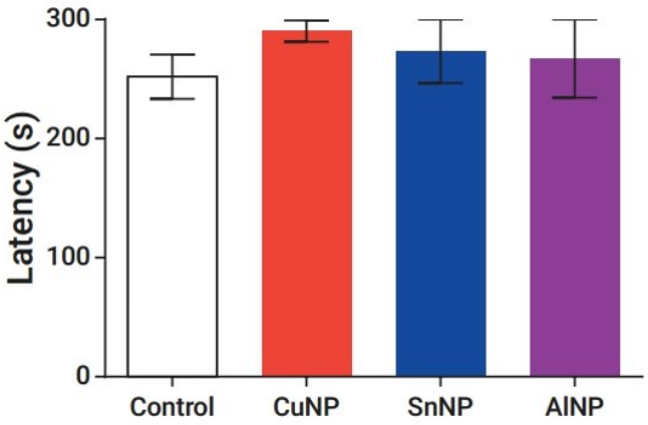

Figure 3.16: CuNP, SnNP and AlNP produced during the laser material processing did not affect the learning and memory process of the rats exposed to these nanoparticles. None of the nanoparticle exposed groups demonstrated statistically significant difference when compared to control groups in terms of latency duration in the light compartment.

swim test.

3.3.2 *In vivo* Electrophysiology

In vivo electrophysiology is one of the methods for the evaluation of hippocampal learning. Since the pyramidal neurons and their dendrites are orderly arranged in CA3 and CA1 regions of hippocampus, electrical field recordings give significant information about the temporal arrangement of neuronal responses. Here, the basic synaptic transmission from CA3 to CA1 region of hippocampus was determined. After stimulating the ventral hippocampal commissure, population spike amplitudes in stratum pyramidale did not show any difference between CuNP, SnNP and AlNP groups when compared to control group (Figure 3.17a). Similarly, EPSP slopes and population spike amplitudes were evaluated from the recordings taken from CA1 stratum radiatum. Although there is a tendency to decrease in the EPSP slope, there is no statistically significant difference between the nanoparticle exposed groups and the control group (Figure 3.17b). Both EPSP slopes and population spike amplitudes reveal the basic synaptic transmission from CA3 region to CA1 region of the hippocampus, in this experimental

procedure. More specifically, these data provide information about both the presynaptic neurotransmitter release and postsynaptic receptor response [172]. Thus, it can be suggested that CuNP, SnNP and AlNP did not affect the synaptic transmission in CA1 region of the hippocampus, indicating no alteration in the number and excitability of the neurons in this region.

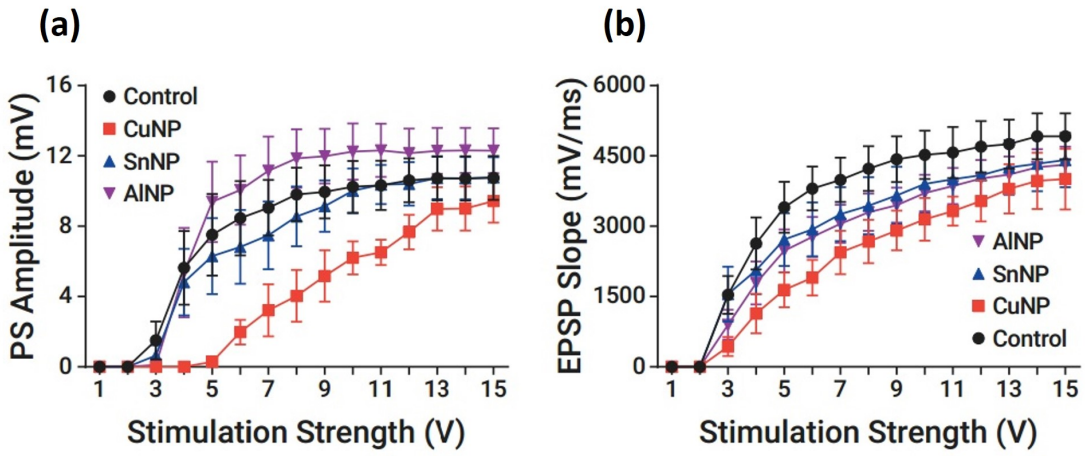

Figure 3.17: CuNP, SnNP and AlNP did not affect the synaptic transmission in CA1 region of the hippocampus of the rats after exposure to these nanoparticles. (a) Population spike and (b) EPSP slope amplitudes from the recordings taken from CA1 stratum pyramidale and stratum radiatum, respectively, after stimulating the ventral hippocampal commissure. Both EPSP slope and population spike amplitude did not show statistically significant difference between the nanoparticle exposed groups and the control group.

On the other hand, paired-pulse facilitation gives information about the activity-dependent short-term synaptic plasticity and it is detected when two stimuli are delivered to presynaptic fibers in very short time interval[173]. After stimulating the ventral hippocampal commissure, recordings from CA1 stratum radiatum were also evaluated in terms of the ratio between EPSP slopes which were induced with two stimuli with different interpulse intervals in between (Figure 3.18a). Moreover, the ratio of population spike amplitudes were analyzed in the same situation (Figure 3.18b). Neither of the nanoparticle exposed groups showed statistically significant difference than the control group in terms of $(EPSP_s2)/(EPSP_s1)$. Therefore, it can be inferred that no facilitation was observed in CA1 region of the rats exposed to CuNP, SnNP and AlNP.

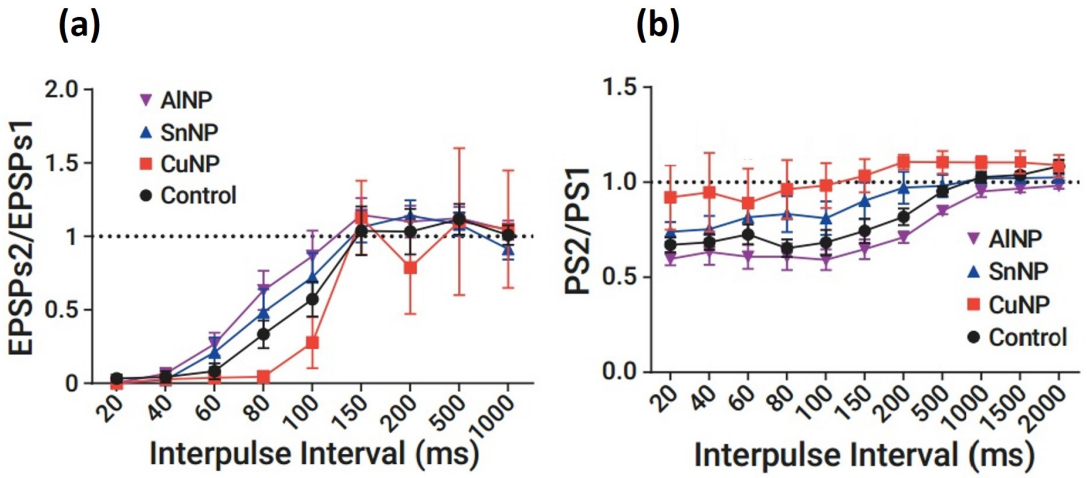

Figure 3.18: CuNP, SnNP and AlNP did not result in any facilitation in CA1 region of hippocampus of the rats exposed to these nanoparticles. (a) Ratio of the EPSP and (b) ratio of population spike amplitudes from the recordings taken from CA1 stratum pyramidale and stratum radiatum, respectively, after stimulating the ventral hippocampal commissure. Neither of the nanoparticle exposed groups showed statistically significant difference than the control group in terms of $(EPSP_s2)/(EPSP_s1)$.

Finally, LTP analysis was performed to evaluate the hippocampal learning and memory process. LTP was induced by stimulating the ventral hippocampal commissure with a high frequency stimulation (HFS). The data were normalized by taking the ratio of the EPSP slopes after the induction and before the induction. The recording was taken from the CA1 stratum radiatum. CuNP and AlNP groups were induced less than the control group in a statistically significant manner ($^{**}p<0.01$); but in the long term no statistically significant difference was observed (Figure 3.19). Thus, it can be inferred that copper, tin and aluminum nanoparticle exposure did not affect the long-term memory process in nanoparticle exposed rats. These data are also consistent with the passive avoidance test data, indicating no alteration in the memory process.

Previously, it was demonstrated that intraperitoneal CuO nanoparticle injection to rats for consecutive 14 days led to a decrease in EPSP slopes obtained from CA1 region of the hippocampus, indicating that CuO nanoparticles negatively affected the synaptic transmission [174]. In this study, although there is

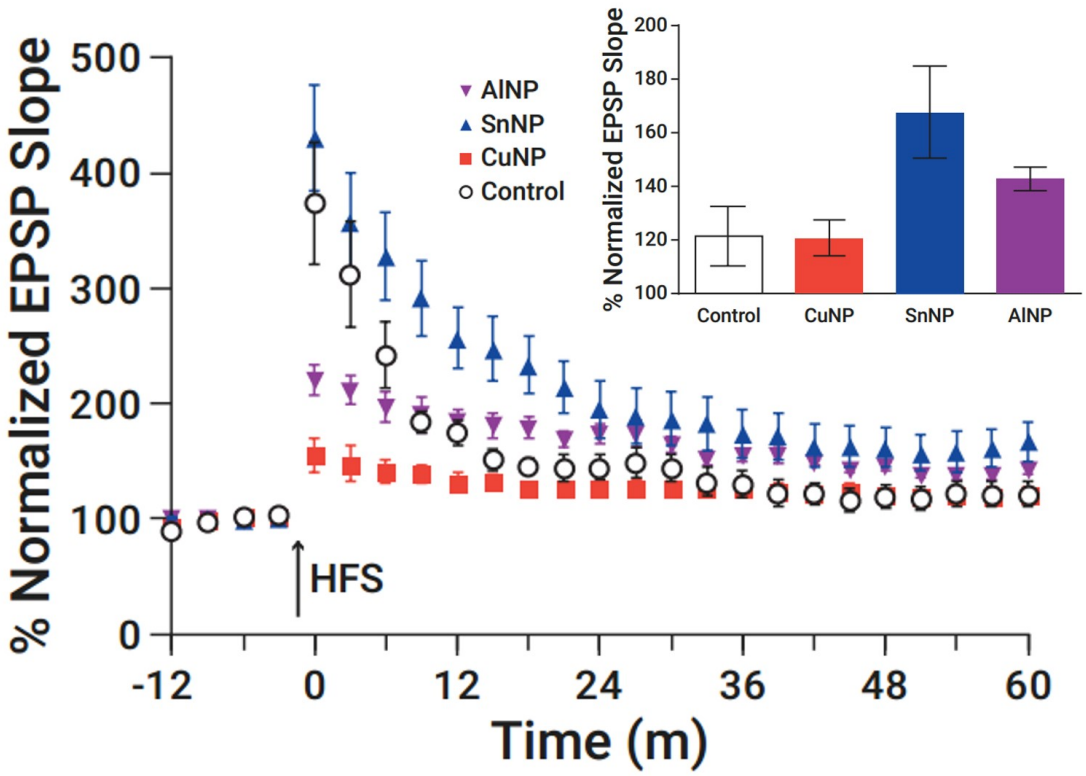

Figure 3.19: CuNP, SnNP and AlNP exposure did not affect the long-term memory process in nanoparticle exposed rats. CuNP and AlNP groups were induced less than the control group in a statistically significant manner ($^{**}p<0.01$); but in the long term no statistically significant difference was observed.

a tendency for decrease in EPSP slope in CuNP treated group, it did not reach to statistical significance. Moreover, silver nanoparticles were administered to rats as nasal drops and EPSP was shown to significantly decrease compared to control group. Thus, the LTP measurement also showed a decrease in long term potentiation in silver nanoparticle exposed group [115]. On the other hand, intraperitoneally injected ZnO nanoparticles were shown to enhance the long term potentiation in rats [175]. It was shown in this study that CuNP, SnNP and AlNP did not affect the synaptic transmission, number and excitability and the facilitation of the neurons in CA1 region of the hippocampus. Moreover, there was no significant difference between the nanoparticle exposed groups and the control group in terms of LTP analysis, indicating that these rats had intact learning and memory process after 3-months of nanoparticle exposure. The exposure routes in the literature are generally through injections or nasal drops. Thus, the exposure dose might be much higher than the dose inhaled throughout this real time exposure experiment. Therefore, the dose of the nanoparticles reaching to the hippocampus might not be enough to alter the synaptic transmission patterns.

3.3.3 RNA concentrations

Concentrations of isolated RNA samples and A_{260}/A_{280} and A_{260}/A_{230} were determined as described previously. The results are represented in the Appendix Table A.3. RNA concentrations were displayed in ng/μl. The values of A_{260}/A_{280} values between 1.80 - 2.00 indicate the purity of RNA, which is free from DNA contamination. The results indicate that the isolated RNA samples do not contain contaminants and they are pure.

3.3.4 Protein concentrations

Concentrations of isolated proteins from the rats hippocampus tissues were determined with DC Protein Assay and the concentrations are presented in Table Appendix table A.4.

3.3.5 Fold changes in the expression levels of NMDAR1 and NMDAR2a genes and NMDAR1 protein levels

The calculation of the fold change was performed as relative to the housekeeping gene, GAPDH, for both control and nanoparticle exposed groups according to the efficiency corrected equation 2.1. The differences in the gene expressions are depicted in Fig.3.20 and 3.21 for NMDAR1 and NMDAR2a genes, respectively, as bar graphs.

Although CuNP exposure did not lead to a statistically significant change in NMDAR1 expression, both SnNP and AlNP resulted in an increase in the expression level ($^{***}p<0.001$). CuNP exposed group demonstrated a decrease to 0.63 ± 0.30, while SnNP and AlNP showed an increase by 3.42 ± 0.19 and 3.24 ± 0.46 fold in NMDAR1 expression. Similarly, SnNP and AlNP exposures resulted in a statistically significant increase in NMDAR2a expression (23.18 ± 3.67, $^{**}p<0.01$ and 20.88 ± 4.23, $^{***}p<0.001$, respectively. CuNP exposure did not affect the expression level of NMDAR2a compared to control group (1.09 ± 0.01).

CuNP and SnNP resulted a decrease in NMDAR1 protein levels to 0.44 ± 0.11 and 0.59 ± 0.07 fold compared to control group, respectively ($^{**}p<0.01$ for both groups). (Figure 3.22). However, NMDAR1 protein levels did not show a statistically significant decrease in AlNP exposed group (0.84 ± 0.06).

NMDAR1 subunit is the obligatory subunit of NMDAR and together with either or both the NMDAR2a and the NMDAR2b subunit, they constitute the functional NMDAR [176]. The number and the type of NMDAR2 subunits affect the allosteric modulation by polyamines and the ligand affinities [177]. Thus, we wanted to check the expression changes in NMDAR1 upon CuNP, SnNP and AlNP exposure. NMDAR is one of the most important targets for the heavy metal toxicity [178]. NMDARs have recognition sites for a number of ligands which can be both endogenous and exogenous. These ligands might be divalent metal cations and they might exert toxic effects on these receptors [178, 179]. The

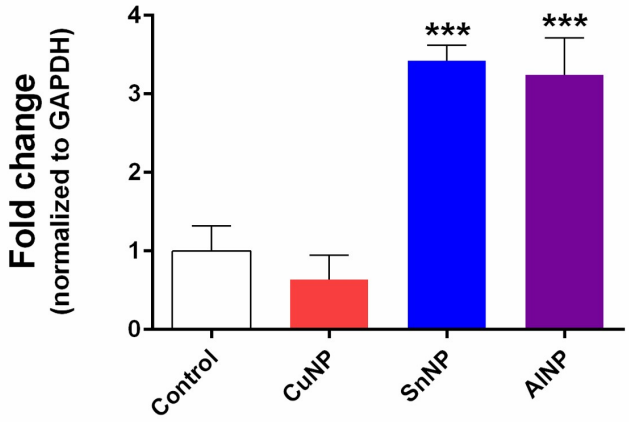

Figure 3.20: CuNP exposure did not lead to a statistically significant change in NMDAR1 mRNA expression. However, both SnNP and AlNP resulted in an increase in the mRNA expression level of NMDAR1 in hippocampus of the rats after exposure to these nanoparticles. Although CuNP exposure did not lead to a statistically significant change in NMDAR1 expression detected by qRT-PCR, both SnNP and AlNP resulted in an increase in the expression level ($^{***}p<0.001$). CuNP exposed group demonstrated a decrease to 0.63 ± 0.30, while SnNP and AlNP showed an increase by 3.42 ± 0.19 and 3.24 ± 0.46 fold in NMDAR1 expression.

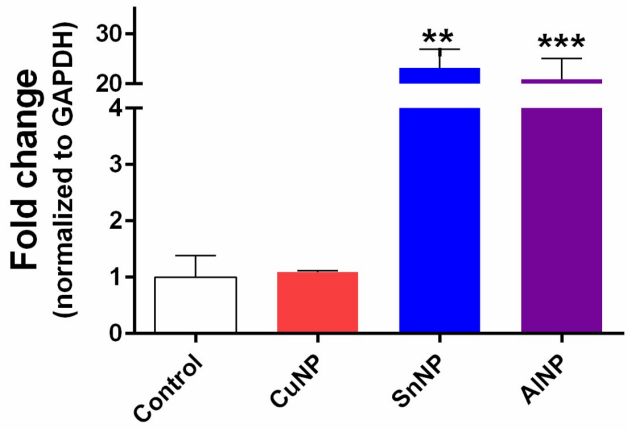

Figure 3.21: SnNP and AlNP exposures resulted in a statistically significant increase in NMDAR2a expression in hippocampus of the rats after exposure to these nanoparticles. SnNP and AlNP exposures resulted in a statistically significant increase in NMDAR2a expression (23.18 ± 3.67, $^{**}p<0.01$ and 20.88 ± 4.23, $^{***}p<0.001$, respectively. CuNP exposure did not affect the expression level of NMDAR2a compared to control group (1.09 ± 0.01).

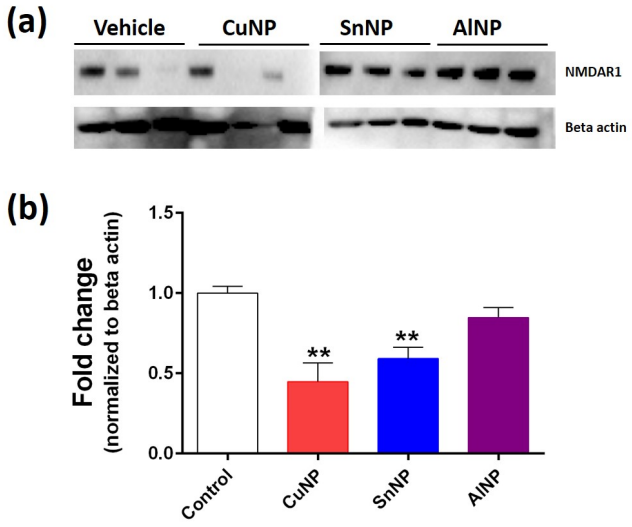

Figure 3.22: CuNP and SnNP resulted a decrease in NMDAR1 protein levels in hippocampus of the rats after exposure to these nanoparticles. CuNP and SnNP resulted a decrease in NMDAR protein levels to 0.44 ± 0.11 and 0.59 ± 0.07 fold compared to control group, respectively ($^{**}p<0.01$ for both groups). However, NMDAR1 protein levels did not show a statistically significant decrease in AlNP exposed group (0.84 ± 0.06).

effect of the divalent cations were shown to be dependent on NMDAR2 subunit of NMDARs [180]. Mg^{2+} and Zn^{2+} have significant physiological roles through interaction with NMDAR and this makes it possible to classify other divalent ions as Mg^{2+}like (voltage-dependent) or Zn^{2+}like (voltage-independent) [181]. Therefore, NMDAR2a expression was also analyzed in this study. Cu, Sn and Al are also divalent cations and although they are in nanoparticle form in the exposure, they might also be ionizing in the tissues. Cu^{2+} was shown to inhibit NMDAR activity [182]. In this study CuNP did not affect the expression of NMDAR1 and NMDAR2a significantly, but it decreased the NMDAR protein level in a statistically significant manner, which might be related to the inhibition of receptor activity. Although there are no studies about the effect of Sn on NMDAR in the literature, again being a divalent cation, Sn might affect the receptor expression and protein levels. The increase in the NMDAR1 expression might be the feedback mechanism to elevate the decreased NMDAR1 protein levels. Aluminum, on the other hand, was shown to alter the downstream pathway of NMDAR [183]. Thus, it might be inferred that AlNP, by disrupting the downstream cellular

pathways of NMDAR, might lead to increase in the gene expression of NMDAR1 and, as a result, a stable protein level. It was shown that NMDAR1 and NMDAR2a are differentially expressed in different regions of hippocampus, such as CA1, CA3 and dentate gyrus [184]. In this study, the synaptic activity outputs were recorded from CA1 region but RNA and protein isolation were performed from whole hippocampus tissue. This might be the reason why there is an alteration in mRNA and protein levels of NMDAR subunits but no change in long term potentiation. It might also be suggested that, other subunit NMDAR2b might be affected after nanoparticle treatment which might be the limiting factor in NMDAR protein levels, resulting in the NMDAR1 protein levels in the membrane were decreased.

3.4 Conclusion

For the first time in the literature, the real time nanoparticle exposure setup was developed to mimic the industrial environment for the determination effects of nanoparticles on the rats' learning and memory process. Both behavioral tests and *in vivo* electrophysiology experiments revealed that 3 months of copper, tin and aluminum nanoparticles exposure did not lead to any alterations in the learning and memory process of the rats. However, AlNP led to a decrease in the anxiety like behavior of the rats exposed to these nanoparticles. Thus, it can be concluded that AlNP resulted in a mood change in these animals. Moreover, it was demonstrated that NMDAR subunits NMDAR1 and NMDAR2a mRNA expressions were significantly increased in SnNP and AlNP exposed groups. Moreover, NMDAR1 protein levels were shown to decrease after CuNP and SnNP exposure compared to controls. It might be concluded that CuNP, SnNP and AlNP produced during laser materials processing might lead to changes in mRNA and protein levels of NMDAR after three months of exposure. Although this change was not reflected to the synaptic transmission and behavior, in long term exposure there is a high risk to alter the learning and memory functions, together with neurodegeneration.

Chapter 4

Localization and Body Distribution of Nanoparticles

4.1 Introduction

As described in chapter 3, a real-time exposure set-up with laser marking system was designed and the nanoparticles were administered to the rats in this environment for the first time in the literature. Besides reaching to brain, these nanoparticles are predicted to reach a number of organs in the body via circulation. Although there are studies showing the body distribution of the nanoparticles upon different exposure routes, the experimental setup mimicking the real time industrial environment was used for the first time in this thesis study. Inhaled particles, nano and micron sized particles, were shown to pass to the circulation from lungs [185]. The fate of the particles taken into the body through inhalation and their accumulation in the respiratory tract depends on the size of the particles [186, 187]. It was determined that large particles, which are 530 μm in size, show their effects in nasopharyngeal region. Smaller particles (1-5 μm) were shown to be accumulated in tracheobronchial region. However, nanoparticles reach into the alveolar region, where the elimination mechanisms are not sufficient [188]. Although respiratory tract has different structural and functional methods

to deal with inhaled particles, these mechanisms are not sufficient for the high doses of the inhaled particles [189, 190, 191]. The inhaled nanoparticles might be eliminated from the lung but it requires a long time. Moreover, the interaction of the nanoparticles to the cells results in the adverse effects in the lung [191]. The elimination mechanism of the lung for inhaled particles is through alveolar macrophage-mediated clearance but it might not be successful for the nanoparticles, which macrophages lead them to get closer to the alveolar epithelium and get into the bloodstream [192, 193]. If the nanoparticles aggregate in the tissue and form larger particles, they can be recognized by alveolar macrophages and eliminated by phagocytosis [194]. Thus, nanoparticles gain access to the target organs by passing to bloodstream from the lung alveolar epithelium and might exert their toxic effects [10]. As introduced in chapter 3, CNS is protected by the BBB and nanoparticles were shown to pass BBB and reach to different parts of the brain in a number of studies [106, 8]. In this study, by using a novel exposure setup for the fist time in the literature, the rats were exposed to the CuNP, SnNP and AlNP and we determined the body distribution of these nanoparticles in rat organs and plasma samples.

4.2 Materials and Methods

4.2.1 Removal of the Organs

After completing the *in vivo* electrophysiology experiments, the rats were sacrificed with a guillotine while the rats are still under the urethane anesthesia. The trunk blood was collected right after they were sacrificed. The skull was opened and the brain was removed. The frontal cortex, hippocampus, occipital lobe, hindbrain, and cerebellum samples were collected in the artificial cerebrospinal fluid (ACSF) buffer at 0°C. Then, lung, heart, kidney, spleen, adrenal glands, and testis samples were also removed. While the samples for TEM analysis were kept in the 2.5% gluteraldehyde solution, the samples for ICP-MS analysis were stored at -80°C. Moreover, the hippocampus sample from the other hemisphere

was removed. This sample was further kept at at 4°C overnight in RNA*later* solution (Qiagen, Germany). The samples were removed from the solution by the forceps and passed into a new microcentrifuge tube to be stored at -80°C until RNA and protein isolation processes.

4.2.2 TEM Analysis of the Tissue Samples

All the tissue samples were fixed in 2.5% gluteraldehyde for 24 hours. Then, the samples were washed in Sorensons Phosphate Buffer (SPB, pH: 7.4), postfixed in 1% osmium tetroxide. After this step, the samples were re-washed with SBP to reach the dehydration step. The samples were dehydrated by using increasing concentrations of alcohol (25%, 50%, 75% and pure alcohol). Then the tissues were washed with propylene oxide twice and embedded the media which was prepared by mixing 1:1 propylene oxide and epoxy resin embedding material. The samples were incubated in this mixture for 1 hour and at the end of this incubation period, the same amount of epoxy resin embedding material was added to the mixture and the ratio of the mixture was increased to 1/3. The samples were incubated in the rotator overnight in this mixture and the preparation for the embedding part was completed. By embedding the samples into plastic capsules with the epoxy resin embedding material, the samples were incubated in 60C incubator for 48 hours. At the end of 48 hours, the samples were taken out of the incubator and semi-thin sections about 2 m in thickness were cut with ultramicrotome (LKB-Nova, Sweden). Semi-thin sections were stained with methylene blue and examined by an Optiphot (Nikon, Japan) light microscope to determine the area to be sectioned further. After trimming procedure of these semi-thin sections, ultrathin sections at a thickness of 60 nm were taken by ultramicrotome, collected on copper grids, stained with uranyl acetate and lead citrate, and examined with a transmission electron microscope (JEOL JEM 1200 EX, Japan).

4.2.3 ICP-MS Analysis of the Tissue Samples

The tissue samples stored at -80°C were weighed and approximately 250 mg tissue sample for used in the analysis. The weighed tissue samples were placed into polytetrafluoroethylene (PTFE) microwave tubes and 8 ml concentrated HNO_3 was added onto the sample. The tissues were homogenized in the tissue digestion microwave oven at 180°C, 45 bar pressure for 35 minutes. All the chemical reagents used in ICP-MS analysis were high-purity grade solvents. HNO_3 was purchased from Sigma Aldrich, Germany and hydrochloric acid (HCl) was purchased from Merck, Germany. The internal calibration standard was bismuth (Bi) at a concentration of 10 ppb. All of the standards were purchased from High Purity Standards, USA. The water used in all ICP-MS procedures was deionized water with 18 MΩcm. The ICP-MS analysis was performed by internal standard correction and standard curve formation for each of the elements. The samples were diluted to 1:50 with 2% HNO_3 for copper measurement, 1:12.5 with 5% HNO_3 and 5% HCl for tin and 1:25 with 1% HNO_3 for aluminum. The measurement was performed with the ICP-MS equipment from Thermo-Scientific, USA.

4.3 Results and Discussion

TEM analyses revealed that CuNP, SnNP and AlNP reached to a number of organs. The summary of the organs in which nanoparticles were detected are listed in Table 4.1. Moreover, TEM images of control tissues and the tissue samples collected from CuNP, SnNP and AlNP exposed rats are demonstrated in appendix figures B1-B12. TEM images revealed that all the nanoparticles were distributed in both extracellular matrix and in the cytoplasm of the cells. This indicates that CuNP, SnNP and AlNP were taken into the cells, which might be a risk for the toxicity of these nanoparticles in specific tissues.

To confirm the the TEM images, quantification of the elements in organs was performed with ICP-MS analysis. The quantitative results are represented

Table 4.1: Distribution of CuNP, SnNP and AlNP in rats' organs according to TEM results. The presence of nanoparticles is indicated with the "X" sign in the table.

Sample	CuNP	SnNP	AlNP
Heart		X	X
Lung	X	X	X
Kidney	X	X	X
Adrenal Glands	X	X	X
Liver		X	X
Testis	X	X	X
Spleen	X		X
Intestine			
Hippocampus			
Cerebellum	X		X
Hindbrain		X	
Frontal Cortex	X		X
Occipital Lobe			X

in appendix table B1. Copper concentrations increased significantly in heart ($^{*}p<0.05$), lung ($^{****}p<0.001$), liver ($^{**}p<0.01$) and frontal cortex ($^{*}p<0.05$) (Figure 4.14). Although not statistically significant, copper concentration increased in testis, spleen, cerebellum, hindbrain and occipital lobe. Since copper has a number of roles in the body for the normal physiological pathways [119, 120], as described previously in chapter 3, control tissues also exhibited certain levels of copper.

Tin, on the other hand, normally is not present in the body and after SnNP exposure, tin element was detected in all the tissues analyzed although there are tissues tin increase is not statistically significant (Figure 4.16). Similarly, aluminum was detected in all of the investigated tissues, except for the olfactory bulb (Figure 4.17). Besides, only copper was found significantly higher in plasma among three elements (Figure 4.18). Tin and aluminum plasma concentrations in SnNP and AlNP exposed rats were similar to that of control group. The plasma aluminum concentration in the control group is consistent with the literature

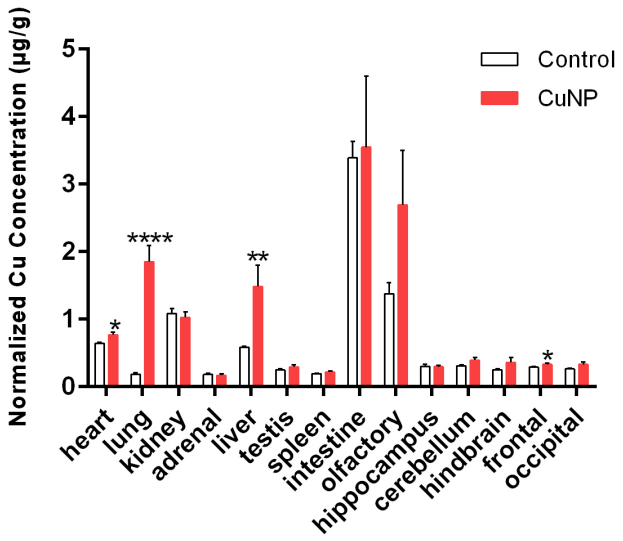

Figure 4.1: Cu element concentration in the tissues of CuNP exposed rats. Cu element was shown to be increased in heart ($^{*}p<0.05$), lung ($^{****}p<0.0001$), liver ($^{**}p<0.01$) and frontal cortex ($^{*}p<0.05$) in a statistically significant manner. Testis, spleen, cerebellum, hindbrain and occipital lobe copper concentrations also increased.

[195].

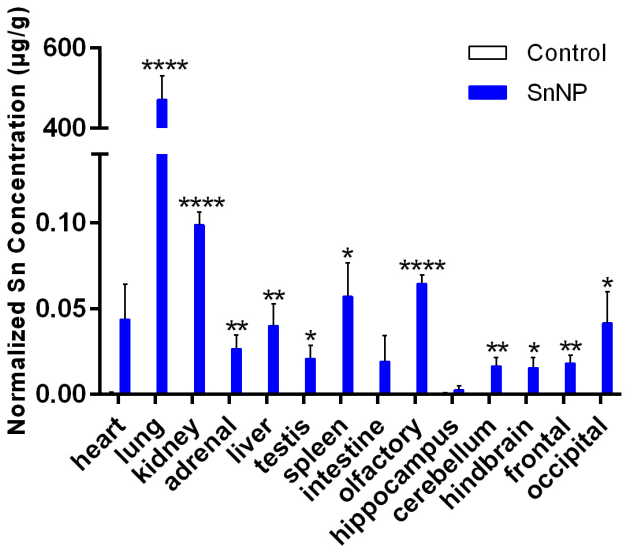

Figure 4.2: Sn element concentration in the tissues of SnNP exposed rats. Sn element was shown to be increased statistically significantly in all of tissues analyzed except for the heart and hipocampus ($^{*}p<0.05$, $^{**}p<0.01$, $^{****}p<0.0001$). Although not statistically significant, the Sn concentration increased also in heart and hippocampus tissues.

In the ICP-MS analyses, it was demonstrated that all of the three nanoparticles are distributed throughout the body to various organs. There are some differences between the TEM data and ICP-MS data since although a number of slices are prepared and investigated in TEM analyses there might be some part of the tissues where nanoparticles cannot be detected. Thus, TEM data is considered as the supportive data of ICP-MS analysis.

In this study, it was demonstrated that CuNP, SnNP and AlNP generated during laser material processing were taken into the body of rats exposed to this environment via inhalation. More significantly, it was shown that these nanoparticles are distributed to a number of organs such as lungs, heart, liver, spleen, testis and so on, together with a number of brain regions. In the literature, there are some studies investigated the body distribution of nanoparticle which were administered to animals through different routes. Figure 4.15 describes the potential routes. De Jong et al. (2008) injected gold nanoparticles to the tail vein of the

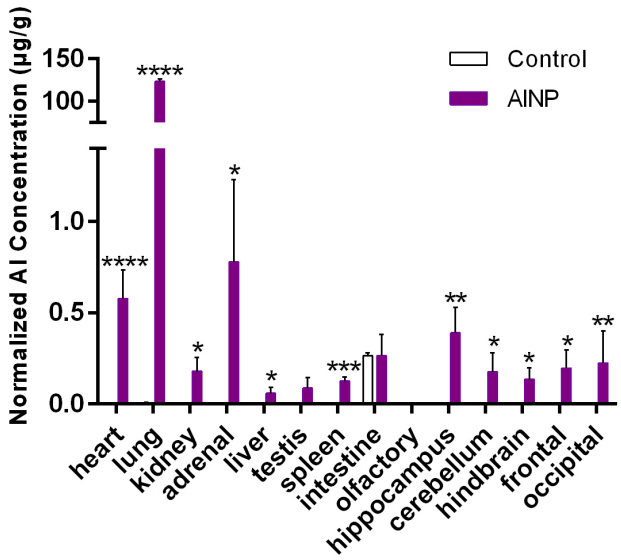

Figure 4.3: Al element concentration in the tissues of AlNP exposed rats. Al element was shown to be increased statistically significantly in all of tissues analyzed except for the testis ($^{*}p<0.05$, $^{**}p<0.01$, $^{***}p<0.005$, $^{****}p<0.0001$). Although not statistically significant, the Al concentration increased also in testis.

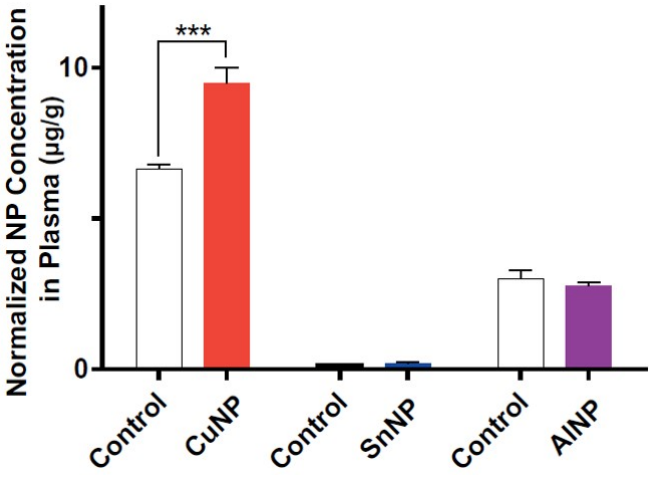

Figure 4.4: Cu, Sn and Al element concentrations in the plasma of CuNP, SnNP and AlNP exposed rats, respectively. Cu element was found to be increased statistically significantly when compared to control group ($^{***}p<0.001$).

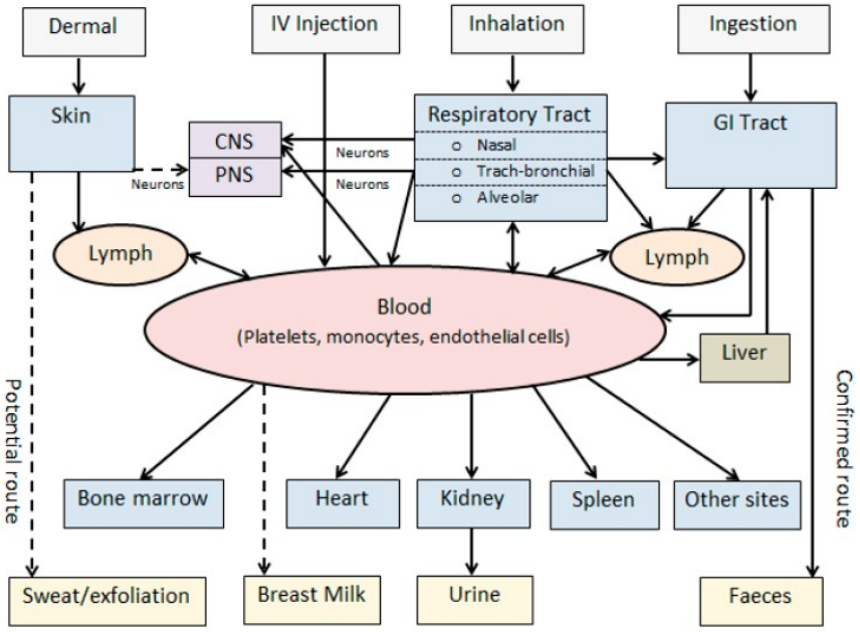

Figure 4.5: Potential routes of nanoparticles upon exposure. Adapted from [196].

rats and they showed the size-dependent body distribution of the nanoparticles. They detected the smallest nanoparticles in blood, heart, lungs, liver, spleen, kidney, thymus, brain, and reproductive organs of the rats [197]. TiO_2 nanoparticles were included in the drinking water of the mice and it was revealed that there is a significant increase in the cytokine expression in peripheral blood, suggesting the systemic distribution of nanoparticles throughout the body [198]. In a study conducted with the whole-body exposure set-up, TiO_2 in aerosols were exposed to mice for 10 days as the subacute exposure. It was demonstrated that there was a significant inflammatory response in the lungs of the exposed mice [199]. Silver nanoparticles administered to rats through oral gavage for 28 days were detected in liver, kidney, lungs, muscles, brain, plasma, small intestine and stomach [200]. In another study comparing the silver nanoparticles and silver ions, when silver nanoparticles were administered to rats by oral gavage for 28 days, on the other hand, the nanoparticles were detected in testis, kidney, brain, lung and blood of the animals [201]. The rats, which were exposed to silver nanoparticles through inhalation for 6h/day, 5 days/week for 13 weeks, were examined in terms of body distribution of the nanoparticle and silver nanoparticles were detected in liver,

kidneys, olfactory bulb, brain, lungs and whole blood [116]. Moreover, orally administered silver nanoparticles were detected in rats' testes, kidneys, liver, brain, lungs, stomach and blood [202].

Upon inhalation, lung was shown to be the first target organ for the nanoparticles to reach and result in inflammatory reactions [203]. In this study, it was shown that CuNP, SnNP and AlNP were distributed to a number of target organs such as heart, liver, kidney, testis. Moreover, there is a high concentration of nanoparticles detected in the lung tissue. Since laser material processing led to a wide range of size distribution, it might be inferred that larger nanoparticles might have accumulated in the lung tissue while smaller ones reached to bloodstream and to the target organs. On the other hand, only Cu was shown in the plasma, but all Sn and Al were transferred to the organs. Since the nanoparticles might be transferred to the target organs via circulation, it is not surprising to detect increased Cu, Sn and Al concentrations in the heart. Liver, on the other hand, was shown to be one of the most preferential organ for the nanoparticle accumulation since hepatocytes are highly perfused with the blood [204]. Moreover, since spleen and liver are the organs in the reticuloendothelial system, there is a high chance for nanoparticles to get into these tissues [205]. On the other hand, the nanoparticles detected in the kidney might again be due to renal clearance of nanoparticles from the bloodstream [206]. Furthermore, in a number of studies, it was shown that inhalation and other routes of nanoparticle exposure led to the disruption of male reproductive functions by reaching to testis after passing the testis-blood barrier and affecting the testosterone synthesis and sperm production [207, 208]. Moreover, since there is no significant increase in intestine for all of the exposed nanoparticles compared to control, the exposure route was only through inhalation but not digestion. One of the striking findings of this study is that Cu, Sn and Al were detected in a number of brain regions. The nanoparticles might reach to the brain either by disrupting the BBB or through the olfactory bulb. Cu and Sn were detected in olfactory bulb while no Al was observed in this region. Al might either only reach to brain through the circulation and BBB or it might surpass and not accumulated in the olfactory bulb. By reaching to different brain parts, these nanoparticles would affect a number of pathways in

central nervous system and they might lead to neurodegeneration and apoptosis of neurons upon accumulation.

4.4 Conclusion

The material processing laser setup, which is mimicking the industrial working environment, was used to expose the rats to nanoparticles generated during the material processing. To our knowledge, this is the first study in the literature in which a real time exposure setup was used and the body distribution of these nanoparticles were investigated. Cu, Sn and Al were detected in a number of organs of the rats upon inhalation. The lack of these elements in the intestine indicates that the major route of entry was inhalation. Although we cannot completely rule out the oral route, it seems to be a very minor path of entry for NPs. Lungs, the primary target organs after the inhalation, were detected with the high element concentrations indicating the accumulation of these nanoparticles in the lungs. 1.85 $\pm$ 0.24 μg/g copper, 471.26 $\pm$ 60.30 μg/g tin, 123.44 $\pm$ 2.99 μg/g aluminum were detected in the lungs of CuNP, SnNP and AlNP exposed groups, respectively. The nanoparticles also reached to a number of organs through systemic circulation, such as heart, liver, kidney, spleen, and testis. Moreover, these nanoparticles were shown to reach a number of brain parts either by passing through the BBB or via olfactory bulb or through both of the routes. For instance, 0.33 $\pm$ 0.01 μg/g copper, 0.02 $\pm$ 0.00 μg/g tin, 0.20 $\pm$ 0.09 μg/g aluminum were detected in the frontal cortex of CuNP, SnNP and AlNP exposed groups, respectively Detection of these nanoparticles in different brain parts shows the severity of risk in terms of neurodegeneration and the apoptosis of neuron cells. The body distribution results indicate that nanoparticles produced during laser materials processing might lead to a number of health risks in human upon inhalation.

Chapter 5

Nanoparticle Toxicity

5.1 Introduction

In this chapter, two different studies related to *in vitro* toxicity of different nanoparticles, which were produced by pulsed laser ablation in liquids, will be introduced. The nanotoxicity of silver nanoparticles were investigated in the isolated rat hippocampus tissue in the first study and it was revealed that silver nanoparticles are taken into the body through phagocytosis. Moreover, it was shown that silver nanoparticles led to the decrease in cell survival in dose-dependent manner. In the second study, the nanotoxicity of CuNP, SnNP and AlNP was analyzed in human neuroblastoma cell line in terms of the effects on cell survival and NMDAR subunit mRNA expression and protein levels. It was demonstrated that CuNP, SnNP and AlNP led to the cell death with increasing nanoparticle concentrations and CuNP and SnNP resulted in alterations in NMDAR1 mRNA and protein levels.

5.2 Toxicity of Internalized Laser Generated Pure Silver Nanoparticles to the Isolated Rat Hippocampus Cells

Nanoparticles are used in a number of different applications in medical, biological, electronic, and industrial fields. One of the most commonly used types of nanoparticles in those applications is the silver nanoparticles (AgNP). They are used as therapeutics; cosmetics; antimicrobial coatings on medical implants, catheters, wound dressings and so on [209]. AgNPs are also utilized as imaging agents because of their unique plasmon-resonance optical scattering properties [210]. Central nervous system has a high risk of nanoparticle exposure since the nanoparticles can reach the brain both by systemic circulation and through the olfactory bulb via the olfactory mucosa [131, 132]. It was shown that AgNPs are detectable in the brain after inhalation and it was proposed that nanoparticles gain access to the brain through the BBB either by passive diffusion or by carrier mediated endocytosis [211]. It was demonstrated that AgNPs results in BBB destruction and neuronal degeneration [212]. Moreover, orally administered AgNPs were found to be accumulated in the brain [213]. One recent study showed that learning ability and memory retention was severely damaged and there was edema in hippocampus after nasally administered AgNPs in rats [115]. AgNPs caused alterations in the expression profiles of the genes related with motor neuron disorders, neurodegenerative diseases and immune cell function [214]. Sung et al. (2009) conducted a whole-body inhalation study to AgNPs at different doses. AgNPs were shown to accumulate in the liver, olfactory bulb, brain, and kidneys. It is important that brain has a high risk due to the transfer of AgNPs from olfactory neurons after inhalation [215]. Similarly, Ji et al. (2007) investigated the body distribution of AgNPs upon inhalation and the nanoparticles were detected in liver, brain, olfactory bulb, and spleen [216]. The effects of AgNPs on gene expression in different regions of the mouse brain was also investigated. The particles were administered to adult male mice via intraperitoneal injections and it was demonstrated that gene expression changed in the caudate nucleus, frontal cortex, and hippocampus of mice when treated with the

Ag NPs [217]. As indicated in a number of studies, AgNP can pass the blood brain barrier and reach to brain, with the potential of neurotoxicity in a number of different brain regions. Hippocampus was chosen for our study since it is the major brain region responsible for learning and memory. Moreover, hippocampus is shown to be highly susceptible to cell death [218]. The cellular effects of AgNPs were studied in various mammalian cell lines in *in vitro* settings [219, 220, 221]. AgNPs were shown to be toxic to mitochondria [222] due to oxidative stress leading to inflammation, DNA damage and finally apoptosis [223]. It is known that AgNPs can accumulate in the brain [149] and damage learning and memory retention via reactive oxygen species (ROS) in rats [224]. Furthermore, AgNPs altered the expression of genes related with motor neuron disorders, neurodegenerative diseases and immune function [225]. Although AgNPs have been considered as safe and commonly used in drugs, cosmetics, etc. for decades, recent studies suggest that AgNPs would lead to serious toxicity in the nervous system as well as other systems. In order to exert intracellular toxic effects, nanoparticles should be taken into the cell and interact with macromolecules. The cellular uptake mechanism for nanoparticles is various forms of endocytosis depending on their physicochemical properties [226]. Surface chemistry is the main determinant of nanoparticle toxicity [227]. So far, studies on AgNPs have all used coated nanoparticles (polyvinylpyrrolidone, antibodies, surfactant, or chemical byproducts) resulting in different surface chemistries while uncoated pure AgNP toxicity is yet to be elucidated. Since pure uncoated AgNPs are the most common silver nanoparticles in nature and in industry as products or byproducts such as during laser ablation, it is important to determine their mechanism for internalization which is correlated with their toxicity [96]. In this study, we produced pure uncoated AgNPs without any chemical surface modifications by using laser ablation method and aimed to investigate the direct toxicity of the AgNPs to the neural tissue and their mechanism of internalization by the neurons in rat hippocampal slices.

5.2.1 Materials and Methods

5.2.1.1 Animals and Hippocampal Slice Preparation

3 weeks old male Wistar albino rats were used for procedures involving hippocampal slices. After anaesthetizing by diethyl ether, the animals were rapidly decapitated, hippocampi were removed and transverse slices at thickness of 400 m were cut in oxygenated, 50 ml of ice-cold dissection buffer [low Ca^{2+}/high Mg^{2+} artificial CSF (ACSF)], using a Vibroslice (World Precision Instruments, FL, USA). Oxygen was supplied using a 95% O_2, 5% CO_2 gas mixture (carbogen). All animal experiments were approved by Hacettepe University Animal Experimentations Local Ethics Board (number: B.30.2.HAC.0.05.06.00/50).

5.2.1.2 Nanoparticle production and characterization

A 99.99% pure silver block was used as the target of a laser beam to produce the AgNPs with laser ablation method as described previously [2]. Nanoparticles were produced by a commercial nanosecond pulsed ND:YLF laser (Spectra Physics Empower Q-Switched Laser, CA, USA) operating at 527 nm with 100 ns pulse duration and 16 W average output power at 1 kHz pulse repetition rate corresponding to a pulse energy of 16 mJ. The silver block was placed in a glass vessel containing 20 ml of pure deionized water. The laser beam was focused on the target by the help of a plano-convex lens with a focal length of 50 mm. The height of liquid layer over the target was approximately 5 mm. The laser ablation was carried out for 5 minutes by the beam scanning over the target surface, creating a solution with dispersed nanoparticles in the liquid medium. The silver block was weighed before and after the ablation process and the concentration of the AgNP solution was determined to be 0.1 mg/ml. UVVisNIR spectrophotometer (Agilent Technologies Varian Cary 5000, CA, USA) analysis was performed for the determination of characteristic absorbance spectrum of the AgNPs. The structural and topographical properties of AgNPs were analyzed using a scanning

electron microscope (SEM, FEI Quanta 200 FEG, OR, USA). Further morphological analysis of the AgNPs were done by using a transmission electron microscope (TEM, FEI Tecnai G2F30) together with the elemental characterizations by using energy dispersive X-ray (EDX) analysis. TEM samples were prepared by dropping the AgNP solution onto a carbon-coated TEM grid.

5.2.1.3 Administration of AgNPs to hippocampal slices for TEM analysis

After hippocampal slice preparation, obtained slices were incubated at 37°C in ACSF for 60 minutes with three different incubation environments as described in figure 5.1. The ACSF solution consisted of the following (in mM): 124 NaCl, 5 KCl, 12 NaH_2PO_4, 26 $NaHCO_3$, 10 D-glucose, 2 $CaCl_2$, 1 $MgCl_2$ and was oxygenated using 95% O_2 and 5% CO_2. KCl with a final concentration of 4 M was added into one of the AgNP incubation solutions to check whether the AgNPs are located in the pre-synaptic vesicles in hippocampus cells. It is known that high K^+ concentration leads to a stimulated synaptic vesicular recycling; thus it helps to demonstrate the AgNPs in the presynaptic vesicles, if any [228].

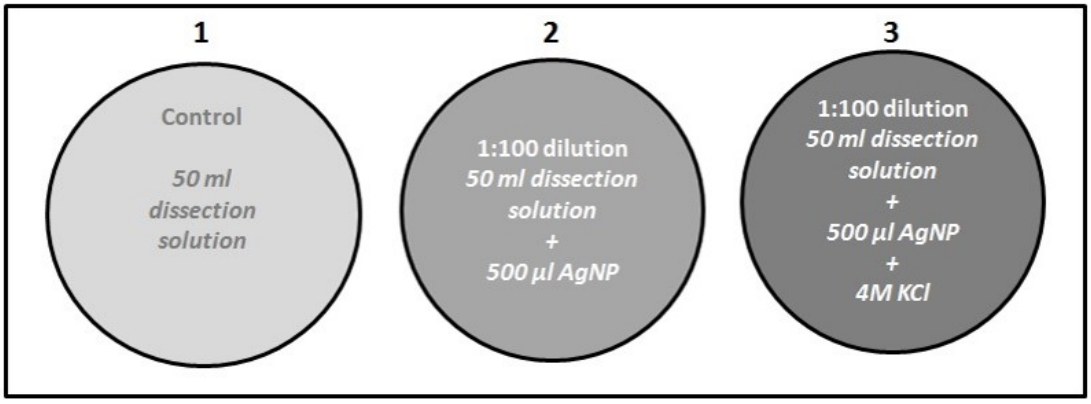

Figure 5.1: Rat hippocampal slice incubation with pure AgNPs. Control slices were incubated with dissection buffer solution as shown in condition 1. For the experimental group, condition 2 included 500 μl AgNP and 50 ml dissection buffer solution to achieve 1:100 dilution and condition 3 included additional 4M KCl for high K^+ administration to check whether the AgNPs are located in the pre-synaptic vesicles of hippocampal neurons.

5.2.1.4 Sample preparation and TEM analysis of the hippocampal slices

The incubated hippocampal slices were fixed in 2.5% gluteraldehyde for 24 hours. Then, the samples were washed in Sorensons phosphate buffer (SPB, pH: 7.4), postfixed in 1% osmium tetroxide. Following this step, the samples were re-washed with SBP to reach the dehydration step. The samples were dehydrated by using increasing concentrations of alcohol (25%, 50%, 75% and pure alcohol). Then the tissues were washed with propylene oxide twice and embedded in the media which were prepared by mixing 1:1 propylene oxide and epoxy resin embedding material. The samples were incubated in this mixture for 1 hour and at the end of the incubation period, the same amount of epoxy resin embedding material was added to the mixture and the ratio of the mixture was increased to 1/3. The samples were incubated in the rotator overnight in the resulting mixture and the preparation for the embedding part was completed. The samples were incubated in 60°C incubator for 48 hours after being embedded into plastic capsules with the epoxy resin embedding material. At the end of 48 hours, the samples were taken out of the incubator and semithin sections about 2 m in thickness were cut with ultramicrotome (LKB-Nova, Sweden). The sections were stained with methylene blue and examined by an Optiphot (Nikon, Japan) light microscope to determine the area to be sectioned further. After trimming procedure of these semithin sections, ultrathin sections at a thickness of 60 nm were taken by ultramicrotome, collected on copper grids, stained with uranyl acetate and lead citrate, and examined with a transmission electron microscope (JEOL JEM 1200 EX, Japan).

5.2.1.5 Cell Viability Assay

For the investigation of cell viability, we have chosen five different AgNP concentrations; 10, 15, 20, 25 and 30 mg/L. Control slices were incubated without nanoparticles in ACSF solution. All groups were oxygenated with carbogen mixture except a second nanoparticle-free group which was treated with hypoxic

conditions as the positive control group to assess the baseline metabolic activity. After incubating the hippocampal slices with the AgNPs for 60 minutes, the slices were removed from the incubation solution and further incubated with 0.5 mg/ml 3-(4,5-dimethylthiazol-2-yl)-2,5-diphenyltetrazolium bromide (MTT, Sigma Aldrich, Germany) solution for 60 minutes at 37°C. Then, 4 mM acidified isopropanol was added to the solution to solubilize the formazan crystals formed at the end of the reaction. The absorbance was measured at 570 nm by using a microplate reader (BioTek Synergy HT, VT, USA).

5.2.1.6 Statistical Analysis

The statistical analysis of MTT cell viability assay was performed by one-way ANOVA with post-hoc Tukey test to compare control group to the experimental groups. A p value below 0.05 was accepted as statistically significant.

5.2.2 Results and Discussion

To our knowledge, this is the first study evaluating the toxicity of the pure uncoated AgNPs produced by laser ablation method by administration to the hippocampal tissue. In this study, i) AgNP treatment caused cell death in a dose-dependent manner. ii) Pure AgNPs were localized in the cytoplasm rather than organelles; ii) AgNPs were taken up by hippocampal neurons via phagocytosis; iii) This endocytosis pathway was separate from the vesicular recycling pathway since stimulation of vesicular recycling did not increase the AgNP uptake; iv) This endocytosis pathway preferentially selected the large AgNPs.

5.2.2.1 Produced uncoated pure AgNPs were spherical and did not aggregate

The AgNPs were produced in deionized water at a concentration of 0.1 mg/ml and the production was observed as the change of color to yellow appearance

(Figure 5.2a). The optical absorption spectrum of AgNPs was determined by UV-Vis absorption spectroscopy. Figure 5.2b shows that the optical absorption spectrum of AgNPs giving the specific silver peak at 406 nm, which is consistent with the literature [229].

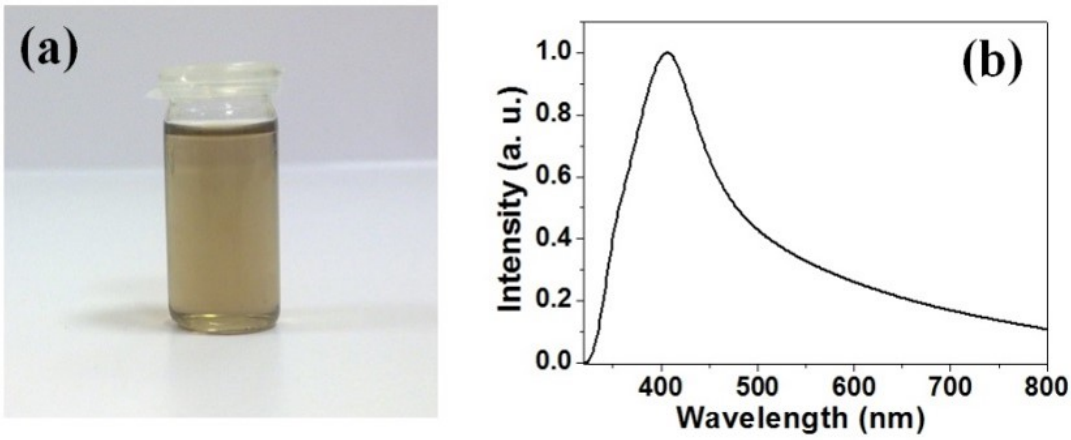

Figure 5.2: Optical properties of pure AgNPs (a) The image of 0.1 mg/ml AgNP solution produced by laser ablation method. No precipitation was detected for at least for 4 months; (b) Absorption spectrum exhibited absorbance peak at 406 nm corresponding to AgNP.

First, we evaluated the size distribution of nanoparticles produced by laser ablation method from pure silver. In SEM images (Figure 5.3a), most of the AgNPs were found to be smaller than 100 nm in diameter but there were also larger AgNPs that were up to approximately 500 nm in diameter. The nanoparticles were also shaped spherically. The TEM analysis was performed to further characterize the AgNPs and determine their structure (Figure 5.3b). The TEM results confirmed the SEM results in terms of shape and size of the AgNPs. Furthermore, the nanoparticles showed no aggregation pattern in the TEM images. The TEM images also demonstrated that the AgNPs had a crystal structure. EDX analysis was performed for further confirmation of the purity of AgNP solution. As shown in the inset of figure 5.3b, the solution was consisting of carbon (C), copper (Cu) that belongs to the TEM grids, and silver (Ag) as can be determined from the peaks corresponding to those elements. Thus, there was no interference of any impurity during the AgNP administration to the hippocampus tissue.

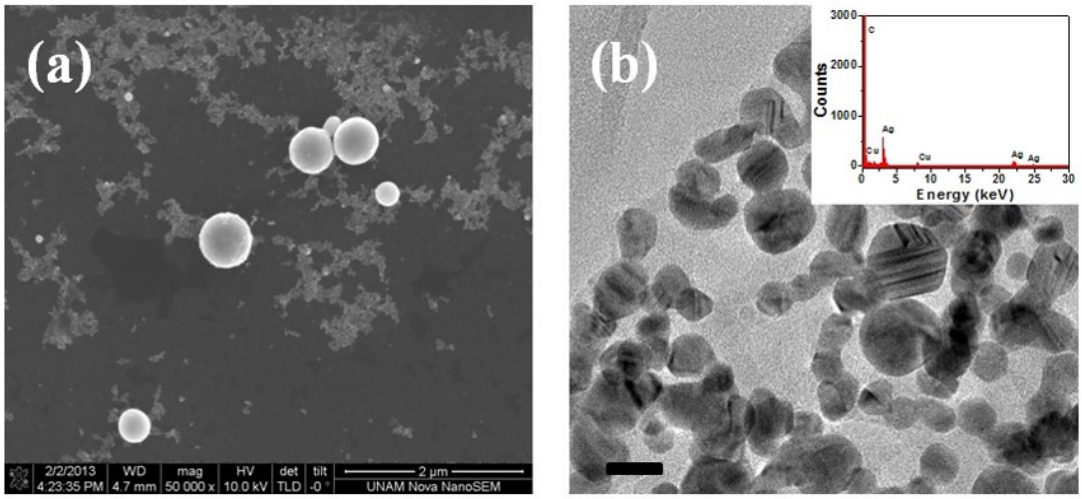

Figure 5.3: Representative SEM and TEM images. (a) SEM image of AgNPs (2 μm scale bar); (b) TEM image of the AgNPs (20 nm scale bar); the inset corresponds to EDX analysis of the AgNP sample. The solution consisted of carbon (C), copper (Cu), which belonged to TEM grids, and silver (Ag) as can be determined from the peaks corresponding to those elements, indicating no interference of any other impurity in AgNP solution

The broad size distribution of nanoparticles is considered as a drawback of the laser ablation method in the nanoparticle synthesis. To control the size, surfactant materials are used so that the nanoparticles can be produced in a specified size range [230]. However, this would affect the purity and most probably change the behavior of the AgNPs in the biological environment. For this study, purity was a significant parameter to determine the AgNP localization in the hippocampal tissue, therefore we avoided using surfactants. Furthermore, the broad size distribution obtained by the laser ablation method is an advantage to mimic the industrially occurring nanoparticles in real life settings. It was shown that the shape of the nanoparticles are strongly correlated with their cellular uptake rates, with rod-shaped nanoparticles show the highest uptake rate, followed by spheres, cylinders, and finally cubes [231]. We assume that production of spherical nanoparticles by laser ablation method increased their phagocytosis. Besides the importance of shape and size in cellular uptake, aggregation is an important feature that nanoparticles exhibit and generally a number of nanostructures exert their toxic effects upon aggregation [232]. In this study, aggregation was not observed in TEM results before tissue administration, thus, whether the AgNPs

would aggregate or not depended on their behavior inside the tissue.

5.2.2.2 Rat hippocampal neurons internalize AgNPs by phagocyctosis

Electron microscopy was performed to visualize the distribution of AgNPs in extracellular and intracellular areas of the neural tissue. TEM analysis displayed that the AgNPs were distributed both in the extracellular and the intracellular matrices (Figures 5.4b, c, d). Additionally, we never observed the presence of AgNPs inside a specific organelle; rather, they were always distributed in the cytoplasm. Small AgNPs below 100 nm in diameter were only found in the extracellular matrix while larger nanoparticles were present in both extra- and intracellular regions. Moreover, phagocytosis of an AgNP by a hippocampal neuron was also observed and photographed in the TEM analysis (Figure 5.4e).

Our TEM results of the tissues exhibited the distribution of large size nanoparticles in both intracellular and extracellular regions. Small AgNPs below 100 nm in size were found to be exclusively localized in the extracellular region, showing that the internalization mechanism solely works for nanoparticles larger than a specific size. Furthermore, the internalized nanoparticles were observed only in the cytoplasms of the hippocampal cells and not in the organelles. Previous studies on the cellular localization of AgNPs in tissues other than hippocampus show that these nanoparticles can be found in membrane-bound organelles. One group showed that the starch-coated AgNPs were taken into glioblastoma cells and were localized in the endosomes and lysosomes [233]. In our study, the AgNPs were not found in endosomes. This might be due to the endosomal escape phenomenon, in which nanoparticles tend to escape the endosomes or lysosomes and are distributed in the cytoplasm freely [234]. Alternatively, our pure nanoparticles may be not subject to the same uptake and distribution mechanisms as coated nanoparticles since nanoparticles bind to different sets of proteins and lipids based on their coatings.

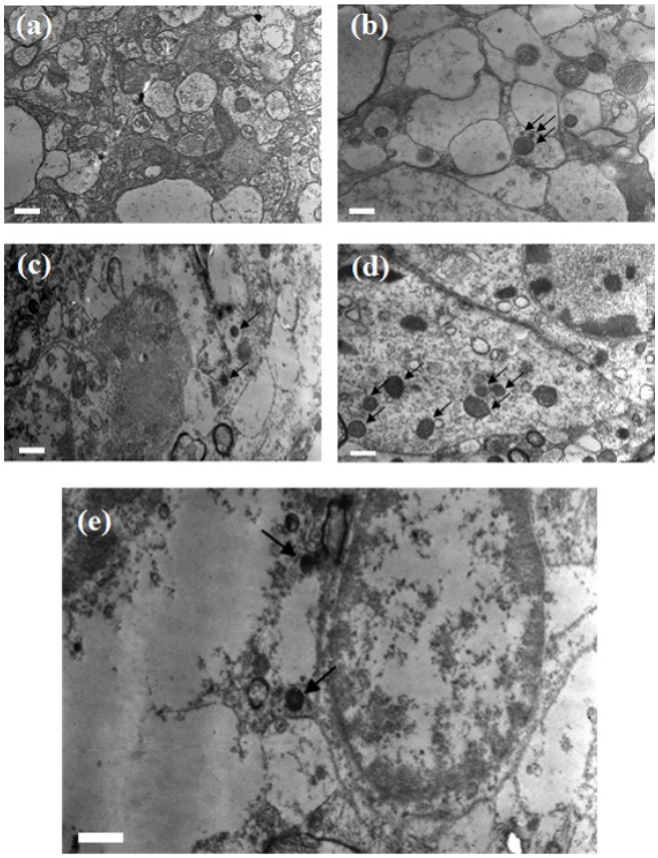

Figure 5.4: TEM images showing AgNP distribution in hippocampal slice treated with AgNPs, (a) control; (b, c) AgNPs in the extracellular region; (d) AgNPs inside the cell, distributed in the cytosol; (e) phagocytosis of AgNPs. Arrows indicate the AgNPs. Scale bar for each figure is 500 nm.

5.2.2.3 Neurons preferentially phagocytose large AgNPs

Preferential uptake of large AgNPs into the cell cytoplasm might be explained with the internalization pathway. So far, five endocytosis pathways were discovered. They are kiss and run mechanism, clathrin-mediated endocytosis, phagocytosis, caveolae, and macropinocytosis. Kiss and run mechanism and clathrin-mediated endocytosis pathways take part in sustaining the vesicular neurotransmitter release and vesicle recycling in the synapse. Phagocytosis does not have a role in neurotransmitter turnover but it can internalize particles larger than 100 nm, which cannot be internalized by other mechanisms. We did not observe presence of nanoparticles in axon terminals in conditions where the synaptic vesicular turnover either was kept at the basal rate or was significantly increased by high K^+ treatment, which is known to stimulate the vesicular recycling in the synapses [228]. Rather, AgNPs were located inside the neuron soma. Our data revealed that the AgNP internalization process was via outward membrane projections in the soma region; implying that vesicular recycling pathways do not have a role in nanoparticle internalization, at least for this size set of pure uncoated AgNPs. We excluded clathrin-mediated endocytosis pathway as a major mechanism of AgNP cellular entry for the reasons listed below: Firstly, the size of the AgNP was greater than the average size of molecules can be handled by clathrin pathway which is around 200 nm [235]; secondly, we did not observe a characteristic dense area around the internalized AgNP as an indicator of clathrin coating; and lastly, we observed an extracellular elongation of the membrane as if it was engulfing the AgNP. The findings of this study suggest phagocytosis as the internalization mechanism for pure uncoated AgNPs rather than any other endocytosis pathways. This uptake mechanism is crucial for further toxicology studies since it may be a novel entry mechanism for nanoparticles that do not have altered surface chemistry or coating. There are studies about the uptake mechanisms of AgNPs into the cells, but to our knowledge, this is the first time that pure uncoated AgNPs produced by laser ablation is shown to be taken into neurons in the isolated hippocampus tissue. Our study proves that even a pure nanoparticle would facilitate the cellular uptake and it can be internalized and localized in the cell. These findings indicate the phagocytosis pathway might be

the cellular uptake mechanism for the pure AgNPs, rather than other endocytosis pathways.

5.2.2.4 AgNP treatment dose-dependently causes cell death

In order to evaluate the toxicity of pure uncoated AgNPs of different sizes we employed MTT cell viability assay. The MTT analysis showed a dose-dependent toxicity for AgNPs. 10, 15 and 20 mg/L AgNP administration did not cause any significant decrease in cell survival while 25 and 30 mg/L AgNP led to a statistically significant cell death ($p<0.0001$) when compared to the control group (Figure 5.5).

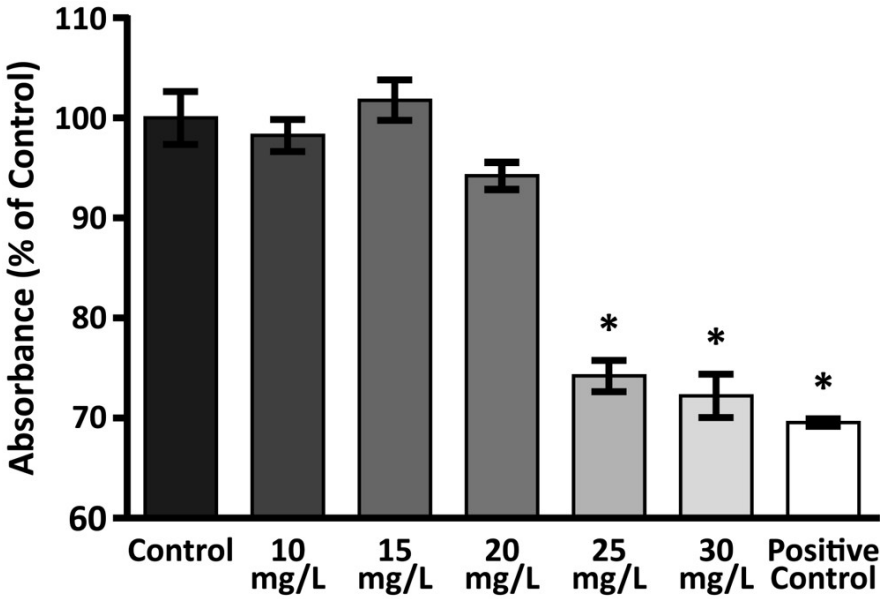

Figure 5.5: MTT cell viability assay results of hippocampal cells upon exposure to various AgNP concentrations for one hour. 10, 15 and 20 mg/L AgNP treatment did not cause a significant decrease in cell survival. One hour of 25 and 30 mg/L AgNP incubation resulted in cellular toxicity and cell death, which was found to be statistically significant ($p<0.0001$). Control group was incubated in physiological conditions while the positive control group did not receive oxygenation during incubation.

The dose selection for MTT cell viability assay was performed according to the literature. A wide range of AgNP doses were administered to cells *in vitro* in a

number of studies [221, 236, 237]. Accordingly, we wanted to determine the effects of the lowest possible dose which would not affect the hippocampal cells and the highest dose which would lead to death of cells as much as hypoxic conditions. The doses administered by Hussain et al. (2005) [221] to the rat liver cells were used as a reference and 10 mg/L was found to not affect the hippocampal cell survival. Moreover, 30 mg/L caused cell death comparable to the hypoxic positive group. Thus, to observe the dose-dependence of cell death upon AgNP administration, we performed cell viability analysis with five doses between 10 and 30 mg/L. Heavy metal toxicity is generally associated with cognitive and motor function disorders. Since hippocampus is a major brain region responsible for learning and memory and it is highly susceptible to cell death [238], we selected this region for our experiments. AgNP incubation decreased cell survival in a dose-dependent manner in rat hippocampal slices. Low doses of AgNP did not trigger any considerable decrease in cell survival while higher doses of AgNP resulted in a significant cell death compared to the controls. However, we did not perform a time-dependent assay to determine the toxicity of the lower doses in long-term periods, which might be considered as a limitation of the study. Therefore, lower doses of AgNPs might also be toxic for the neural tissue in long-term exposure. Our data are also consistent with a recent study which demonstrated that AgNP results in cellular toxicity in HT22 hippocampus cell line in a dose dependent manner [239]. The possible mechanism for AgNP toxicity seems to be related to an increase in the ROS levels that causes oxidative stress on the cells. Oxidative stress is seen when the anti-oxidant defense mechanism cannot compete with the increasing ROS levels [232]. A number of studies showed that the AgNPs cause lipid peroxidation in cell membrane, increased ROS levels and oxidative stress which result in DNA damage and apoptosis [240]. AgNPs were also shown to upregulate the oxidative stress-related genes in the caudate nucleus, frontal cortex and hippocampus regions of brain in mice [241]. Thus, it is crucial to determine the exact localization of AgNPs in the cells following exposure. While we did not evaluate the mechanism of AgNP-induced cellular toxicity, we speculate that the toxicity demonstrated with cell viability assay might be the result of ROS production in the hippocampal cells, leading to cell death on the basis of previous research.

5.2.3 Conclusion

In this study, we showed the distribution and the toxicity of the pure AgNPs produced by laser ablation method in the rat hippocampal slices. Moreover, we demonstrated that the cellular uptake mechanism of pure AgNPs depends on their sizes. Since we did not observe the presence of AgNPs in synaptic vesicles following stimulation of synaptic vesicular recycling, we concluded that phagocytosis is the type of endocytotic pathway that dominates the entry of pure AgNPs into the hippocampal neurons. Moreover, AgNP led to dose-dependent toxicity in hippocampal slices. Our data provide significant information for the further cellular and molecular research about the neurotoxicology of nanoparticles since exposure to silver nanoparticles might result in neurodegeneration. Furthermore, this study showed that laser ablation is a considerably useful method for studying nanoparticle toxicity since it provides pure nanoparticles mimicking the ones encountered in the industry.

5.3 Copper, Tin and Aluminum Nanoparticle Nanotoxicity on Human Neuroblastoma Cell Line SH-SY5Y

As described in chapter 3, CuNP is used in a number of fields but it also shows certain levels of cellular toxicity. The data represented in Chapter 3 and Chapter 4 shows that exposure to the nanoparticles via inhalation lead to the distribution and localization of these nanoparticles to different organs, including brain. Thus, it is also crucial to study the effects of these nanoparticles in *in vitro* conditions to reveal the cellular toxicity. In the literature, there are a number of studies analyzing the effects of different nanoparticles on various cell lines. However, to our knowledge, this is the first study in the literature demonstrating that CuNP, AlNP and SnNP, which were generated by pulsed laser ablation in liquids, result in cellular toxicity in human neuroblastoma SH-SY5Y cell line. Nanoparticles were

shown to induce ROS production in cells due to three different factors: (1) the surface reactivity and the functional groups on the nanoparticle surface, (2) active redox cycling on the surface of NP because of transition metal-based nanoparticles, (3) the interactions between the cell and the nanoparticles [242, 243]. In terms of the surface reactivity, when oxidant and free radical are bound onto the nanoparticle surface, free radicals are produced [244]. Moreover, due to the nanosize of the particles, structural defects and changes in the electronic properties are observed and this leads to the production of reactive groups on nanoparticle surface [245, 246]. The electron donor or acceptor active sites within the reactive sites on the nanoparticle surface gain access to interaction with molecular O_2 to form O_2^-, which would result in the further ROS production [247]. Furthermore, free radicals might be generated by binding onto nanoparticle surface or they might be produced freely in an aqueous suspension [248]. ROS production might be enhanced due to the release of metal ions after the nanoparticle dissolution [249]. On the other hand, metals and chemical compounds on the nanoparticle surface accelerate the ROS generation [250]. Copper was shown to induce oxidative stress through Fenton-type reaction, in which the copper ions as the transition metal ion reacts with H_2O_2 to obtain $OH^{\cdot}$ and oxidized metal ion [251]. Besides, when nanoparticles are taken into the cell and reach to mitochondria, they might trigger the ROS production by disrupting the electron transport chain, damage to the organelle structure, activation of NADPH-like enzyme system and mitochondrial membrane depolarization [252, 253]. Nanoparticle-induced oxidative stress in the cells were shown to eventually result in apoptosis [254, 255, 256]. There are a number of apoptotic pathways in the cell, but among them, metal and metal oxide nanoparticles lead to cell death via intrinsic mitochondrial apoptotic pathway [253]. The increased levels of ROS in mitochondria might lead to the membrane depolarization in mitochondria due to the disruption of membrane phospholipids [257]. Among a number of metal oxide nanoparticles, copper was demonstrated to induce apoptosis due to mitochondrial dysfunction mediated by ROS [258].

In this part of the study, CuNP, SnNP and AlNP, produced by the same material processing laser system described above, were exposed to SH-SY5Y human

neuroblastoma cell line to determine their cellular toxicity and to analyze the mRNA expression and protein level changes in NMDAR subunits.

5.3.1 Materials and Methods

5.3.1.1 Cell Culture

SH-SY5Y human neuroblastoma cell line was a gift from Prof. Dr. Vasıf Hasırcı at Middle East Technical University Center of Excellence in Biomaterials and Tissue Engineering. SH-SY5Y cells were cultured in polystyrene cell culture plates in Dulbeccos Modified Eagle Medium/Hams Nutrient Mixture F12 (DMEM/F12; 1:1) (Sigma-Aldrich, Germany) supplemented with 10% fetal bovin serum (FBS) (Biological Industries, USA) and 100 g/mL penicillin/streptomycin (Sigma-Aldrich, Germany). These plates were incubated at 37°C and 5% CO_2 and the medium was changed in two days. The cells adhered to the cell culture plate were incubated in 0.05% Trypsin-EDTA (Sigma-Aldrich, Germany) at 37°C for 5 minutes and collected by centrifugation at 2.500xg for 5 minutes.

5.3.1.2 Production of Copper, Tin and Aluminum Nanoparticles by Laser Ablation Method in Liquid

The same copper, tin and aluminum plates described in Chapter 2 were used as the target of a laser beam to produce the copper, tin and aluminum nanoparticles (CuNP, SnNP and AlNP, respectively) with laser ablation method as described in 5.2.1.2 in phosphate buffered saline (PBS) solution. Nanoparticles were produced by the nanosecond pulsed ND:YAG marking laser described in Chapter 2, Table 2.1. The laser ablation was carried out for 5 minutes by the beam scanning over the target surface, creating a solution with dispersed nanoparticles in the liquid medium. The targets for each nanoparticle production was weighed before and after the ablation process and the concentration of the nanoparticle solutions were determined as 115 ng/μl CuNP, 1000 ng/μl SnNP and 185 ng/μl AlNP.

The nanoparticle solutions were sterilized by exposing them to UV light for 1 hour. The structural and topographical properties of nanoparticles were analyzed using SEM (FEI Quanta 200 FEG, OR, USA). Further morphological analysis of nanoparticles were performed by using TEM (FEI Tecnai G2F30) as described previously.

5.3.1.3 Alamar Blue Assay for the Cellular Toxicity

For alamar blue assay, 40.000 SH-SY5Y cells/well were seeded in a 96 well plate and they were incubated overnight at 37°C and 5% CO_2. After the incubation, the cells were treated with nanoparticle solutions with different concentrations as PBS only (D0), 12.5 ng/μl (D1), 25 ng/μl (D2) and 50 ng/μl (D3) in a 50 μl volume. Besides these treatments, there were also positive control cells with no treatment and negative control wells containing only DMEM but not the cells. All groups were studied as n=6. Four different analysis points were determined as 0, 24, 48 and 72 hours after the treatment. For the analysis at different time points, the cell media were removed from the wells, 40 μl/well 10% alamar blue solution (for 10% alamar blue solution; 1 ml olf alamar blue (Invitrogen, USA) was mixed with 100 μl penicillin/streptomycin (Sigma-Aldrich, Germany) and 8.9 ml DMEM without phenol red (Merck Millipore, Germany)) was added to each well. After incubating at 37°C and 5% CO_2 for 1 hour, the absorbance values were determined with a spectrophotometric measurement at 570 nm and 595 nm wavelengths. The cellular toxicity was calculated by using the measured absorbance values and the equation:

$$\text{Decrease in the percentage} = \frac{[(\epsilon_{ox})_{\lambda 2} \times A_{\lambda 1}] - [(\epsilon_{ox})_{\lambda 1} \times A_{\lambda 2}]}{[(\epsilon_{red})_{\lambda 1} \times A'_{\lambda 2}] - [(\epsilon_{red})_{\lambda 2} \times A'_{\lambda 1}]} \times 100 \quad (5.1)$$

where;

$\lambda 1 = 570$ nm

$(\epsilon_{ox})_{\lambda 2} = 117.216$

$(\epsilon_{ox})_{\lambda 1} = 80.586$

$\lambda 2 = 595$ nm
$(\epsilon_{red})_{\lambda 1} = 155.677$
$(\epsilon_{red})_{\lambda 2} = 14.652$

The toxicity percentage was calculated by using the following equation:

$$\text{Toxicity percentage} = \frac{\text{Decrease in the percentage of sample}}{\text{Decrease percentage of the control}} \times 100 \qquad (5.2)$$

According to equation 5.2, the dose whose toxicity percentage was below 50% was accepted as the LD_{50} value (LD: Lethal Dose).

5.3.1.4 RNA Isolation from the Cells

For RNA isolation, SH-SY5Y cells were cultured in T25 cell culture flasks as 500.000 cells / T25 flask. They were incubated overnight at 37°C and 5% CO_2. The flasks were divided into four groups as vehicle group (only PBS), CuNP-treated, SnNP-treated and AlNP-treated groups (n=3). The LD_{50} dose calculated at 48^{th} hour as described in equation 5.2 was administered to each group. Accordingly, 15.03 ng/μl CuNP, 73.32 ng/μl SnNP and 29.77 ng/μl AlNP were administered to the cells. After the nanoparticle administration, the cells were incubated for 48 hours at 37°C and 5% CO_2. At the end of the 48 hour, RNA isolation was performed with Trizol method as described in Chapter 3. The only difference was the homogenization method. This time, Trizol reagent (Invitrogen, USA) was directly added onto the cells in T25 flasks after the removal of medium. The isolation protocol was same as in Chapter 3. The concentrations of the RNA samples were measured with NanoDrop (Thermo Scientific, USA).

5.3.1.5 cDNA Preparation

Primer Synthesis

The primer design and synthesis was performed by considering the NCBI gene accession numbers as described in chapter 3, primer synthesis section.

Table 5.1: The designed and synthesized primers to be used in cDNA Synthesis and qPCR (RP: reverse primer, FP: forward primer)

Gene name and NCBI accession number	Sequence	Tm values	Distilled water added for 100μM stock	Product Length
GAPDH (NM_001289745.1) FP	5'CAATGACCCCTTCATTGACC3'	53.6°C	1150.30 μl	95 bp
GAPDH (NM_001289745.1) RP	5'TTGATTTTGGAGGGATCTCG3'	52.2°C	988.50 μl	
NMDAR1 (NM_007327.3) FP	5'CGTGAGTCCAAGGCAGAGAA3'	54°C	1016.80 μl	80 bp
NMDAR1 (NM_007327.3) RP	5'TCTTTCGCCTCCATCAGCAG3'	54°C	1193.70 μl	
NMDAR2a (NM_001134407.2) FP	5' CATGCGGGAACCCGCTAAA3'	53°C	972.10 μl	110 bp
NMDAR2a (NM_001134407.2) RP	5' CCACTGACGGTCCCTGTAG3'	55°C	1124.50 μl	

cDNA Synthesis

cDNA synthesis was performed with the same protocol described in chapter 3, cDNA synthesis section.

5.3.2 Quantitative Real Time Polymerase Chain Reaction (qRT-PCR)

qRT-PCR was performed as described in subsection 3.2.6 and the reaction conditions were applied as shown in Table 3.3 and Table 3.4. The relative quantification was also performed as described in Equation 3.1.

5.3.3 Protein Isolation from SH-SY5Y Cell Line

For protein isolation, SH-SY5Y cells were cultured in T75 cell culture flasks as 5×10^6 cells / T75 flask. They were incubated overnight at 37°C and 5% CO_2. The flasks were divided into four groups as vehicle group (only PBS), CuNP treated, SnNP treated and AlNP treated groups (n=3). The LD_{50} dose calculated at 48^{th} hour as described in equation 5.2 was administered to each group. Accordingly, 15.03 ng/μl CuNP, 73.32 ng/μl SnNP and 29.77 ng/μl AlNP were administered

to the cells. After the nanoparticle administration, the cells were incubated for 48 hours at 37°C and 5% CO_2.

The same commercially available protein isolation kit was used for the isolation of proteins from SH-SY5Y cells but this time the isolation protocol for the cells was performed according to the manufacturer's procedure (Thermo Scientific, USA). Before the isolation procedure, a commercially available protease and phospatase inhibitor (Sigma Aldrich, Germany) was added to the permeabilization and solubilization buffers. The cells were detached from the cell culture flasks by 0.05% Trypsin-EDTA (Sigma-Aldrich, Germany) treatment and incubating at 37°C for 5 minutes. The cells were centrifuged at 2.500xg for 5 minutes. The pellet was resuspended in 3 ml of cell wash solution and centrifuged at 2.500xg for 5 minutes, again. The supernatant was carefully removed and the cells were resuspended in 1.5 ml cell wash solution. After the centrifugation at 2.500xg for 5 minutes, the pellet was resuspended in 0.75 ml of permeabilization buffer. The solution was vortexed and incubated 30 minutes on ice with constant mixing. After the incubation, the solution was centrifuged at 16.000 x g for 15 minutes at 4°C to pellet the permeabilized cells. The supernatant, containing the cystosolic protein fraction, was transferred to a new microcentrifuge tube. Then, the pellet was dissolved in 0.5 mL of solubilization buffer and incubated for 30 minutes on ice with constant mixing. After the incubation, the solution was, again, centrifuged at 16.000 x g for 15 minutes at 4°C. At the end of the centrifugation process, the supernatant was containing membrane and membrane-associated proteins. The pellet was discarded. Both cytosolic and membrane-associated proteins were stored at -20°C in aliquots until the western blot analyses.

Protein concentrations were determined as described in 3.2.8.

The SDS-PAGE and western blot analyses were performed as described in 3.2.9 and 3.2.10.

5.3.3.1 Statistical Analysis

All the data are represented as mean ± SEM. For the mRNA expression and protein level analyses unpaired, two-tailed Student's t test was used. $p<0.05$ was considered as statistically significant.

5.3.4 Results and Discussion

5.3.4.1 Characterization of CuNP, SnNP and AlNP

The SEM image of the nanoparticles showed that spherically shaped CuNP, SnNP and AlNP were produced with laser ablation successfully (Figure 5.6). For the further analysis, TEM images were obtained and it was demonstrated that the most of the nanoparticles are smaller than 100 nm although there are larger nanoparticles as shown in SEM images. TEM images also represent that there is no aggregation of the nanoparticles. Thus, before administration to the cells, the nanoparticles did not aggregate. Furthermore, TEM images showed that the nanoparticles had crystal structure.

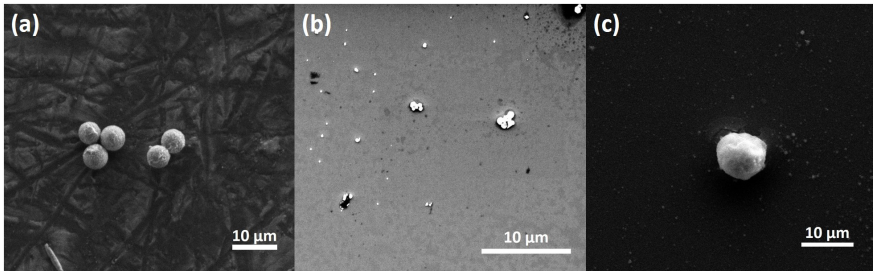

Figure 5.6: TEM images of (a) CuNP, (b) SnNP and (c) AlNP produced in PBS.

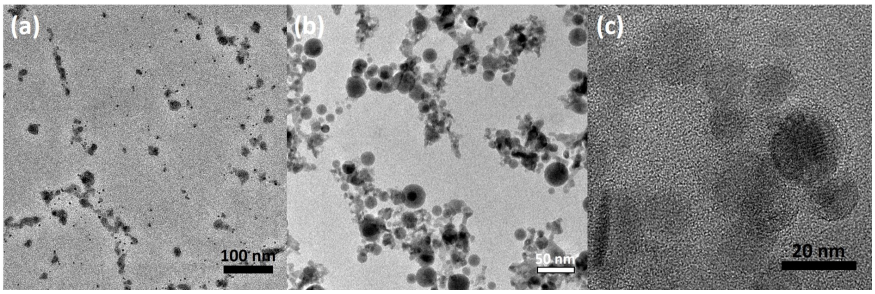

Figure 5.7: TEM images of (a) CuNP, (b) SnNP and (c) AlNP produced in PBS. All the nanoparticles were spherical in shape, crystalline in structure and most of the nanoparticles are smaller than 100 nm.

5.3.4.2 CuNP, SnNP and AlNP lead to cell death in a dose-dependent manner

Alamar blue analysis performed after the 48^{th} hour of the nanoparticle administration revealed that all nanoparticles resulted in a dose-dependent toxicity (Figure 5.8). At 12.5 ng/μl, CuNP resulted in the death of approximately 43% of the cells ($^{*}p<0.5$). At the same dose, SnNP and AlNP killed 22% and 41% of the cells ($^{*}p<0.5$ for AlNP group). At 25 and 50 ng/μl doses, CuNP killed all of the cells. SnNP resulted in the death of 33% and 61% of the cells at 25 and 50 ng/μl doses, respectively. AlNP, on the other hand, led to the death of 45% and 63% of the cells at 25 and 50 ng/μl doses, respectively.

As shown in figure 5.8, CuNP, SnNP and AlNP led to a dose-dependent toxicity in SH-SY5Y cells 48 hours after the administration of nanoparticles. Among them, CuNP was found as the most toxic one since all of the cells were dead with 25.0 and 50.0 ng/μ concentration. SnNP and AlNP were shown to increase their cytotoxic effect with increasing nanoparticle doses and this toxicity was shown due to the ROS increase in the cell [259]. Kim et al. showed that CuNP produced by laser ablation method has the lowest toxicity on PC3 and MCF7 cell lines among AgNP, AuNP and CoNP. They suggested that since copper is used as a cofactor and biocatalyst, it is less toxic than the other three nanoparticles [260]. Prabhu et al. (2010) studied the effects of CuNP on rat dorsal root ganglion by exposing these neurons to CuNP in increasing nanoparticle concentrations (10100

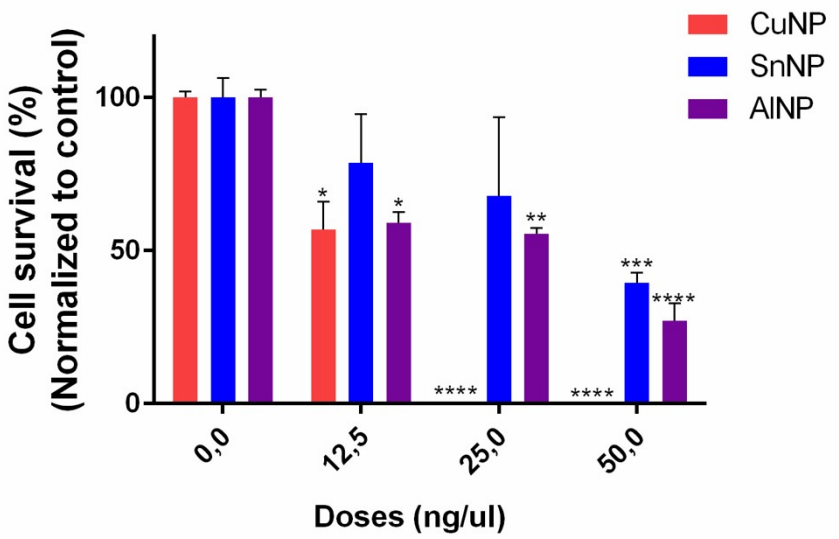

Figure 5.8: Alamar blue cellular toxicity results at 48th hour after administration of nanoparticles. CuNP, SnNP and AlNP displayed dose dependent toxicity on SH-SY5Y cells. $^{*}p<0.5$, $^{**}p<0.01$, $^{***}p<0.05$, $^{****}p<0.001$.

M) and sizes (40, 60, and 80 nm) for 24 h. It was demonstrated that all sized of CuNP led to significant toxic effects. Furthermore, they also reported that small-sized nanoparticles and higher concentration exerted the maximum toxic effects [261]. CuNP treatment to PC12 neuron cell line led to a decrease in cell survival in both dose- and time-dependent manner and this toxicity was suggested as due to the elevated reactive oxygen species (ROS) and oxidative stress [262]. It was shown that CuO nanoparticles triggered autophagy in MCF-7 breast cancer cell line in dose and time dependent manner [263]. Moreover, CuO nanoparticles were shown to cause cytotoxicity in HepG2 cells with increasing doses and they suggested that this was the result of upregulation of tumor suppressor gene p53 and the gene encoding apoptotic enzyme caspase-3 due to CuO administration [264]. Besides copper, a number of studies revealed that the nanoparticle toxicity is due to increase ROS in cells, resulting in disruption of metabolic pathways via oxidative stress [97]. AlNP was shown as cytotoxic in a number of studies. Lin et al. (2008) demonstrated that Al_2O_3 nanoparticles led to a dose and time dependent cytotoxicty, which might be suggested due to the membrane depolarization of A549 cell line, which are human bronchoalveolar carcinoma-derived cells

[146]. Furthermore, Al_2O_3 NP significantly decreased the phagocytosis ability of rat alveolar macrophages [145]. Moreover, aluminum oxide nanoparticles were shown to induce mitochondria-mediated oxidative stress leading to cytotoxicity in human mesenchymal stem cells [265]. As mentioned in Chapter 3, although there are a number of application fields in which SnNP is used, there are not much studies related to its cellular toxicity. In this study, the dose-dependent toxicity of CuNP, SnNP and AlNP might be due the ROS production and oxidative stress in the neuron cells, which ultimately led to the activation of apoptotic patways and cell death.

5.3.4.3 CuNP, SnNP and AlNP lead to changes in NMDAR1 and NMDAR2a mRNA expression levels and NMDAR1 protein level

RNA isolation was performed from concentrations of isolated RNA from SH-SY5Y cells and their concentrations and ratios of A_{260}/A_{280} and A_{260}/A_{230} were determined. The results are represented in the appendix table C2. RNA concentrations were indicated in ng/μl and it was revealed that the concentrations were acceptable to be used in cDNA synthesis and qRT-PCR experiments. Moreover, the A_{260}/A_{280} values between 1.80 - 2.00 suggest that RNA is pure and free from any DNA contamination.

The expression changes in NMDAR1 and NMDAR2a were detected (Figure 5.9). Accordingly, CuNP, SnNP and AlNP resulted in an increase in the NMDAR1 subunit expression as 3.595 $\pm$ 0.174, 2.146 $\pm$ 1.136 and 1.413 $\pm$ 1.006, respectively. On the other hand, NMDAR2a subunit expression increased by 1.280 $\pm$ 0.292 fold with CuNP treatment but decreased 0.535 $\pm$ 0.062 fold with SnNP and there was no expression with AlNP treatment.

Concentrations of isolated proteins from the SH-SY5Y cells were determined and represented in appendix table C3.

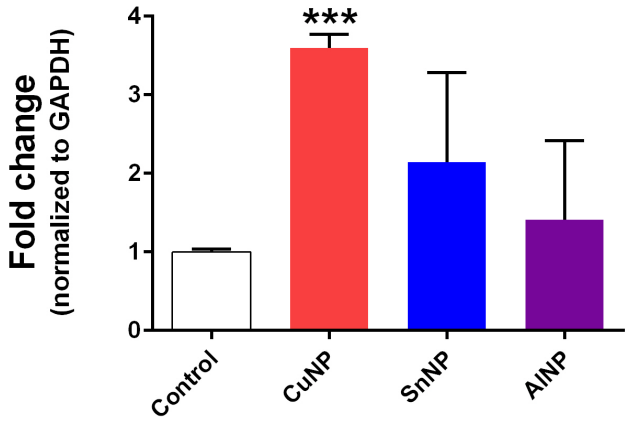

Figure 5.9: NMDAR1 mRNA expression change with CuNP, SnNP and AlNP administration to SH-SY5Y cells detected with qRT-PCR. CuNP, SnNP and AlNP resulted in an increase in the NMDAR1 subunit expression as 3.595 ± 0.174, 2.146 ± 1.136 and 1.413 ± 1.006, respectively (n=3).

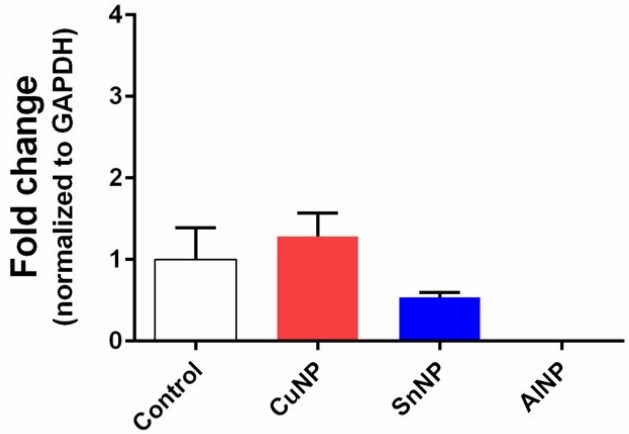

Figure 5.10: NMDAR2a subunit expression increased by 1.280 ± 0.292 fold with CuNP treatment but decreased 0.535 ± 0.062 fold with SnNP and there was no expression with AlNP treatment (n=3).

The changes in NMDAR1 protein levels with CuNP, SnNP and AlNP administration to SH-SY5Y cells were determined with western blot analysis (Figure 5.11). CuNP resulted in a 90% decrease in the NMDAR1 protein levels ($^{**}p<0.01$). On the other hand, SnNP led to a 0.67 fold decrease in the protein expression ($^{*}p<0.05$). Although AlNP administration increased the NMDAR1 protein level 1.34 fold, the change did not reach to statistical significance.

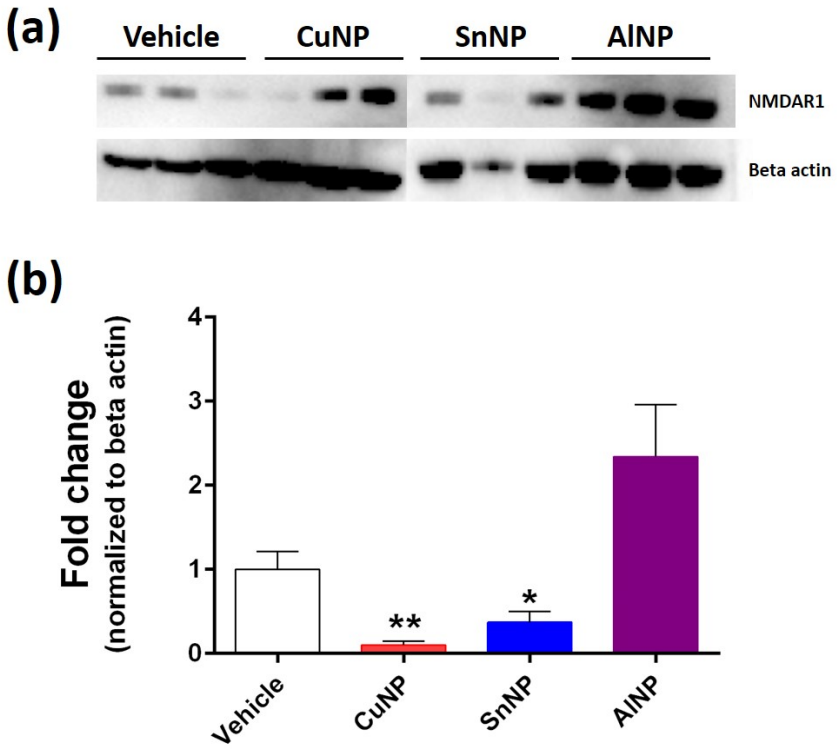

Figure 5.11: Change in NMDAR1 protein levels with CuNP, SnNP and AlNP administration to SH-SY5Y cells. CuNP resulted in a decreased NMDAR1 protein levels to 0.10 ± 0.04 ($^{**}p<0.01$). SnNP led to a decrease up to 0.37 ± 0.13 in the protein amounts ($^{*}p<0.05$). Although AlNP administration increased the NMDAR1 protein level 1.34 fold, the change did not reach to statistical significance.

Besides the cytotoxic effects of CuNP, SnNP and AlNP on SH-SY5Y cell line, these nanoparticles also altered the mRNA expression of NMDAR1 and NMDAR2a subunits, together with an alteration in NMDAR1 protein levels. Among three nanoparticles, CuNP led to a statistically significant increase in NMDAR1 subunit while SnNP and AlNP did not alter the expression significantly although

SnNP resulted in an increased expression tendency. However, NMDAR2a did not change significantly after the nanoparticle exposures. CuNP was also shown as the most toxic nanoparticle among them on SH-SY5Y cell line in the alamar blue cytotoxicity assay. On the other hand, CuNP and SnNP led to statistically significant decrease in NMDAR protein levels. Being a divalent cation receptor [178, 179], NMDAR was shown to be significantly affected by the CuNP and SnNP. Moreover, the signficantly increased mRNA levels upon CuNP and tendency to increase after SnNP exposure might be the compensation mechanism of significantly decreased protein levels. On the other hand, these nanoparticles might be affecting the translational pathway of NMDAR protein, thus increased mRNA expression could not be reflected to the protein levels. Since these nanoparticles also resulted in the ROS production and cellular toxicity in a dose dependent manner, the effect of ROS on the NMDAR expression should also be considered. It was demonstrated that NMDAR1 mRNA expression increased significantly after hydrogen peroxide administration [266], which is consistent with our data. Moreover, it was shown in the literature that when NMDAR is excessively activated, ROS production is observed, leading to activation of apoptotic cascade [267]. Thus, in an increased ROS environment in the cell, decreased NMDAR protein levels in CuNP- and SnNP-exposed cells might be a feedback mechanism not to further increase the ROS due to nanoparticles. Furthermore, NMDAR2b subunit was not detected in this study in terms of the gene expression and protein levels. However, NMDAR2b gene expression and protein levels might also be altered. Since the functional NMDAR consists of NMDAR1 and NMDAR2a or NMDAR2b subunits, NMDAR1 protein levels in the membrane might be determined with the levels of NMDAR2a and NMDAR2b subunits. There are some differences between the NMDAR subunit expression and protein levels in *in vivo* studies described in Chapter 3 and the results obtained in these *in vitro* studies. These differences might be explained by a number of factors. Firstly, the exposed doses are quite different between these two studies. While in the *in vivo* study, a real time exposure setup was designed and used to expose rats, in the *in vitro* study nanoparticles were directly added into the medium. In the *in vivo* study, the exposed nanoparticles were distributed to body into different organs in different doses. However, in *in vitro* study, cells were in the direct

contact with the nanoparticles. Therefore, the dose might be a significant factor for different NMDAR subunit expression and protein levels in *in vivo* and *in vitro* studies. Secondly, in the *in vivo* study an intact central nervous system was in action. In other words, the microglials cells and the synaptic connections should also be considered while evaluating the results. However, in *in vitro* conditions only neuron cells are exposed to nanoparticles and there are no synapses in cell culture conditions. Thirdly, the cell lines are always cancer cells and SH-SHY5Y cells are human bone marrow neuroblastoma cells. The same study might be conducted with a hippocampal primary cell culture or hippocampal cell line such as HT22, which is an immortalized mouse hippocampus cell line.

5.4 Conclusion

This chapter described two different studies analyzing the toxic effects of different nanoparticles in *in vitro* conditions. In the first study, we demonstrated the distribution and the toxicity of the pure AgNPs produced by laser ablation method in the rat hippocampal slices. We also showed that the cellular uptake mechanism of pure AgNPs depends on their sizes. It was also revealed that phagocytosis is the type of endocytotic pathway that dominates the entry of pure AgNPs into the hippocampal neurons. Furthermore, AgNP led to dose-dependent toxicity in hippocampal slices. On the other hand, CuNP, SnNP and AlNP, which were produced by pulsed laser ablation method were administered to a dose-dependent cytotoxicity in human neuroblastoma cell line SH-SY5Y. Moreover, it was shown that NMDAR subunits NMDAR1 and NMDAR2a mRNA expressions and NMDAR1 protein levels were altered after CuNP, SnNP and AlNP administration.

Chapter 6

Conclusion

This thesis study showed the successful nanoparticle production by pulsed laser ablation method and the toxic effects of these nanoparticles both in *in vivo* and *in vitro* conditions.

It was revealed that pulsed laser ablation is a quite convenient method for the production of a number of different nanoparticles both in liquids and gas environment. Moreover, the starting material might change from bulk solid target to powder target.

Ultra-small InN-NCs (<5 nm in diameter) could be produced from InN powder target by using PLAL technique. It was shown that lower laser energy and lower ablation duration result in much smaller nanoparticles since even if the ablation time increased and the smaller nanoparticles were produced, they tended to aggregate. Hexagonal InN-NCs smaller than 5 nm in diameter were produced in ethanol with optimized ablation conditions successfully. We showed that PLAL is a suitable technique for production of InN-NCs, which is a Group III nitride. Thus, other nitrides in the same group might be successfully produced with this technique. As an outlook of InN-NC production with PLAL method, ablation with femtosecond laser pulses might be studied to overcome the low decomposition temperature disadvantage of InN material. This study was accepted for

publication in Applied Physics A and it is in the publication process.

It was demonstrated that CuNP, SnNP and AlNP were successfully produced in the environment during the marking of respective metal plates. This data indicate that laser material processing in the industry constitutes high risk for the workers since they expose to the nanoparticles without any protective material.

For the first time in the literature, the real time nanoparticle exposure setup was developed to mimic the industrial environment for the determination effects of nanoparticles on the rats' learning and memory process. Both behavioral tests and *in vivo* electrophysiology experiments revealed that 3 months of copper, tin and aluminum nanoparticles exposure did not lead to any alterations in the learning and memory process of the rats. However, AlNP led to a decrease in the anxiety like behavior of the rats exposed to these nanoparticles. Thus, it can be concluded that AlNP resulted in a mood change in these animals. Moreover, it was demonstrated that NMDAR subunits NMDAR1 and NMDAR2a mRNA expressions were significantly increased in SnNP and AlNP exposed groups. Moreover, NMDAR1 protein levels were shown to decrease after CuNP and SnNP exposure compared to controls. It might be concluded that CuNP, SnNP and AlNP produced during laser materials processing might lead to changes in mRNA and protein levels of NMDAR after three months of exposure. Although this change was not reflected to the synaptic transmission and behavior, in long term exposure there is a high risk to alter the learning and memory functions, together with neurodegeneration.

Cu, Sn and Al were detected in a number of organs throughout the body upon inhalation. The lack of these elements in the intestine demonstrates that the major route of entry was through inhalation. Although we cannot completely rule out the oral route, it seems to be a very minor path of entry for NPs. Lungs, the primary target organs after the inhalation, were detected with the high element concentrations indicating the accumulation of these nanoparticles in the lungs. The nanoparticles also reached to a number of organs through systemic circulation, such as heart, liver, kidney, spleen, and testis. Moreover, nanoparticles were shown to reach a number of brain parts either by passing

through the BBB or via olfactory bulb. The body distribution results indicate that nanoparticles produced during laser materials processing might lead to a number of health risks in human upon inhalation.

As an outlook, a setup which will remove the produced nanoparticles from the environment might be developed so that the risk of the nanoparticle inhalation would be reduced. Our group also designed such a system in which the nanoparticles will be taken out of the laser material processing area and will be trapped in the water. By this way, these nanoparticles will not be distributed to the atmosphere. This system will be analyzed in terms of nanoparticle capture capacity with water and with different solvents containing surfactants in it. Thus, a solution for this important problem in the industry might be developed.

The distribution and the toxicity of the pure AgNPs produced by laser ablation method was demonstrated in the rat hippocampal slices. Moreover, the cellular uptake mechanism of pure AgNPs were shown to depend on their sizes. Since no AgNPs were detected in synaptic vesicles following stimulation of synaptic vesicular recycling, it was concluded that phagocytosis is the type of endocytotic pathway that dominates the entry of pure AgNPs into the hippocampal neurons. Moreover, AgNP led to dose-dependent toxicity in hippocampal slices. The data provide significant information for the further cellular and molecular research about the neurotoxicology of nanoparticles since exposure to silver nanoparticles might result in neurodegeneration. Furthermore, this study showed that laser ablation is a considerably useful method for studying nanoparticle toxicity since it provides pure nanoparticles mimicking the ones encountered in the industry. This study was accepted to Toxicology and Industrial Health and it is in the publication proces.

CuNP, SnNP and AlNP exposure led to a dose-dependent cytotoxicity in human neuroblastoma cell line SH-SY5Y. Moreover, it was shown that NMDAR subunits NMDAR1 and NMDAR2a mRNA expressions and NMDAR1 protein levels were altered after CuNP, SnNP and AlNP administration.

Bibliography

[1] M. Lynch, "Long-term potentiation and memory," *Physiological reviews*, vol. 84, no. 1, pp. 87–136, 2004.

[2] S. Alkis, M. Alevli, S. Burzhuev, H. A. Vural, A. K. Okyay, and B. Ortaç, "Generation of inn nanocrystals in organic solution through laser ablation of high pressure chemical vapor deposition-grown inn thin film," *Journal of Nanoparticle Research*, vol. 14, no. 8, pp. 1–6, 2012.

[3] T. Oztas, H. S. Sen, E. Durgun, and B. Ortac, "Synthesis of colloidal 2d/3d mos2 nanostructures by pulsed laser ablation in an organic liquid environment," *The Journal of Physical Chemistry C*, vol. 118, no. 51, pp. 30120–30126, 2014.

[4] S. Hu, Y. Dong, J. Yang, J. Liu, and S. Cao, "Simultaneous synthesis of luminescent carbon nanoparticles and carbon nanocages by laser ablation of carbon black suspension and their optical limiting properties," *Journal of Materials Chemistry*, vol. 22, no. 5, pp. 1957–1961, 2012.

[5] F. Lin, J. Yang, S.-H. Lu, K.-Y. Niu, Y. Liu, J. Sun, and X.-W. Du, "Laser synthesis of gold/oxide nanocomposites," *Journal of Materials Chemistry*, vol. 20, no. 6, pp. 1103–1106, 2010.

[6] S. Hu, Y. Guo, Y. Dong, J. Yang, J. Liu, and S. Cao, "Understanding the effects of the structures on the energy gaps in carbon nanoparticles from laser synthesis," *Journal of Materials Chemistry*, vol. 22, no. 24, pp. 12053–12057, 2012.

[7] A. Hahn, S. Barcikowski, and B. N. Chichkov, "Influences on nanoparticle production during pulsed laser ablation," *Pulse*, vol. 40, no. 45, p. 50, 2008.

[8] H. S. Sharma and A. Sharma, "Nanoparticles aggravate heat stress induced cognitive deficits, blood–brain barrier disruption, edema formation and brain pathology," *Progress in brain research*, vol. 162, pp. 245–273, 2007.

[9] P. K. Jain, X. Huang, I. H. El-Sayed, and M. A. El-Sayed, "Review of some interesting surface plasmon resonance-enhanced properties of noble metal nanoparticles and their applications to biosystems," *Plasmonics*, vol. 2, no. 3, pp. 107–118, 2007.

[10] G. Oberdörster, E. Oberdörster, and J. Oberdörster, "Nanotoxicology: an emerging discipline evolving from studies of ultrafine particles," *Environmental health perspectives*, pp. 823–839, 2005.

[11] A. E. Deniz, H. A. Vural, B. Ortaç, and T. Uyar, "Gold nanoparticle/polymer nanofibrous composites by laser ablation and electrospinning," *Materials Letters*, vol. 65, no. 19, pp. 2941–2943, 2011.

[12] G. Yang, "Laser ablation in liquids: applications in the synthesis of nanocrystals," *Progress in Materials Science*, vol. 52, no. 4, pp. 648–698, 2007.

[13] G.-W. Yang, J.-B. Wang, and Q.-X. Liu, "Preparation of nano-crystalline diamonds using pulsed laser induced reactive quenching," *Journal of Physics: Condensed Matter*, vol. 10, no. 35, p. 7923, 1998.

[14] N. O. San, C. Kurşungöz, Y. Tümtaş, Ö. Yaşa, B. Ortaç, and T. Tekinay, "Novel one-step synthesis of silica nanoparticles from sugarbeet bagasse by laser ablation and their effects on the growth of freshwater algae culture," *Particuology*, vol. 17, pp. 29–35, 2014.

[15] E. Üçüncü, A. D. Özkan, C. Kurşungöz, Z. E. Ülger, T. T. Ölmez, T. Tekinay, B. Ortaç, and E. Tunca, "Effects of laser ablated silver nanoparticles on lemna minor," *Chemosphere*, vol. 108, pp. 251–257, 2014.

[16] A. Demirel, T. Öztaş, C. Kurşungöz, İ. Yılmaz, and B. Ortaç, "Synthesis of blue-shifted luminescent colloidal gan nanocrystals through femtosecond pulsed laser ablation in organic solution," *Journal of Nanoparticle Research*, vol. 18, no. 5, pp. 1–10, 2016.

[17] B. Monemar, "Iii-v nitridesimportant future electronic materials," *Journal of Materials Science: Materials in Electronics*, vol. 10, no. 4, pp. 227–254, 1999.

[18] A. G. Bhuiyan, A. Hashimoto, and A. Yamamoto, "Indium nitride (inn): A review on growth, characterization, and properties," *Journal of Applied Physics*, vol. 94, no. 5, pp. 2779–2808, 2003.

[19] I. Mahboob, T. Veal, C. McConville, H. Lu, and W. Schaff, "Intrinsic electron accumulation at clean inn surfaces," *Physical review letters*, vol. 92, no. 3, p. 036804, 2004.

[20] S. K. OLeary, B. E. Foutz, M. S. Shur, and L. F. Eastman, "Potential performance of indium-nitride-based devices," *Applied physics letters*, vol. 88, no. 15, p. 152113, 2006.

[21] X. Michalet, F. Pinaud, L. Bentolila, J. Tsay, S. Doose, J. Li, G. Sundaresan, A. Wu, S. Gambhir, and S. Weiss, "Quantum dots for live cells, in vivo imaging, and diagnostics," *science*, vol. 307, no. 5709, pp. 538–544, 2005.

[22] M.-S. Hu, W.-M. Wang, T. T. Chen, L.-S. Hong, C.-W. Chen, C.-C. Chen, Y.-F. Chen, K.-H. Chen, and L.-C. Chen, "Sharp infrared emission from single-crystalline indium nitride nanobelts prepared using guided-stream thermal chemical vapor deposition," *Advanced Functional Materials*, vol. 16, no. 4, pp. 537–541, 2006.

[23] O. Briot, B. Maleyre, and S. Ruffenach, "Indium nitride quantum dots grown by metalorganic vapor phase epitaxy," *Applied physics letters*, vol. 83, no. 14, pp. 2919–2921, 2003.

[24] N. Nepal, N. A. Mahadik, L. O. Nyakiti, S. B. Qadri, M. J. Mehl, J. K. Hite, and C. R. Eddy Jr, "Epitaxial growth of cubic and hexagonal inn thin

films via plasma-assisted atomic layer epitaxy," *Crystal Growth & Design*, vol. 13, no. 4, pp. 1485–1490, 2013.

[25] A. Lima, A. Tabata, J. Leite, S. Kaiser, D. Schikora, B. Schöttker, T. Frey, D. As, and K. Lischka, "Growth of cubic inn on inas (001) by plasma-assisted molecular beam epitaxy," *Journal of crystal growth*, vol. 201, pp. 396–398, 1999.

[26] J. C. Hsieh, D. S. Yun, E. Hu, and A. M. Belcher, "Ambient pressure, low-temperature synthesis and characterization of colloidal inn nanocrystals," *Journal of materials chemistry*, vol. 20, no. 8, pp. 1435–1437, 2010.

[27] A. K. Mann, D. Varandani, B. R. Mehta, L. K. Malhotra, G. Mangamma, and A. Tyagi, "Formation of inn nanoparticle and nanorod structures by nitrogen plasma annealing method," *Bulletin of Materials Science*, vol. 31, no. 3, pp. 233–240, 2008.

[28] J. Xiao, Y. Xie, R. Tang, and W. Luo, "Benzene thermal conversion to nanocrystalline indium nitride from sulfide at low temperature," *Inorganic chemistry*, vol. 42, no. 1, pp. 107–111, 2003.

[29] M. Qaeed, K. Ibrahim, K. Saron, and A. Salhin, "Optical and structural properties of indium nitride nanoparticles synthesized by chemical method at low temperature," *Solar Energy*, vol. 97, pp. 614–619, 2013.

[30] P. Šimek, D. Sedmidubskỳ, K. Klímová, Š. Huber, P. Brázda, M. Mikulics, O. Jankovskỳ, and Z. Sofer, "Synthesis of inn nanoparticles by rapid thermal ammonolysis," *Journal of nanoparticle research*, vol. 16, no. 12, p. 2805, 2014.

[31] K. Sardar, F. Deepak, A. Govindaraj, M. Seikh, and C. Rao, "Inn nanocrystals, nanowires, and nanotubes," *Small*, vol. 1, no. 1, pp. 91–94, 2005.

[32] C. Wu, T. Li, L. Lei, S. Hu, Y. Liu, and Y. Xie, "Indium nitride from indium iodide at low temperatures: synthesis and their optical properties," *New journal of chemistry*, vol. 29, no. 12, pp. 1610–1615, 2005.

[33] X. Zhu, T. Suzuki, T. Nakayama, H. Suematsu, W. Jiang, and K. Niihara, "Underwater laser ablation approach to fabricating monodisperse metallic nanoparticles," *Chemical physics letters*, vol. 427, no. 1, pp. 127–131, 2006.

[34] A. K. Ali, *Preparation of Ag and Au Nanoparticles by Pulsed Laser Ablation in Liquids*. PhD thesis, Baghdad University, 1 2010.

[35] M. C. Roco, "Environmentally responsible development of nanotechnology," *Environmental science & technology*, vol. 39, no. 5, pp. 106A–112A, 2005.

[36] S. Alkis, M. Alevli, S. Burzhuev, H. A. Vural, A. K. Okyay, and B. Ortaç, "Generation of inn nanocrystals in organic solution through laser ablation of high pressure chemical vapor deposition-grown inn thin film," *Journal of Nanoparticle Research*, vol. 14, no. 8, p. 1048, 2012.

[37] B. Tekcan, S. Alkis, M. Alevli, N. Dietz, B. Ortac, N. Biyikli, and A. K. Okyay, "A near-infrared range photodetector based on indium nitride nanocrystals obtained through laser ablation," *IEEE Electron Device Letters*, vol. 35, no. 9, pp. 936–938, 2014.

[38] N. El-Atab, F. Cimen, S. Alkis, B. Ortaç, M. Alevli, N. Dietz, A. K. Okyay, and A. Nayfeh, "Enhanced memory effect via quantum confinement in 16 nm inn nanoparticles embedded in zno charge trapping layer," *Applied Physics Letters*, vol. 104, no. 25, p. 253106, 2014.

[39] D. Kim and D. Jang, "Synthesis of nanoparticles and suspensions by pulsed laser ablation of microparticles in liquid," *Applied surface science*, vol. 253, no. 19, pp. 8045–8049, 2007.

[40] H. Zeng, X.-W. Du, S. C. Singh, S. A. Kulinich, S. Yang, J. He, and W. Cai, "Nanomaterials via laser ablation/irradiation in liquid: a review," *Advanced Functional Materials*, vol. 22, no. 7, pp. 1333–1353, 2012.

[41] V. Amendola and M. Meneghetti, "Laser ablation synthesis in solution and size manipulation of noble metal nanoparticles," *Physical chemistry chemical physics*, vol. 11, no. 20, pp. 3805–3821, 2009.

[42] R. Tilaki, A. Iraji Zad, and S. Mahdavi, "Stability, size and optical properties of silver nanoparticles prepared by laser ablation in different carrier media," *Applied Physics A: Materials Science & Processing*, vol. 84, no. 1, pp. 215–219, 2006.

[43] A. Hahn, S. Barcikowski, and B. N. Chichkov, "Influences on nanoparticle production during pulsed laser ablation," *Pulse*, vol. 40, no. 45, p. 50, 2008.

[44] A. Schwenke, P. Wagener, S. Nolte, and S. Barcikowski, "Influence of processing time on nanoparticle generation during picosecond-pulsed fundamental and second harmonic laser ablation of metals in tetrahydrofuran," *Applied Physics A: Materials Science & Processing*, vol. 104, no. 1, pp. 77–82, 2011.

[45] H. Zhang, R. L. Penn, R. J. Hamers, and J. F. Banfield, "Enhanced adsorption of molecules on surfaces of nanocrystalline particles," *The Journal of Physical Chemistry B*, vol. 103, no. 22, pp. 4656–4662, 1999.

[46] F. Mafuné, J.-y. Kohno, Y. Takeda, T. Kondow, and H. Sawabe, "Formation and size control of silver nanoparticles by laser ablation in aqueous solution," *The Journal of Physical Chemistry B*, vol. 104, no. 39, pp. 9111–9117, 2000.

[47] F. Mafuné, J.-y. Kohno, Y. Takeda, T. Kondow, and H. Sawabe, "Formation of gold nanoparticles by laser ablation in aqueous solution of surfactant," *The Journal of Physical Chemistry B*, vol. 105, no. 22, pp. 5114–5120, 2001.

[48] M. Lei, K. Huang, R. Zhang, H. Yang, X. Fu, Y. Wang, and W. Tang, "Catalyst-free chemical vapor deposition route to inn nanowires and their cathodoluminescence properties," *Journal of Alloys and Compounds*, vol. 535, pp. 50–52, 2012.

[49] S. Barcikowski, A. Hahn, A. Kabashin, and B. Chichkov, "Properties of nanoparticles generated during femtosecond laser machining in air and water," *Applied Physics A*, vol. 87, no. 1, pp. 47–55, 2007.

[50] L. R. Squire, "Memory and the hippocampus: a synthesis from findings with rats, monkeys, and humans.," *Psychological review*, vol. 99, no. 2, p. 195, 1992.

[51] W. B. Scoville and B. Milner, "Loss of recent memory after bilateral hippocampal lesions," *Journal of Neurology, Neurosurgery & Psychiatry*, vol. 20, no. 1, pp. 11–21, 1957.

[52] J. P. Aggleton and M. W. Brown, "Episodic memory, amnesia, and the hippocampal–anterior thalamic axis," *Behavioral and brain sciences*, vol. 22, no. 03, pp. 425–444, 1999.

[53] H. Eichenbaum and N. J. Cohen, *From conditioning to conscious recollection: Memory systems of the brain*. No. 35, Oxford University Press on Demand, 2004.

[54] L. R. Squire, C. E. Stark, and R. E. Clark, "The medial temporal lobe," *Annu. Rev. Neurosci.*, vol. 27, pp. 279–306, 2004.

[55] R. Lorente de Nó, "Studies on the structure of the cerebral cortex. ii. continuation of the study of the ammonic system.," *Journal für Psychologie und Neurologie*, 1934.

[56] N. Ishizuka, W. M. Cowan, and D. G. Amaral, "A quantitative analysis of the dendritic organization of pyramidal cells in the rat hippocampus," *Journal of Comparative Neurology*, vol. 362, no. 1, pp. 17–45, 1995.

[57] G. K. Pyapali, A. Sik, M. Penttonen, G. Buzsaki, and D. A. Turner, "Dendritic properties of hippocampal ca1 pyramidal neurons in the rat: intracellular staining in vivo and in vitro," *Journal of Comparative Neurology*, vol. 391, no. 3, pp. 335–352, 1998.

[58] P. Andersen, T. Bliss, and K. K. Skrede, "Lamellar organization of hippocampal excitatory pathways," *Experimental Brain Research*, vol. 13, no. 2, pp. 222–238, 1971.

[59] W. Deng, J. B. Aimone, and F. H. Gage, "New neurons and new memories: how does adult hippocampal neurogenesis affect learning and memory?," *Nature Reviews Neuroscience*, vol. 11, no. 5, pp. 339–350, 2010.

[60] P. Andersen, *The hippocampus book*. Oxford university press, 2007.

[61] J. A. Kemp and R. M. McKernan, "Nmda receptor pathways as drug targets," *Nature neuroscience*, vol. 5, pp. 1039–1042, 2002.

[62] M. Jansen and G. Dannhardt, "Antagonists and agonists at the glycine site of the nmda receptor for therapeutic interventions," *European journal of medicinal chemistry*, vol. 38, no. 7, pp. 661–670, 2003.

[63] P. L. Chazot, "The nmda receptor nr2b subunit: a valid therapeutic target for multiple cns pathologies," *Current medicinal chemistry*, vol. 11, no. 3, pp. 389–396, 2004.

[64] M. R. Farlow, "Nmda receptor antagonists. a new therapeutic approach for alzheimer's disease.," *Geriatrics*, vol. 59, no. 6, pp. 22–27, 2004.

[65] R. Dingledine, K. Borges, D. Bowie, and S. F. Traynelis, "The glutamate receptor ion channels," *Pharmacological reviews*, vol. 51, no. 1, pp. 7–62, 1999.

[66] H. Mori and M. Mishina, "Structure and function of the nmda receptor channel," *Neuropharmacology*, vol. 34, no. 10, pp. 1219–1237, 1995.

[67] S. Das, Y. F. Sasaki, T. Rothe, L. S. Premkumar, M. Takasu, J. E. Crandall, P. Dikkes, D. A. Conner, P. V. Rayudu, W. Cheung, *et al.*, "Increased nmda current and spine density in mice lacking the nmda receptor subunit nr3a," *Nature*, vol. 393, no. 6683, pp. 377–381, 1998.

[68] M. Nishi, H. Hinds, H.-P. Lu, M. Kawata, and Y. Hayashi, "Motoneuron-specific expression of nr3b, a novel nmda-type glutamate receptor subunit that works in a dominant-negative manner," *J Neurosci*, vol. 21, no. 23, p. 185RC, 2001.

[69] R. S. Zukin and M. V. Bennett, "Alternatively spliced isoforms of the nmdari receptor subunit," *Trends in neurosciences*, vol. 18, no. 7, pp. 306–313, 1995.

[70] K. Prybylowski, S. Grossman, J. Wrathall, and B. Wolfe, "Expression of splice variants of the nr1 subunit of the n-methyl-d-aspartate receptor in the normal and injured rat spinal cord," *Journal of neurochemistry*, vol. 76, no. 3, pp. 797–805, 2001.

[71] G. A. Wray, M. W. Hahn, E. Abouheif, J. P. Balhoff, M. Pizer, M. V. Rockman, and L. A. Romano, "The evolution of transcriptional regulation in eukaryotes," *Molecular biology and evolution*, vol. 20, no. 9, pp. 1377–1419, 2003.

[72] G. A. Wray, M. W. Hahn, E. Abouheif, J. P. Balhoff, M. Pizer, M. V. Rockman, and L. A. Romano, "The evolution of transcriptional regulation in eukaryotes," *Molecular biology and evolution*, vol. 20, no. 9, pp. 1377–1419, 2003.

[73] M. Levine and R. Tjian, "Transcription regulation and animal diversity," *Nature*, vol. 424, no. 6945, pp. 147–151, 2003.

[74] A. M. VanDongen, *Biology of the NMDA Receptor*. CRC Press, 2008.

[75] T. V. Bliss and G. L. Collingridge, "A synaptic model of memory: long-term potentiation in the hippocampus.," *Nature*, vol. 361, no. 6407, p. 31, 1993.

[76] B. L. McNaughton, R. Douglas, and G. V. Goddard, "Synaptic enhancement in fascia dentata: cooperativity among coactive afferents," *Brain research*, vol. 157, no. 2, pp. 277–293, 1978.

[77] D. M. Lovinger and A. Routtenberg, "Synapse-specific protein kinase c activation enhances maintenance of long-term potentiation in rat hippocampus.," *The Journal of physiology*, vol. 400, no. 1, pp. 321–333, 1988.

[78] R. C. Malenka, "Postsynaptic factors control the duration of synaptic enhancement in area ca1 of the hippocampus," *Neuron*, vol. 6, no. 1, pp. 53–60, 1991.

[79] W. B. Levy and O. Steward, "Synapses as associative memory elements in the hippocampal formation," *Brain research*, vol. 175, no. 2, pp. 233–245, 1979.

[80] G. Collingridge, S. Kehl, and H. t. McLennan, "Excitatory amino acids in synaptic transmission in the schaffer collateral-commissural pathway of the rat hippocampus.," *The Journal of physiology*, vol. 334, no. 1, pp. 33–46, 1983.

[81] P. Ascher and L. Nowak, "The role of divalent cations in the n-methyl-d-aspartate responses of mouse central neurones in culture.," *The Journal of Physiology*, vol. 399, p. 247, 1988.

[82] E. R. Kandel, J. H. Schwartz, T. M. Jessell, S. A. Siegelbaum, and A. J. Hudspeth, *Principles of neural science*, vol. 4. McGraw-hill New York, 2000.

[83] I. B. Zovkic and J. D. Sweatt, "Epigenetic mechanisms in learned fear: implications for ptsd," *Neuropsychopharmacology*, vol. 38, no. 1, pp. 77–93, 2013.

[84] T. Reese and M. J. Karnovsky, "Fine structural localization of a blood-brain barrier to exogenous peroxidase," *The Journal of cell biology*, vol. 34, no. 1, pp. 207–217, 1967.

[85] L. Rubin and J. Staddon, "The cell biology of the blood-brain barrier," *Annual review of neuroscience*, vol. 22, no. 1, pp. 11–28, 1999.

[86] L. P. Rowland, M. E. Fink, and L. Rubin, "Cerebrospinal fluid: blood-brain barrier, brain edema, and hydrocephalus," *Principles of neural science, 3rd edition. New York: Elsevier*, pp. 1050–1060, 1991.

[87] W. M. Pardridge, "Drug delivery to the brain," *Journal of Cerebral Blood Flow & Metabolism*, vol. 17, no. 7, pp. 713–731, 1997.

[88] R. Daneman, L. Zhou, A. A. Kebede, and B. A. Barres, "Pericytes are required for blood-brain barrier integrity during embryogenesis," *Nature*, vol. 468, no. 7323, pp. 562–566, 2010.

[89] A. Armulik, G. Genové, M. Mäe, M. H. Nisancioglu, E. Wallgard, C. Niaudet, L. He, J. Norlin, P. Lindblom, K. Strittmatter, *et al.*, "Pericytes regulate the blood-brain barrier," *Nature*, vol. 468, no. 7323, pp. 557–561, 2010.

[90] R. D. Bell, E. A. Winkler, A. P. Sagare, I. Singh, B. LaRue, R. Deane, and B. V. Zlokovic, "Pericytes control key neurovascular functions and neuronal phenotype in the adult brain and during brain aging," *Neuron*, vol. 68, no. 3, pp. 409–427, 2010.

[91] E. A. Winkler, J. D. Sengillo, R. D. Bell, J. Wang, and B. V. Zlokovic, "Blood–spinal cord barrier pericyte reductions contribute to increased capillary permeability," *Journal of Cerebral Blood Flow & Metabolism*, vol. 32, no. 10, pp. 1841–1852, 2012.

[92] E. Chryssolouris, *Laser machining: theory and practice*. Springer Science & Business Media, 2013.

[93] A. Stournaras, K. Salonitis, P. Stavropoulos, and G. Chryssolouris, "Theoretical and experimental investigation of pulsed laser grooving process," *The International Journal of Advanced Manufacturing Technology*, vol. 44, no. 1-2, pp. 114–124, 2009.

[94] A. Corcoran, L. Sexton, B. Seaman, P. Ryan, and G. Byrne, "The laser drilling of multi-layer aerospace material systems," *Journal of Materials Processing Technology*, vol. 123, no. 1, pp. 100–106, 2002.

[95] C. Yeo, "The physics of laser processing," *J. Mater. Process. Technol*, vol. 42, pp. 15–49, 1994.

[96] S. Barcikowski, A. Hahn, and J. Walter, "Health risks of nanoparticulate emissions during femtosecond and picosecond pulsed laser machining," in *SPIE LASE: Lasers and Applications in Science and Engineering*, pp. 720109–720109, International Society for Optics and Photonics, 2009.

[97] A. Elsaesser and C. V. Howard, "Toxicology of nanoparticles," *Advanced drug delivery reviews*, vol. 64, no. 2, pp. 129–137, 2012.

[98] J. Wang, M. F. Rahman, H. M. Duhart, G. D. Newport, T. A. Patterson, R. C. Murdock, S. M. Hussain, J. J. Schlager, and S. F. Ali, "Expression changes of dopaminergic system-related genes in pc12 cells induced by manganese, silver, or copper nanoparticles," *Neurotoxicology*, vol. 30, no. 6, pp. 926–933, 2009.

[99] S. Gosso, D. Gavello, C. N. Giachello, C. Franchino, E. Carbone, and V. Carabelli, "The effect of cdse–zns quantum dots on calcium currents and catecholamine secretion in mouse chromaffin cells," *Biomaterials*, vol. 32, no. 34, pp. 9040–9050, 2011.

[100] J. Cooper, F. Bloom, and R. Roth, "The biochemical basis of neuropharmacology. 2003."

[101] S. A. Shah, G. H. Yoon, A. Ahmad, F. Ullah, F. U. Amin, and M. O. Kim, "Nanoscale–alumina induces oxidative stress and accelerates amyloid beta production in icr female mice," *Nanoscale*, vol. 7, no. 37, pp. 15225–15237, 2015.

[102] T.-T. Win-Shwe and H. Fujimaki, "Nanoparticles and neurotoxicity," *International journal of molecular sciences*, vol. 12, no. 9, pp. 6267–6280, 2011.

[103] J. H. Sung, J. H. Ji, J. D. Park, J. U. Yoon, D. S. Kim, K. S. Jeon, M. Y. Song, J. Jeong, B. S. Han, J. H. Han, *et al.*, "Subchronic inhalation toxicity of silver nanoparticles," *Toxicological Sciences*, vol. 108, no. 2, pp. 452–461, 2009.

[104] R. Hu, X. Gong, Y. Duan, N. Li, Y. Che, Y. Cui, M. Zhou, C. Liu, H. Wang, and F. Hong, "Neurotoxicological effects and the impairment of spatial recognition memory in mice caused by exposure to tio 2 nanoparticles," *Biomaterials*, vol. 31, no. 31, pp. 8043–8050, 2010.

[105] Y.-S. Chen, Y.-C. Hung, L.-W. Lin, I. Liau, M.-Y. Hong, and G. S. Huang, "Size-dependent impairment of cognition in mice caused by the injection of gold nanoparticles," *Nanotechnology*, vol. 21, no. 48, p. 485102, 2010.

[106] D. J. BEGLEY, "The blood-brain barrier: Principles for targeting peptides and drugs to the central nervous system," *Journal of pharmacy and pharmacology*, vol. 48, no. 2, pp. 136–146, 1996.

[107] A. De Lorenzo, "The olfactory neuron and the blood-brain barrier," in *Ciba foundation symposium-taste and smell in vertebrates*, pp. 151–176, Wiley Online Library, 2008.

[108] S. Takenaka, E. Karg, C. Roth, H. Schulz, A. Ziesenis, U. Heinzmann, P. Schramel, and J. Heyder, "Pulmonary and systemic distribution of inhaled ultrafine silver particles in rats.," *Environmental health perspectives*, vol. 109, no. Suppl 4, p. 547, 2001.

[109] S. Yamamoto, S. Ahmed, M. Kakeyama, T. Kobayashi, H. Fujimaki, *et al.*, "Brain cytokine and chemokine mrna expression in mice induced by intranasal instillation with ultrafine carbon black," *Toxicology letters*, vol. 163, no. 2, pp. 153–160, 2006.

[110] Y. Ze, L. Sheng, X. Zhao, J. Hong, X. Ze, X. Yu, X. Pan, A. Lin, Y. Zhao, C. Zhang, *et al.*, "Tio 2 nanoparticles induced hippocampal neuroinflammation in mice," *PloS one*, vol. 9, no. 3, p. e92230, 2014.

[111] L. L. Davenport, H. Hsieh, B. L. Eppert, V. S. Carreira, M. Krishan, T. Ingle, P. C. Howard, M. T. Williams, C. V. Vorhees, and M. B. Genter, "Systemic and behavioral effects of intranasal administration of silver nanoparticles," *Neurotoxicology and teratology*, vol. 51, pp. 68–76, 2015.

[112] T.-T. Win-Shwe, D. Mitsushima, S. Yamamoto, Y. Fujitani, T. Funabashi, S. Hirano, and H. Fujimaki, "Extracellular glutamate level and nmda receptor subunit expression in mouse olfactory bulb following nanoparticle-rich diesel exhaust exposure," *Inhalation toxicology*, vol. 21, no. 10, pp. 828–836, 2009.

[113] D. Han, Y. Tian, T. Zhang, G. Ren, and Z. Yang, "Nano-zinc oxide damages spatial cognition capability via over-enhanced long-term potentiation in hippocampus of wistar rats," *International journal of nanomedicine*, 2011.

[114] R. Hu, X. Gong, Y. Duan, N. Li, Y. Che, Y. Cui, M. Zhou, C. Liu, H. Wang, and F. Hong, "Neurotoxicological effects and the impairment of spatial recognition memory in mice caused by exposure to tio 2 nanoparticles," *Biomaterials*, vol. 31, no. 31, pp. 8043–8050, 2010.

[115] Y. Liu, W. Guan, G. Ren, and Z. Yang, "The possible mechanism of silver nanoparticle impact on hippocampal synaptic plasticity and spatial cognition in rats," *Toxicology letters*, vol. 209, no. 3, pp. 227–231, 2012.

[116] J. H. Sung, J. H. Ji, J. D. Park, J. U. Yoon, D. S. Kim, K. S. Jeon, M. Y. Song, J. Jeong, B. S. Han, J. H. Han, *et al.*, "Subchronic inhalation toxicity of silver nanoparticles," *Toxicological Sciences*, vol. 108, no. 2, pp. 452–461, 2009.

[117] L. CALDERon-GARCIDUEnas, W. Reed, R. R. Maronpot, C. Henriquez-Roldán, R. Delgado-Chavez, A. CALDERon-GARCIDUEnas, I. Dragustinovis, M. Franco-Lira, M. Aragón-Flores, A. C. Solt, *et al.*, "Brain inflammation and alzheimer's-like pathology in individuals exposed to severe air pollution," *Toxicologic pathology*, vol. 32, no. 6, pp. 650–658, 2004.

[118] B. Crüts, L. van Etten, H. Törnqvist, A. Blomberg, T. Sandström, N. L. Mills, and P. J. Borm, "Exposure to diesel exhaust induces changes in eeg in human volunteers," *Particle and fibre toxicology*, vol. 5, no. 1, p. 4, 2008.

[119] M. E. Shils and M. Shike, *Modern nutrition in health and disease*. Lippincott Williams & Wilkins, 2006.

[120] R. Uauy, M. Olivares, and M. Gonzalez, "Essentiality of copper in humans.," *The American journal of clinical nutrition*, vol. 67, no. 5, pp. 952S–959S, 1998.

[121] B. P. Zietz, H. H. Dieter, M. Lakomek, H. Schneider, B. Keßler-Gaedtke, and H. Dunkelberg, "Epidemiological investigation on chronic copper toxicity to children exposed via the public drinking water supply," *Science of the Total Environment*, vol. 302, no. 1, pp. 127–144, 2003.

[122] C. M. Galhardi, Y. S. Diniz, L. A. Faine, H. G. Rodrigues, R. C. Burneiko, B. O. Ribas, and E. L. Novelli, "Toxicity of copper intake: lipid profile, oxidative stress and susceptibility to renal dysfunction," *Food and chemical toxicology*, vol. 42, no. 12, pp. 2053–2060, 2004.

[123] E. Ebrahimnia-Bajestan, H. Niazmand, W. Duangthongsuk, and S. Wongwises, "Numerical investigation of effective parameters in convective heat transfer of nanofluids flowing under a laminar flow regime," *International journal of heat and mass transfer*, vol. 54, no. 19, pp. 4376–4388, 2011.

[124] O. Bondarenko, K. Juganson, A. Ivask, K. Kasemets, M. Mortimer, and A. Kahru, "Toxicity of ag, cuo and zno nanoparticles to selected environmentally relevant test organisms and mammalian cells in vitro: a critical review," *Archives of toxicology*, vol. 87, no. 7, pp. 1181–1200, 2013.

[125] R. Das, S. Gang, S. S. Nath, and R. Bhattacharjee, "Linoleic acid capped copper nanoparticles for antibacterial activity," *Journal of Bionanoscience*, vol. 4, no. 1-2, pp. 82–86, 2010.

[126] L. Esteban-Tejeda, F. Malpartida, A. Esteban-Cubillo, C. Pecharromán, and J. Moya, "Antibacterial and antifungal activity of a soda-lime glass containing copper nanoparticles," *Nanotechnology*, vol. 20, no. 50, p. 505701, 2009.

[127] A. P. Ingle, N. Duran, and M. Rai, "Bioactivity, mechanism of action, and cytotoxicity of copper-based nanoparticles: a review," *Applied microbiology and biotechnology*, vol. 98, no. 3, pp. 1001–1009, 2014.

[128] Z. Chen, H. Meng, G. Xing, C. Chen, Y. Zhao, G. Jia, T. Wang, H. Yuan, C. Ye, F. Zhao, *et al.*, "Acute toxicological effects of copper nanoparticles in vivo," *Toxicology letters*, vol. 163, no. 2, pp. 109–120, 2006.

[129] K. Donaldson, X. Li, and W. MacNee, "Ultrafine (nanometre) particle mediated lung injury," *Journal of Aerosol Science*, vol. 29, no. 5, pp. 553–560, 1998.

[130] D. B. Warheit, B. R. Laurence, K. L. Reed, D. H. Roach, G. A. Reynolds, and T. R. Webb, "Comparative pulmonary toxicity assessment of single-wall carbon nanotubes in rats," *Toxicological sciences*, vol. 77, no. 1, pp. 117–125, 2004.

[131] M. Bruchez, M. Moronne, P. Gin, S. Weiss, and A. P. Alivisatos, "Semiconductor nanocrystals as fluorescent biological labels," *science*, vol. 281, no. 5385, pp. 2013–2016, 1998.

[132] G. Oberdörster, Z. Sharp, V. Atudorei, A. Elder, R. Gelein, W. Kreyling, and C. Cox, "Translocation of inhaled ultrafine particles to the brain," *Inhalation toxicology*, vol. 16, no. 6-7, pp. 437–445, 2004.

[133] H. S. Sharma, S. Hussain, J. Schlager, S. F. Ali, and A. Sharma, "Influence of nanoparticles on blood–brain barrier permeability and brain edema formation in rats," in *Brain edema XIV*, pp. 359–364, Springer, 2010.

[134] K. Kravchyk, L. Protesescu, M. I. Bodnarchuk, F. Krumeich, M. Yarema, M. Walter, C. Guntlin, and M. V. Kovalenko, "Monodisperse and inorganically capped sn and sn/sno2 nanocrystals for high-performance li-ion battery anodes," *Journal of the American Chemical Society*, vol. 135, no. 11, pp. 4199–4202, 2013.

[135] M. N. RITTNER, "Market analysis of nanostructured materials," *American Ceramic Society Bulletin*, vol. 81, no. 3, pp. 33–36, 2002.

[136] L. Jodin, A.-C. Dupuis, E. Rouvière, and P. Reiss, "Influence of the catalyst type on the growth of carbon nanotubes via methane chemical vapor deposition," *The Journal of Physical Chemistry B*, vol. 110, no. 14, pp. 7328–7333, 2006.

[137] A. Bertsch, S. Jiguet, and P. Renaud, "Microfabrication of ceramic components by microstereolithography," *Journal of micromechanics and microengineering*, vol. 14, no. 2, p. 197, 2003.

[138] J. Cho, M. Joshi, and C. Sun, "Effect of inclusion size on mechanical properties of polymeric composites with micro and nano particles," *Composites Science and Technology*, vol. 66, no. 13, pp. 1941–1952, 2006.

[139] T. Textor, F. Schröter, and E. Schollmeyer, "Functionalisation of textiles with nanotechnology," *MRS Online Proceedings Library Archive*, vol. 920, 2006.

[140] S. Pacheco, M. Medina, F. Valencia, and J. Tapia, "Removal of inorganic mercury from polluted water using structured nanoparticles," *Journal of environmental engineering*, vol. 132, no. 3, pp. 342–349, 2006.

[141] J. Li, Y. Wang, J. Wang, M. Harvey, D. Atwood, and L. Bachas, "Immobilization of phosphorylated proteins on alumina nanoparticles: Toward nanosize biosensors.," in *ABSTRACTS OF PAPERS OF THE AMERICAN CHEMICAL SOCIETY*, vol. 221, pp. U81–U81, AMER CHEMICAL SOC 1155 16TH ST, NW, WASHINGTON, DC 20036 USA, 2001.

[142] K. C. Popat, G. Mor, C. A. Grimes, and T. A. Desai, "Surface modification of nanoporous alumina surfaces with poly (ethylene glycol)," *Langmuir*, vol. 20, no. 19, pp. 8035–8041, 2004.

[143] A. Frey, N. Mantis, P. A. Kozlowski, A. J. Quayle, A. Bajardi, J. J. Perdomo, F. A. Robey, and M. R. Neutra, "Immunization of mice with peptomers covalently coupled to aluminum oxide nanoparticles," *Vaccine*, vol. 17, no. 23, pp. 3007–3019, 1999.

[144] E. Oesterling, N. Chopra, V. Gavalas, X. Arzuaga, E. J. Lim, R. Sultana, D. A. Butterfield, L. Bachas, and B. Hennig, "Alumina nanoparticles induce expression of endothelial cell adhesion molecules," *Toxicology letters*, vol. 178, no. 3, pp. 160–166, 2008.

[145] A. J. Wagner, C. A. Bleckmann, R. C. Murdock, A. M. Schrand, J. J. Schlager, and S. M. Hussain, "Cellular interaction of different forms of aluminum nanoparticles in rat alveolar macrophages," *The Journal of Physical Chemistry B*, vol. 111, no. 25, pp. 7353–7359, 2007.

[146] W. Lin, I. Stayton, Y.-w. Huang, X.-D. Zhou, and Y. Ma, "Cytotoxicity and cell membrane depolarization induced by aluminum oxide nanoparticles in human lung epithelial cells a549," *Toxicological and Environmental Chemistry*, vol. 90, no. 5, pp. 983–996, 2008.

[147] Q. Zhang, M. Li, J. Ji, F. Gao, R. Bai, C. Chen, Z. Wang, C. Zhang, and Q. Niu, "In vivo toxicity of nano-alumina on mice neurobehavioral profiles and the potential mechanisms.," *International journal of immunopathology and pharmacology*, vol. 24, no. 1 Suppl, pp. 23S–29S, 2010.

[148] S. A. Shah, G. H. Yoon, A. Ahmad, F. Ullah, F. U. Amin, and M. O. Kim, "Nanoscale-alumina induces oxidative stress and accelerates amyloid beta (aβ) production in icr female mice," *Nanoscale*, vol. 7, no. 37, pp. 15225–15237, 2015.

[149] J. H. Sung, J. H. Ji, J. U. Yoon, D. S. Kim, M. Y. Song, J. Jeong, B. S. Han, J. H. Han, Y. H. Chung, J. Kim, *et al.*, "Lung function changes in sprague-dawley rats after prolonged inhalation exposure to silver nanoparticles," *Inhalation toxicology*, vol. 20, no. 6, pp. 567–574, 2008.

[150] J. H. Sung, J. H. Ji, J. D. Park, M. Y. Song, K. S. Song, H. R. Ryu, J. U. Yoon, K. S. Jeon, J. Jeong, B. S. Han, *et al.*, "Subchronic inhalation toxicity of gold nanoparticles," *Particle and Fibre Toxicology*, vol. 8, no. 1, p. 16, 2011.

[151] L. Prut and C. Belzung, "The open field as a paradigm to measure the effects of drugs on anxiety-like behaviors: a review," *European journal of pharmacology*, vol. 463, no. 1, pp. 3–33, 2003.

[152] R. Rodgers and A. Dalvi, "Anxiety, defence and the elevated plus-maze," *Neuroscience & Biobehavioral Reviews*, vol. 21, no. 6, pp. 801–810, 1997.

[153] A. Can, D. T. Dao, M. Arad, C. E. Terrillion, S. C. Piantadosi, and T. D. Gould, "The mouse forced swim test," *JoVE (Journal of Visualized Experiments)*, no. 59, pp. e3638–e3638, 2012.

[154] P. J. Livesey, J. Bell, and V. Manyam, "Disruption of passive avoidance learning in the rat by electrical stimulation of the hippocampus.," *Behavioral neuroscience*, vol. 98, no. 4, p. 567, 1984.

[155] M. Tsuji, H. Takeda, and T. Matsumiya, "Modulation of passive avoidance in mice by the 5-ht1a receptor agonist flesinoxan: comparison with the benzodiazepine receptor agonist diazepam.," *Neuropsychopharmacology: official publication of the American College of Neuropsychopharmacology*, vol. 28, no. 4, pp. 664–674, 2003.

[156] N. Çarçak, E. Dileköz, R. Gülhan, R. Onur, F. Y. Onat, and Y. Sara, "Increased inhibitory synaptic activity in the hippocampus (ca1) of genetic absence epilepsy rats: Relevance of kindling resistance," *Epilepsy research*, vol. 126, pp. 70–77, 2016.

[157] G. Paxinos and C. Watson, "The rat brain in stereotaxic coordinates: compact. academic press," *San Diego*, 1997.

[158] P. Chomczynski, "A reagent for the single-step simultaneous isolation of rna, dna and proteins from cell and tissue samples.," *Biotechniques*, vol. 15, no. 3, pp. 532–4, 1993.

[159] C. Kursungoz, "Determination of hypothalamic neuropeptide levels involved in appetite regulation in atypical antipsychotic drug, risperidone treatment," 2012.

[160] M. W. Pfaffl, "A new mathematical model for relative quantification in real-time rt–pcr," *Nucleic acids research*, vol. 29, no. 9, pp. e45–e45, 2001.

[161] O. H. Lowry, N. J. Rosebrough, A. L. Farr, R. J. Randall, *et al.*, "Protein measurement with the folin phenol reagent," *J biol Chem*, vol. 193, no. 1, pp. 265–275, 1951.

[162] G. L. Peterson, "Review of the folin phenol protein quantitation method of lowry, rosebrough, farr and randall," *Analytical biochemistry*, vol. 100, no. 2, pp. 201–220, 1979.

[163] S. Ghaderi, S. R. F. Tabatabaei, H. N. Varzi, and M. Rashno, "Induced adverse effects of prenatal exposure to silver nanoparticles on neurobehavioral development of offspring of mice," *The Journal of toxicological sciences*, vol. 40, no. 2, pp. 263–275, 2015.

[164] L. K. Fonken, X. Xu, Z. M. Weil, G. Chen, Q. Sun, S. Rajagopalan, and R. J. Nelson, "Air pollution impairs cognition, provokes depressive-like behaviors and alters hippocampal cytokine expression and morphology," *Molecular psychiatry*, vol. 16, no. 10, pp. 987–995, 2011.

[165] I. Ben-Slama, I. Mrad, N. Rihane, L. E. Mir, M. Sakly, and S. Amara, "Sub-acute oral toxicity of zinc oxide nanoparticles in male rats," *Journal of Nanomedicine & Nanotechnology*, vol. 6, no. 3, p. 1, 2015.

[166] L. Prut and C. Belzung, "The open field as a paradigm to measure the effects of drugs on anxiety-like behaviors: a review," *European journal of pharmacology*, vol. 463, no. 1, pp. 3–33, 2003.

[167] R. Rodgers and J. Cole, "The elevated plus-maze: pharmacology, methodology and ethology," *Ethology and psychopharmacology*, vol. 1994, pp. 9–43, 1994.

[168] N. R. B. Younes, S. Amara, I. Mrad, I. Ben-Slama, M. Jeljeli, K. Omri, J. El Ghoul, L. El Mir, K. B. Rhouma, H. Abdelmelek, *et al.*, "Subacute toxicity of titanium dioxide (tio2) nanoparticles in male rats: emotional behavior and pathophysiological examination," *Environmental Science and Pollution Research*, vol. 22, no. 11, pp. 8728–8737, 2015.

[169] D. A. Davis, M. Bortolato, S. C. Godar, T. K. Sander, N. Iwata, P. Pakbin, J. C. Shih, K. Berhane, R. McConnell, C. Sioutas, *et al.*, "Prenatal exposure to urban air nanoparticles in mice causes altered neuronal differentiation and depression-like responses," *PloS one*, vol. 8, no. 5, p. e64128, 2013.

[170] V. Castagné, P. Moser, S. Roux, and R. D. Porsolt, "Rodent models of depression: forced swim and tail suspension behavioral despair tests in rats and mice," *Curr Protoc Neurosci*, vol. 55, no. 8.10, pp. 1–8, 2011.

[171] A. Mohammadipour, A. Fazel, H. Haghir, F. Motejaded, H. Rafatpanah, H. Zabihi, M. Hosseini, and A. E. Bideskan, "Maternal exposure to titanium dioxide nanoparticles during pregnancy; impaired memory and decreased hippocampal cell proliferation in rat offspring," *Environmental toxicology and pharmacology*, vol. 37, no. 2, pp. 617–625, 2014.

[172] R. M. Joy and T. E. Albertson, "Nmda receptors have a dominant role in population spike-paired pulse facilitation in the dentate gyrus of urethane-anesthetized rats," *Brain research*, vol. 604, no. 1, pp. 273–282, 1993.

[173] C. Papatheodoropoulos, "Striking differences in synaptic facilitation along the dorsoventral axis of the hippocampus," *Neuroscience*, vol. 301, pp. 454–470, 2015.

[174] L. An, S. Liu, Z. Yang, and T. Zhang, "Cognitive impairment in rats induced by nano-cuo and its possible mechanisms," *Toxicology letters*, vol. 213, no. 2, pp. 220–227, 2012.

[175] D. Han, Y. Tian, T. Zhang, G. Ren, and Z. Yang, "Nano-zinc oxide damages spatial cognition capability via over-enhanced long-term potentiation in hippocampus of wistar rats," *International journal of nanomedicine*, 2011.

[176] J. Blahos and R. J. Wenthold, "Relationship between n-methyl-d-aspartate receptor nr1 splice variants and nr2 subunits," *Journal of Biological Chemistry*, vol. 271, no. 26, pp. 15669–15674, 1996.

[177] T. Ishii, K. Moriyoshi, H. Sugihara, K. Sakurada, H. Kadotani, M. Yokoi, C. Akazawa, R. Shigemoto, N. Mizuno, and M. Masu, "Molecular characterization of the family of the n-methyl-d-aspartate receptor subunits.," *Journal of Biological Chemistry*, vol. 268, no. 4, pp. 2836–2843, 1993.

[178] C. Marchetti and P. Gavazzo, "Nmda receptors as targets of heavy metal interaction and toxicity," *Neurotoxicity research*, vol. 8, no. 3-4, pp. 245–258, 2005.

[179] M. Mayer and G. Westbrook, "Permeation and block of n-methyl-d-aspartic acid receptor channels by divalent cations in mouse cultured central neurones.," *The Journal of physiology*, vol. 394, p. 501, 1987.

[180] P. Ascher and L. Nowak, "The role of divalent cations in the n-methyl-d-aspartate responses of mouse central neurones in culture.," *The Journal of Physiology*, vol. 399, p. 247, 1988.

[181] K. Kashiwagi, A. J. Pahk, T. Masuko, K. Igarashi, and K. Williams, "Block and modulation ofn-methyl-d-aspartate receptors by polyamines and protons: Role of amino acid residues in the transmembrane and pore-forming regions of nr1 and nr2 subunits," *Molecular Pharmacology*, vol. 52, no. 4, pp. 701–713, 1997.

[182] V. Vlachová, H. Zemková, and L. Vyklickỳ, "Copper modulation of nmda responses in mouse and rat cultured hippocampal neurons," *European Journal of Neuroscience*, vol. 8, no. 11, pp. 2257–2264, 1996.

[183] M. Llansola, M.-D. Miñana, C. Montoliu, R. Saez, R. Corbalán, L. Manzo, and V. Felipo, "Prenatal exposure to aluminum reduces expression of neuronal nitric oxide synthase and of soluble guanylate cyclase and impairs glutamatergic neurotransmission in rat cerebellum," *Journal of neurochemistry*, vol. 73, no. 2, pp. 712–718, 1999.

[184] S. J. Coultrap, K. M. Nixon, R. M. Alvestad, C. F. Valenzuela, and M. D. Browning, "Differential expression of nmda receptor subunits and splice variants among the ca1, ca3 and dentate gyrus of the adult rat," *Molecular brain research*, vol. 135, no. 1, pp. 104–111, 2005.

[185] A. Nemmar, P. M. Hoet, B. Vanquickenborne, D. Dinsdale, M. Thomeer, M. Hoylaerts, H. Vanbilloen, L. Mortelmans, and B. Nemery, "Passage of inhaled particles into the blood circulation in humans," *Circulation*, vol. 105, no. 4, pp. 411–414, 2002.

[186] S. Bakand, A. Hayes, and F. Dechsakulthorn, "Nanoparticles: a review of particle toxicology following inhalation exposure," *Inhalation toxicology*, vol. 24, no. 2, pp. 125–135, 2012.

[187] B. Asgharian, O. Price, and G. Oberdörster, "A modeling study of the effect of gravity on airflow distribution and particle deposition in the lung," *Inhalation toxicology*, vol. 18, no. 7, pp. 473–481, 2006.

[188] K. Siegmann, L. Scherrer, and H. Siegmann, "Physical and chemical properties of airborne nanoscale particles and how to measure the impact on human health," *Journal of Molecular Structure: THEOCHEM*, vol. 458, no. 1, pp. 191–201, 1998.

[189] C. Lambre, M. Aufderheide, R. E. Bolton, and B. Fubini, "In vitro tests for respiratory toxicity. the report and recommandations of ecvam worshop 18," *ATLA-Alternatives to Laboratory Animals*, vol. 24, no. 5, pp. 671–681, 1996.

[190] S. Bakand, C. Winder, C. Khalil, and A. Hayes, "Toxicity assessment of industrial chemicals and airborne contaminants: transition from in vivo to in vitro test methods: a review," *Inhalation Toxicology*, vol. 17, no. 13, pp. 775–787, 2005.

[191] F. Blank, P. Gehr, and B. Rothen-Rutishauser, "In vitro human lung cell culture models to study the toxic potential of nanoparticles," *Nanotoxicity: From in vitro, in vivo models to health risks*, pp. 379–95, 2009.

[192] M. Lundborg, U. Johard, L. Låstbom, P. Gerde, and P. Camner, "Human alveolar macrophage phagocytic function is impaired by aggregates of ultrafine carbon particles," *Environmental research*, vol. 86, no. 3, pp. 244–253, 2001.

[193] D. M. Brown, I. A. Kinloch, U. Bangert, A. Windle, D. Walter, G. Walker, C. Scotchford, K. Donaldson, and V. Stone, "An in vitro study of the potential of carbon nanotubes and nanofibres to induce inflammatory mediators and frustrated phagocytosis," *Carbon*, vol. 45, no. 9, pp. 1743–1756, 2007.

[194] D. Curtis, "Casarett and doulls toxicology," *Ed McGraw Hill. UEA*, 2001.

[195] Q. Li, H. Liu, M. Alattar, S. Jiang, J. Han, Y. Ma, and C. Jiang, "The preferential accumulation of heavy metals in different tissues following frequent respiratory exposure to pm2. 5 in rats," *Scientific reports*, vol. 5, 2015.

[196] S. Bakand and A. Hayes, "Toxicological considerations, toxicity assessment, and risk management of inhaled nanoparticles," *International journal of molecular sciences*, vol. 17, no. 6, p. 929, 2016.

[197] W. H. De Jong, W. I. Hagens, P. Krystek, M. C. Burger, A. J. Sips, and R. E. Geertsma, "Particle size-dependent organ distribution of gold nanoparticles after intravenous administration," *Biomaterials*, vol. 29, no. 12, pp. 1912–1919, 2008.

[198] B. Trouiller, R. Reliene, A. Westbrook, P. Solaimani, and R. H. Schiestl, "Titanium dioxide nanoparticles induce dna damage and genetic instability in vivo in mice," *Cancer research*, vol. 69, no. 22, pp. 8784–8789, 2009.

[199] V. H. Grassian, P. T. O'Shaughnessy, A. Adamcakova-Dodd, J. M. Pettibone, and P. S. Thorne, "Inhalation exposure study of titanium dioxide nanoparticles with a primary particle size of 2 to 5 nm," *Environmental health perspectives*, pp. 397–402, 2007.

[200] K. Loeschner, N. Hadrup, K. Qvortrup, A. Larsen, X. Gao, U. Vogel, A. Mortensen, H. R. Lam, and E. H. Larsen, "Distribution of silver in rats following 28 days of repeated oral exposure to silver nanoparticles or silver acetate," *Particle and fibre toxicology*, vol. 8, no. 1, p. 18, 2011.

[201] M. van der Zande, R. J. Vandebriel, E. Van Doren, E. Kramer, Z. Herrera Rivera, C. S. Serrano-Rojero, E. R. Gremmer, J. Mast, R. J. Peters, P. C. Hollman, *et al.*, "Distribution, elimination, and toxicity of silver nanoparticles and silver ions in rats after 28-day oral exposure," *ACS nano*, vol. 6, no. 8, pp. 7427–7442, 2012.

[202] Y. S. Kim, J. S. Kim, H. S. Cho, D. S. Rha, J. M. Kim, J. D. Park, B. S. Choi, R. Lim, H. K. Chang, Y. H. Chung, *et al.*, "Twenty-eight-day oral toxicity, genotoxicity, and gender-related tissue distribution of silver nanoparticles in sprague-dawley rats," *Inhalation toxicology*, vol. 20, no. 6, pp. 575–583, 2008.

[203] Z. Chen, H. Meng, G. Xing, H. Yuan, F. Zhao, R. Liu, X. Chang, X. Gao, T. Wang, G. Jia, *et al.*, "Age-related differences in pulmonary and cardiovascular responses to sio2 nanoparticle inhalation: nanotoxicity has susceptible population," *Environmental science & technology*, vol. 42, no. 23, pp. 8985–8992, 2008.

[204] A. Kermanizadeh, B. Gaiser, H. Johnston, D. Brown, and V. Stone, "Toxicological effect of engineered nanomaterials on the liver," *British journal of pharmacology*, vol. 171, no. 17, pp. 3980–3987, 2014.

[205] J. Dumkova, L. Vrlikova, Z. Vecera, B. Putnova, B. Docekal, P. Mikuska, P. Fictum, A. Hampl, and M. Buchtova, "Inhaled cadmium oxide nanoparticles: their in vivo fate and effect on target organs," *International journal of molecular sciences*, vol. 17, no. 6, p. 874, 2016.

[206] V. I. Shubayev, T. R. Pisanic, and S. Jin, "Magnetic nanoparticles for theragnostics," *Advanced drug delivery reviews*, vol. 61, no. 6, pp. 467–477, 2009.

[207] Z. Lan and W.-X. Yang, "Nanoparticles and spermatogenesis: how do nanoparticles affect spermatogenesis and penetrate the blood–testis barrier," *Nanomedicine*, vol. 7, no. 4, pp. 579–596, 2012.

[208] C. Li, S. Taneda, K. Taya, G. Watanabe, X. Li, Y. Fujitani, Y. Ito, T. Nakajima, and A. K. Suzuki, "Effects of inhaled nanoparticle-rich diesel exhaust on regulation of testicular function in adult male rats," *Inhalation toxicology*, vol. 21, no. 10, pp. 803–811, 2009.

[209] X. Chen and H. Schluesener, "Nanosilver: a nanoproduct in medical application," *Toxicology letters*, vol. 176, no. 1, pp. 1–12, 2008.

[210] O. C. Farokhzad, J. Cheng, B. A. Teply, I. Sherifi, S. Jon, P. W. Kantoff, J. P. Richie, and R. Langer, "Targeted nanoparticle-aptamer bioconjugates for cancer chemotherapy in vivo," *Proceedings of the National Academy of Sciences*, vol. 103, no. 16, pp. 6315–6320, 2006.

[211] P. H. Hoet, I. Brüske-Hohlfeld, and O. V. Salata, "Nanoparticles–known and unknown health risks," *Journal of nanobiotechnology*, vol. 2, no. 1, p. 12, 2004.

[212] M. Singh, S. Singh, S. Prasad, and I. Gambhir, "Nanotechnology in medicine and antibacterial effect of silver nanoparticles," *Digest Journal of Nanomaterials and Biostructures*, vol. 3, no. 3, pp. 115–122, 2008.

[213] Y. S. Kim, J. S. Kim, H. S. Cho, D. S. Rha, J. M. Kim, J. D. Park, B. S. Choi, R. Lim, H. K. Chang, Y. H. Chung, *et al.*, "Twenty-eight-day oral toxicity, genotoxicity, and gender-related tissue distribution of silver nanoparticles in sprague-dawley rats," *Inhalation toxicology*, vol. 20, no. 6, pp. 575–583, 2008.

[214] N. Li, C. Sioutas, A. Cho, D. Schmitz, C. Misra, J. Sempf, M. Wang, T. Oberley, J. Froines, and A. Nel, "Ultrafine particulate pollutants induce oxidative stress and mitochondrial damage.," *Environmental health perspectives*, vol. 111, no. 4, p. 455, 2003.

[215] J. H. Sung, J. H. Ji, J. D. Park, J. U. Yoon, D. S. Kim, K. S. Jeon, M. Y. Song, J. Jeong, B. S. Han, J. H. Han, *et al.*, "Subchronic inhalation toxicity of silver nanoparticles," *Toxicological Sciences*, vol. 108, no. 2, pp. 452–461, 2009.

[216] J. H. Ji, J. H. Jung, S. S. Kim, J.-U. Yoon, J. D. Park, B. S. Choi, Y. H. Chung, I. H. Kwon, J. Jeong, B. S. Han, *et al.*, "Twenty-eight-day inhalation toxicity study of silver nanoparticles in sprague-dawley rats," *Inhalation toxicology*, vol. 19, no. 10, pp. 857–871, 2007.

[217] M. Rahman, J. Wang, T. Patterson, U. Saini, B. Robinson, G. Newport, R. Murdock, J. Schlager, S. Hussain, and S. Ali, "Expression of genes related to oxidative stress in the mouse brain after exposure to silver-25 nanoparticles," *Toxicology letters*, vol. 187, no. 1, pp. 15–21, 2009.

[218] D. Riva, C. Njiokiktjien, and S. Bulgheroni, *Brain Lesion Localization and Developmental Functions: Frontal Lobes, Limbic System, Visuocognitive System: Remembering Ans Hey*, vol. 25. John Libbey Eurotext, 2012.

[219] L. Braydich-Stolle, S. Hussain, J. J. Schlager, and M.-C. Hofmann, "In vitro cytotoxicity of nanoparticles in mammalian germline stem cells," *Toxicological sciences*, vol. 88, no. 2, pp. 412–419, 2005.

[220] A. Burd, C. H. Kwok, S. C. Hung, H. S. Chan, H. Gu, W. K. Lam, and L. Huang, "A comparative study of the cytotoxicity of silver-based dressings

in monolayer cell, tissue explant, and animal models," *Wound repair and regeneration*, vol. 15, no. 1, pp. 94–104, 2007.

[221] S. Hussain, K. Hess, J. Gearhart, K. Geiss, and J. Schlager, "In vitro toxicity of nanoparticles in brl 3a rat liver cells," *Toxicology in vitro*, vol. 19, no. 7, pp. 975–983, 2005.

[222] S. M. Hussain, A. K. Javorina, A. M. Schrand, H. M. Duhart, S. F. Ali, and J. J. Schlager, "The interaction of manganese nanoparticles with pc-12 cells induces dopamine depletion," *Toxicological Sciences*, vol. 92, no. 2, pp. 456–463, 2006.

[223] M. Ahamed, M. A. Siddiqui, M. J. Akhtar, I. Ahmad, A. B. Pant, and H. A. Alhadlaq, "Genotoxic potential of copper oxide nanoparticles in human lung epithelial cells," *Biochemical and biophysical research communications*, vol. 396, no. 2, pp. 578–583, 2010.

[224] Y. Liu, W. Guan, G. Ren, and Z. Yang, "The possible mechanism of silver nanoparticle impact on hippocampal synaptic plasticity and spatial cognition in rats," *Toxicology letters*, vol. 209, no. 3, pp. 227–231, 2012.

[225] N. Li, C. Sioutas, A. Cho, D. Schmitz, C. Misra, J. Sempf, M. Wang, T. Oberley, J. Froines, and A. Nel, "Ultrafine particulate pollutants induce oxidative stress and mitochondrial damage.," *Environmental health perspectives*, vol. 111, no. 4, p. 455, 2003.

[226] S. R. Saptarshi, A. Duschl, and A. L. Lopata, "Interaction of nanoparticles with proteins: relation to bio-reactivity of the nanoparticle," *Journal of nanobiotechnology*, vol. 11, no. 1, p. 1, 2013.

[227] W. Lu, D. Senapati, S. Wang, O. Tovmachenko, A. K. Singh, H. Yu, and P. C. Ray, "Effect of surface coating on the toxicity of silver nanomaterials on human skin keratinocytes," *Chemical physics letters*, vol. 487, no. 1, pp. 92–96, 2010.

[228] Y. Sara, M. G. Mozhayeva, X. Liu, and E. T. Kavalali, "Fast vesicle recycling supports neurotransmission during sustained stimulation at hippocampal synapses," *The Journal of neuroscience*, vol. 22, no. 5, pp. 1608–1617, 2002.

[229] M. Rai, A. Yadav, and A. Gade, "Silver nanoparticles as a new generation of antimicrobials," *Biotechnology advances*, vol. 27, no. 1, pp. 76–83, 2009.

[230] F. Mafuné, J.-y. Kohno, Y. Takeda, T. Kondow, and H. Sawabe, "Formation of gold nanoparticles by laser ablation in aqueous solution of surfactant," *The Journal of Physical Chemistry B*, vol. 105, no. 22, pp. 5114–5120, 2001.

[231] S. E. Gratton, P. A. Ropp, P. D. Pohlhaus, J. C. Luft, V. J. Madden, M. E. Napier, and J. M. DeSimone, "The effect of particle design on cellular internalization pathways," *Proceedings of the National Academy of Sciences*, vol. 105, no. 33, pp. 11613–11618, 2008.

[232] A. Nel, T. Xia, L. Mädler, and N. Li, "Toxic potential of materials at the nanolevel," *science*, vol. 311, no. 5761, pp. 622–627, 2006.

[233] P. AshaRani, G. Low Kah Mun, M. P. Hande, and S. Valiyaveettil, "Cytotoxicity and genotoxicity of silver nanoparticles in human cells," *ACS nano*, vol. 3, no. 2, pp. 279–290, 2008.

[234] J. Panyam, W.-Z. Zhou, S. Prabha, S. K. Sahoo, and V. Labhasetwar, "Rapid endo-lysosomal escape of poly (dl-lactide-co-glycolide) nanoparticles: implications for drug and gene delivery," *The FASEB Journal*, vol. 16, no. 10, pp. 1217–1226, 2002.

[235] J. Rejman, V. Oberle, I. S. Zuhorn, and D. Hoekstra, "Size-dependent internalization of particles via the pathways of clathrin-and caveolae-mediated endocytosis," *Biochemical Journal*, vol. 377, no. 1, pp. 159–169, 2004.

[236] K. Kawata, M. Osawa, and S. Okabe, "In vitro toxicity of silver nanoparticles at noncytotoxic doses to hepg2 human hepatoma cells," *Environmental science & technology*, vol. 43, no. 15, pp. 6046–6051, 2009.

[237] T.-H. Kim, M. Kim, H.-S. Park, U. S. Shin, M.-S. Gong, and H.-W. Kim, "Size-dependent cellular toxicity of silver nanoparticles," *Journal of Biomedical Materials Research Part A*, vol. 100, no. 4, pp. 1033–1043, 2012.

[238] D. Riva, C. Njiokiktjien, and S. Bulgheroni, *Brain Lesion Localization and Developmental Functions: Frontal Lobes, Limbic System, Visuocognitive System: Remembering Ans Hey*, vol. 25. John Libbey Eurotext, 2012.

[239] W. Ma, L. Jing, A. Valladares, S. L. Mehta, Z. Wang, P. A. Li, and J. J. Bang, "Silver nanoparticle exposure induced mitochondrial stress, caspase-3 activation and cell death: amelioration by sodium selenite," *International journal of biological sciences*, vol. 11, no. 8, p. 860, 2015.

[240] P. Gopinath, S. K. Gogoi, P. Sanpui, A. Paul, A. Chattopadhyay, and S. S. Ghosh, "Signaling gene cascade in silver nanoparticle induced apoptosis," *Colloids and Surfaces B: Biointerfaces*, vol. 77, no. 2, pp. 240–245, 2010.

[241] M. Rahman, J. Wang, T. Patterson, U. Saini, B. Robinson, G. Newport, R. Murdock, J. Schlager, S. Hussain, and S. Ali, "Expression of genes related to oxidative stress in the mouse brain after exposure to silver-25 nanoparticles," *Toxicology letters*, vol. 187, no. 1, pp. 15–21, 2009.

[242] C.-C. Huang, R. S. Aronstam, D.-R. Chen, and Y.-W. Huang, "Oxidative stress, calcium homeostasis, and altered gene expression in human lung epithelial cells exposed to zno nanoparticles," *Toxicology in vitro*, vol. 24, no. 1, pp. 45–55, 2010.

[243] A. M. Knaapen, P. J. Borm, C. Albrecht, and R. P. Schins, "Inhaled particles and lung cancer. part a: Mechanisms," *International Journal of Cancer*, vol. 109, no. 6, pp. 799–809, 2004.

[244] A. Manke, L. Wang, and Y. Rojanasakul, "Mechanisms of nanoparticle-induced oxidative stress and toxicity," *BioMed research international*, vol. 2013, 2013.

[245] K. Donaldson and C. L. Tran, "Inflammation caused by particles and fibers," *Inhalation toxicology*, vol. 14, no. 1, pp. 5–27, 2002.

[246] G. Oberdörster, A. Maynard, K. Donaldson, V. Castranova, J. Fitzpatrick, K. Ausman, J. Carter, B. Karn, W. Kreyling, D. Lai, *et al.*, "Principles for characterizing the potential human health effects from exposure to nanomaterials: elements of a screening strategy," *Particle and fibre toxicology*, vol. 2, no. 1, p. 8, 2005.

[247] A. Nel, T. Xia, L. Mädler, and N. Li, "Toxic potential of materials at the nanolevel," *science*, vol. 311, no. 5761, pp. 622–627, 2006.

[248] B. Fubini and A. Hubbard, "Reactive oxygen species (ros) and reactive nitrogen species (rns) generation by silica in inflammation and fibrosis," *Free Radical Biology and Medicine*, vol. 34, no. 12, pp. 1507–1516, 2003.

[249] A. M. Knaapen, P. J. Borm, C. Albrecht, and R. P. Schins, "Inhaled particles and lung cancer. part a: Mechanisms," *International Journal of Cancer*, vol. 109, no. 6, pp. 799–809, 2004.

[250] M. R. Wilson, J. H. Lightbody, K. Donaldson, J. Sales, and V. Stone, "Interactions between ultrafine particles and transition metals in vivo and in vitro," *Toxicology and applied pharmacology*, vol. 184, no. 3, pp. 172–179, 2002.

[251] M. Valko, C. Rhodes, J. Moncol, M. Izakovic, and M. Mazur, "Free radicals, metals and antioxidants in oxidative stress-induced cancer," *Chemico-biological interactions*, vol. 160, no. 1, pp. 1–40, 2006.

[252] C. Sioutas, R. J. Delfino, and M. Singh, "Exposure assessment for atmospheric ultrafine particles (ufps) and implications in epidemiologic research," *Environmental health perspectives*, pp. 947–955, 2005.

[253] T. Xia, M. Kovochich, J. Brant, M. Hotze, J. Sempf, T. Oberley, C. Sioutas, J. I. Yeh, M. R. Wiesner, and A. E. Nel, "Comparison of the abilities of ambient and manufactured nanoparticles to induce cellular toxicity according to an oxidative stress paradigm," *Nano letters*, vol. 6, no. 8, pp. 1794–1807, 2006.

[254] Y.-H. Hsin, C.-F. Chen, S. Huang, T.-S. Shih, P.-S. Lai, and P. J. Chueh, "The apoptotic effect of nanosilver is mediated by a ros-and jnk-dependent mechanism involving the mitochondrial pathway in nih3t3 cells," *Toxicology letters*, vol. 179, no. 3, pp. 130–139, 2008.

[255] P. J. Borm, D. Robbins, S. Haubold, T. Kuhlbusch, H. Fissan, K. Donaldson, R. Schins, V. Stone, W. Kreyling, J. Lademann, *et al.*, "The potential risks of nanomaterials: a review carried out for ecetoc," *Particle and fibre toxicology*, vol. 3, no. 1, p. 11, 2006.

[256] H.-J. Eom and J. Choi, "p38 mapk activation, dna damage, cell cycle arrest and apoptosis as mechanisms of toxicity of silver nanoparticles in jurkat t cells," *Environmental science & technology*, vol. 44, no. 21, pp. 8337–8342, 2010.

[257] G. Lenaz, "The mitochondrial production of reactive oxygen species: mechanisms and implications in human pathology," *IUBMB life*, vol. 52, no. 3-5, pp. 159–164, 2001.

[258] P. Manna, M. Ghosh, J. Ghosh, J. Das, and P. C. Sil, "Contribution of nano-copper particles to in vivo liver dysfunction and cellular damage: Role of iκbα/nf-κb, mapks and mitochondrial signal," *Nanotoxicology*, vol. 6, no. 1, pp. 1–21, 2012.

[259] B. Fahmy and S. A. Cormier, "Copper oxide nanoparticles induce oxidative stress and cytotoxicity in airway epithelial cells," *Toxicology In Vitro*, vol. 23, no. 7, pp. 1365–1371, 2009.

[260] Y.-S. Kim, K.-K. Kim, S.-M. Shin, S.-M. Park, and S.-S. Hah, "Comparative toxicity studies of ultra-pure ag, au, co, and cu nanoparticles generated by laser ablation in biocompatible aqueous solution," *Bulletin of the Korean Chemical Society*, vol. 33, no. 10, pp. 3265–3268, 2012.

[261] B. M. Prabhu, S. F. Ali, R. C. Murdock, S. M. Hussain, and M. Srivatsan, "Copper nanoparticles exert size and concentration dependent toxicity on somatosensory neurons of rat," *Nanotoxicology*, vol. 4, no. 2, pp. 150–160, 2010.

[262] P. Xu, J. Xu, S. Liu, G. Ren, and Z. Yang, "In vitro toxicity of nano-sized copper particles in pc12 cells induced by oxidative stress," *Journal of Nanoparticle Research*, vol. 14, no. 6, p. 906, 2012.

[263] D. Laha, A. Pramanik, J. Maity, A. Mukherjee, P. Pramanik, A. Laskar, and P. Karmakar, "Interplay between autophagy and apoptosis mediated by copper oxide nanoparticles in human breast cancer cells mcf7," *Biochimica et Biophysica Acta (BBA)-General Subjects*, vol. 1840, no. 1, pp. 1–9, 2014.

[264] M. A. Siddiqui, H. A. Alhadlaq, J. Ahmad, A. A. Al-Khedhairy, J. Musarrat, and M. Ahamed, "Copper oxide nanoparticles induced mitochondria mediated apoptosis in human hepatocarcinoma cells," *PloS one*, vol. 8, no. 8, p. e69534, 2013.

[265] A. A. Alshatwi, P. V. Subbarayan, E. Ramesh, A. A. Al-Hazzani, M. A. Alsaif, and A. A. Alwarthan, "Aluminium oxide nanoparticles induce mitochondrial-mediated oxidative stress and alter the expression of antioxidant enzymes in human mesenchymal stem cells," *Food Additives & Contaminants: Part A*, vol. 30, no. 1, pp. 1–10, 2013.

[266] C. Betzen, R. White, C. M. Zehendner, E. Pietrowski, B. Bender, H. J. Luhmann, and C. R. Kuhlmann, "Oxidative stress upregulates the nmda receptor on cerebrovascular endothelium," *Free Radical Biology and Medicine*, vol. 47, no. 8, pp. 1212–1220, 2009.

[267] L. Li, Y. Shou, J. L. Borowitz, and G. E. Isom, "Reactive oxygen species mediate pyridostigmine-induced neuronal apoptosis: involvement of muscarinic and nmda receptors," *Toxicology and applied pharmacology*, vol. 177, no. 1, pp. 17–25, 2001.

Appendix A

Appendix A Chapter 3

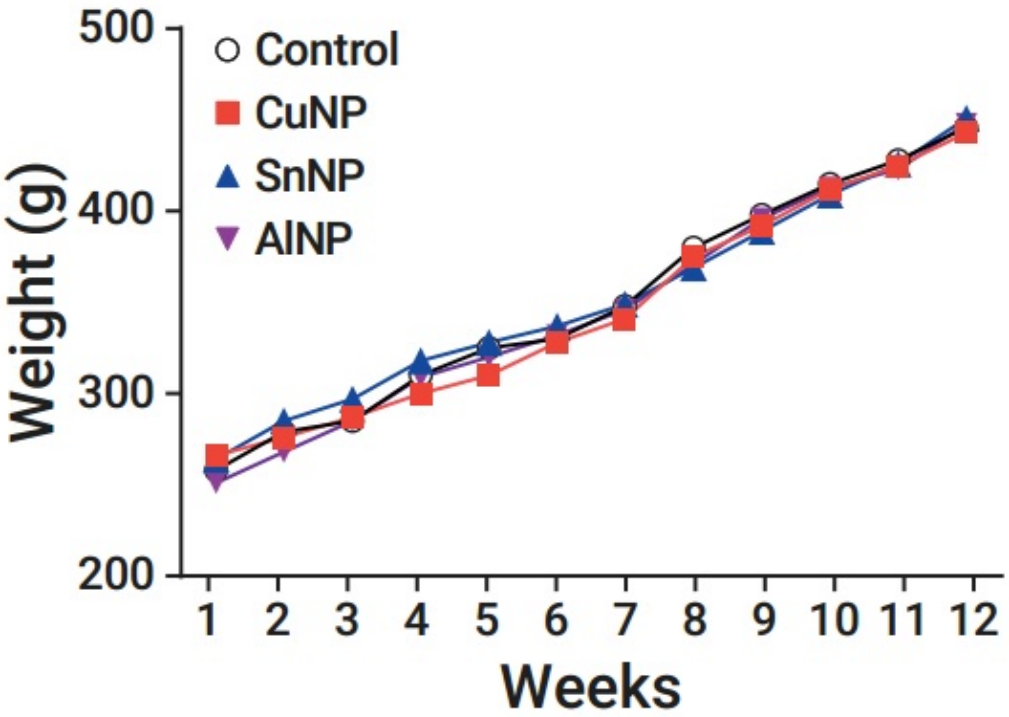

Figure A.1: The weight of rats in CuNP, SnNP and AlNP group was not affected from the nanoparticle exposure throughout the exposure to nanoparticles.

Table A.1: Primers used in cDNA Synthesis and qPCR experiments (RP: reverse primer, FP: forward primer

Gene name and NCBI accession number	Sequence	Tm values	Distilled water added for 100μM stock	Product Length
GAPDH (NM_001289745.1) FP	5'TCCCATTCTTCCACCTTT3'	51°C	209 μl	92 bp
GAPDH (NM_001289745.1) RP	5'TAGCCATATTCATTGTCATACC3'	55°C	212 μl	
NMDAR1 (NM_007327.3) FP	5'GCAGAACGTTTCCCTGTCCA3'	61°C	242 μl	112 bp
NMDAR1 (NM_007327.3) RP	5'CCCCTGCCATGTTCTCAAAA3'	61°C	212 μl	
NMDAR2a (NM_001134407.2) FP	5'CAGAGACCCCGCTACACAC3'	61°C	282 μl	150 bp
NMDAR2a (NM_001134407.2) RP	5'TGCCCACCTTTTCCCACTC3'	59°C	208 μl	

Table A.2: RNA concentrations and volumes used in cDNA Synthesis

Sample	Concentration (ng/μl)	Used volume for cDNA synthesis (μl)	Final concentration of RNA (ng)
C1	1014.60	0.98	1000
C2	997.00	1.00	1000
C3	766.10	1.30	1000
C4	813.00	1.24	1000
C5	401.20	2.50	1000
CuNP1	361.80	2.76	1000
CuNP2	121.60	4.12	500
CuNP3	250.70	3.98	1000
CuNP4	225.20	4.44	1000
CuNP5	80.1	6.24	500
SnNP1	317.80	3.14	1000
SnNP2	603.5	1.66	1000
SnNP3	757.90	1.32	1000
SnNP4	526,60	1.90	1000
SnNP5	465,80	2.16	1000
AlNP1	388.20	2.58	1000
AlNP2	242.80	4.12	1000
AlNP3	533.00	1.88	1000
AlNP4	504.80	1.98	1000
AlNP5	420.00	2.38	1000

Table A.3: RNA concentrations and A_{260}/A_{280} and $A_{260}/A_{230}0$ ratios of RNA samples isolated from hippocampus tissue of controls and nanoparticle exposed groups.

Sample	**Concentration (ng/μl)**	A_{260}/A_{280} **ratio**	A_{260}/A_{230} **ratio**
C1	1014.60	2.01	1.08
C2	997.00	2.04	1.38
C3	766.10	2.02	1.26
C4	813.00	2.04	1.30
C5	401.20	2.06	1.37
CuNP1	361.80	2.04	1.04
CuNP2	121.60	2.07	0.58
CuNP3	250.70	2.14	0.56
CuNP4	225.20	2.07	0.92
CuNP5	80.10	2.05	0.53
SnNP1	317.80	2.08	1.09
SnNP2	603.5	2.09	1.58
SnNP3	757.90	2.09	1.73
SnNP4	526.60	2.10	1.57
SnNP5	465.80	2.07	1.71
AlNP1	388.20	2.09	1.61
AlNP2	242.80	2.04	0.98
AlNP3	533.00	2.08	1.57
AlNP4	504.80	2.11	2.06
AlNP5	420.00	2.08	1.63

Table A.4: Concentrations of proteins isolated from hippocampus tissue of controls and nanoparticle exposed groups.

Sample	**Cytosolic Protein Concentration (mg/ml)**	**Membrane-associated Protein Concentration (ng/μl)**
C7	2.84	3.16
C8	3.16	3.95
C9	0.70	0.50
CuNP6	2.45	3.43
CuNP7	0.86	0.96
CuNP9	1.02	2.38
SnNP6	2.29	3.07
SnNP7	2.53	3.60
SnNP8	2.15	2.95
AlNP6	2.21	3.43
AlNP7	2.29	3.25
AlNP8	1.67	3.37

Appendix B

Appendix B Chapter 4

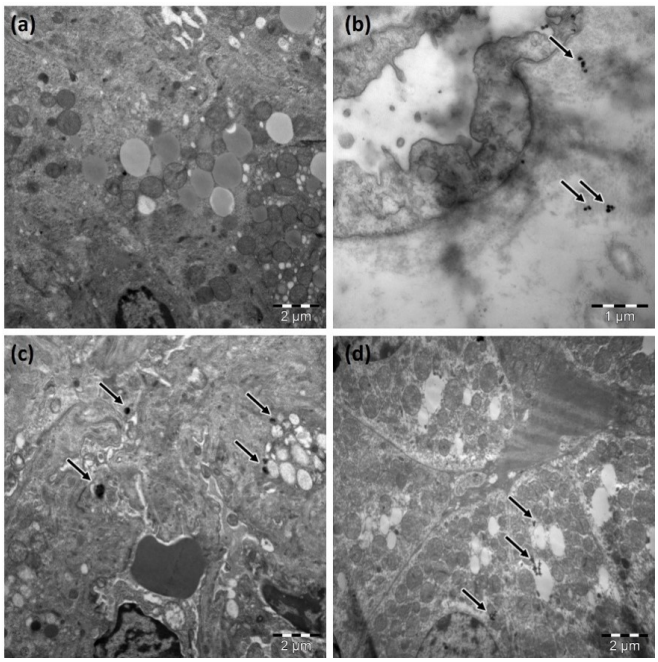

Figure B.1: TEM image of adrenal glands of (a) control, (b) CuNP, (c) SnNP, and (d) AlNP groups. The arrows indicate the nanoparticles in adrenal gland tissue samples. Nanoparticles were determined in all of the nanoparticle-exposed groups.

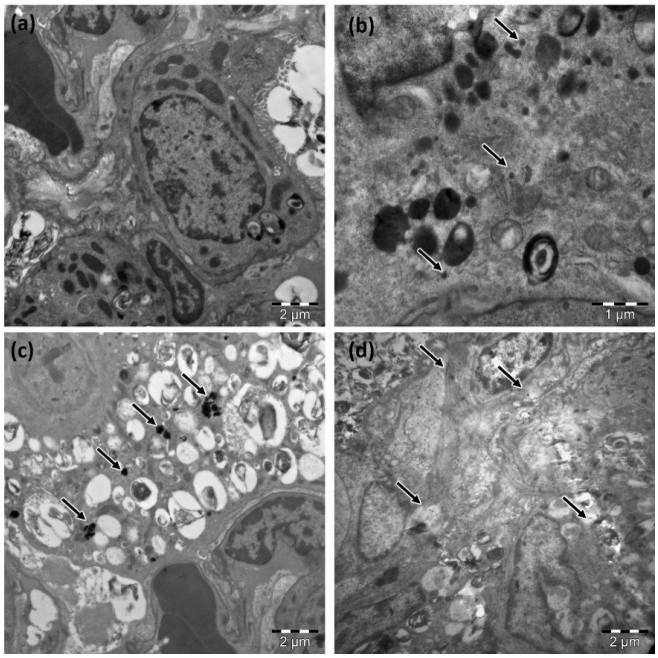

Figure B.2: TEM image of lungs of (a) control, (b) CuNP, (c) SnNP, and (d) AlNP groups. The arrows indicate the nanoparticles in lung tissue samples. Nanoparticles were determined in all of the nanoparticle-exposed groups.

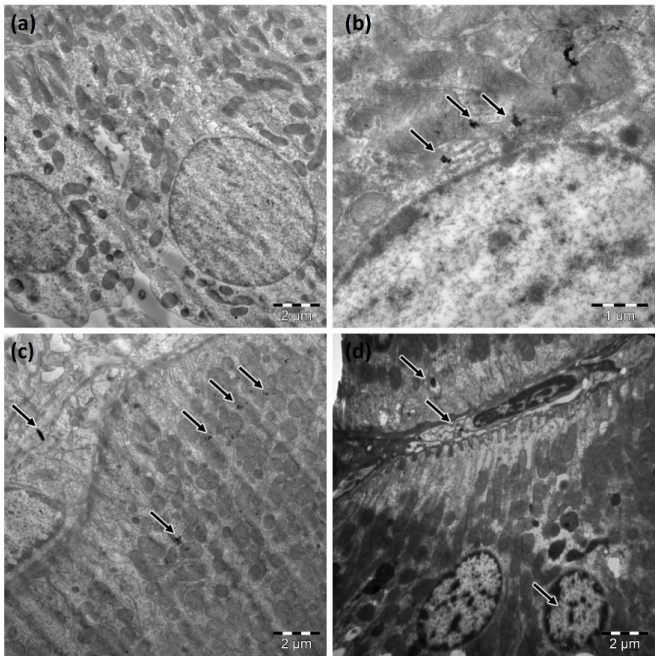

Figure B.3: TEM image of kidneys of (a) control, (b) CuNP, (c) SnNP, and (d) AlNP groups. The arrows indicate the nanoparticles in kidney tissue samples. Nanoparticles were determined in all of the nanoparticle-exposed groups.

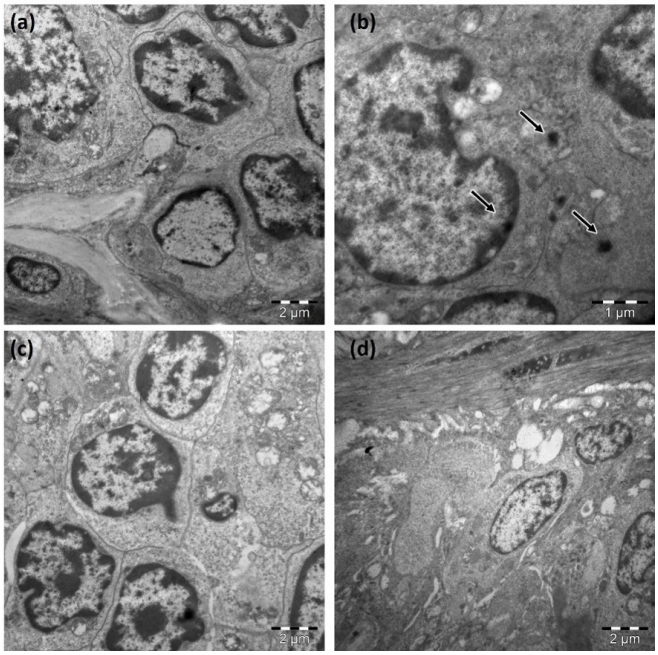

Figure B.4: TEM image of spleen of (a) control, (b) CuNP, (c) SnNP, and (d) AlNP groups. The arrows indicate the nanoparticles in spleen tissue samples. Nanoparticles were determined only in CuNP-exposed group.

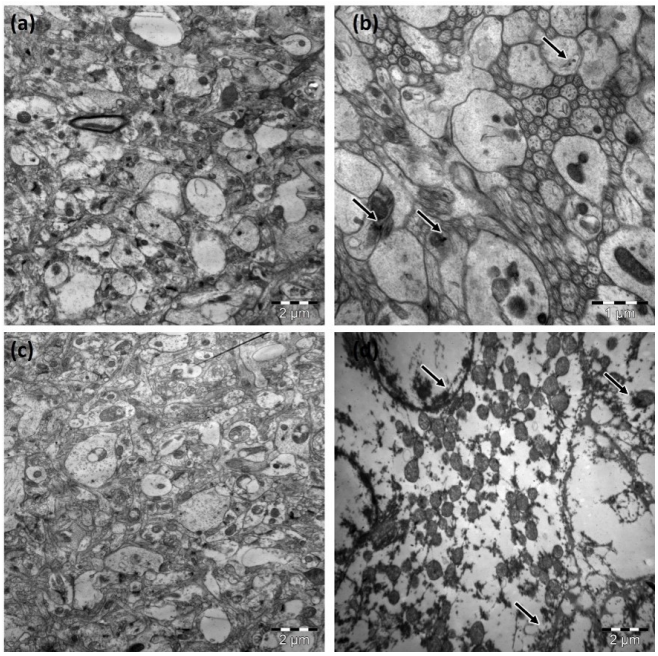

Figure B.5: TEM image of frontal cortex of (a) control, (b) CuNP, (c) SnNP, and (d) AlNP groups. The arrows indicate the nanoparticles in frontal cortex tissue samples. Nanoparticles were determined only in CuNP- and AlNP-exposed groups.

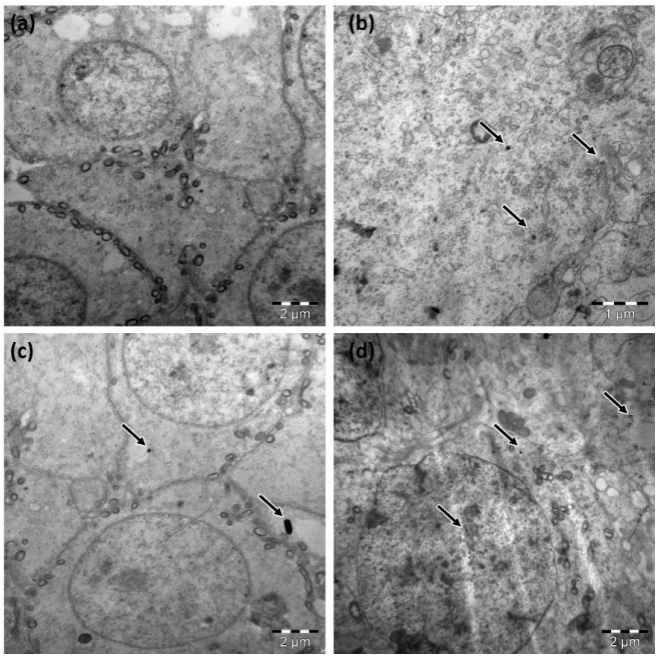

Figure B.6: TEM image of testis of (a) control, (b) CuNP, (c) SnNP, and (d) AlNP groups. The arrows indicate the nanoparticles in testis tissue samples. Nanoparticles were determined in all of the nanoparticle-exposed groups.

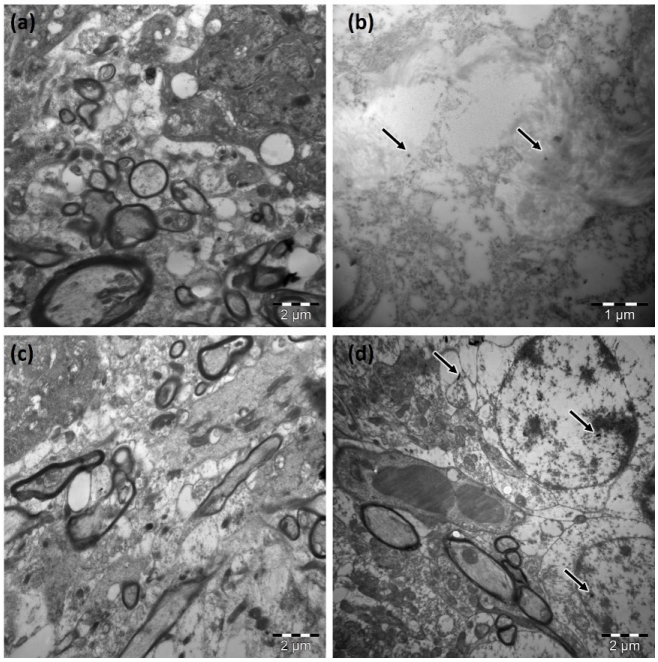

Figure B.7: TEM image of cerebellum of (a) control, (b) CuNP, (c) SnNP, and (d) AlNP groups. The arrows indicate the nanoparticles in cerebellum tissue samples. Nanoparticles were determined only in CuNP- and AlNP-exposed groups.

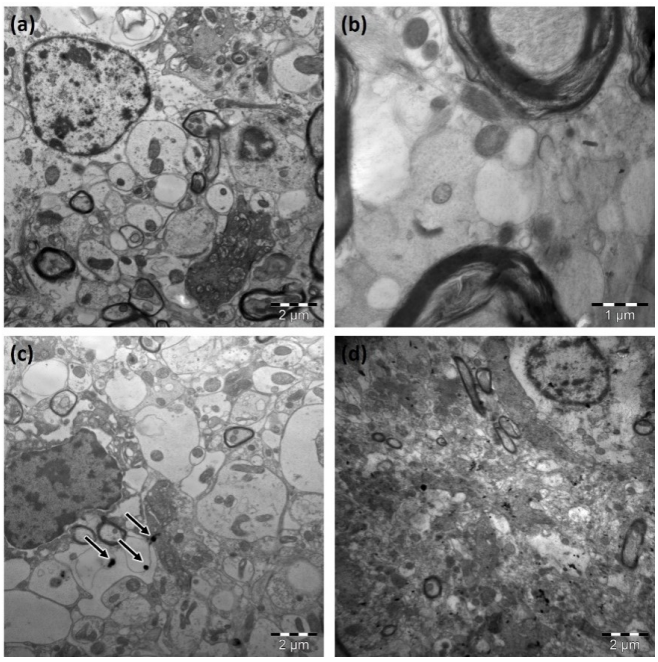

Figure B.8: TEM image of hindbrain of (a) control, (b) CuNP, (c) SnNP, and (d) AlNP groups. The arrows indicate the nanoparticles in hindbrain tissue samples. Nanoparticles were determined only in SnNP-exposed group.

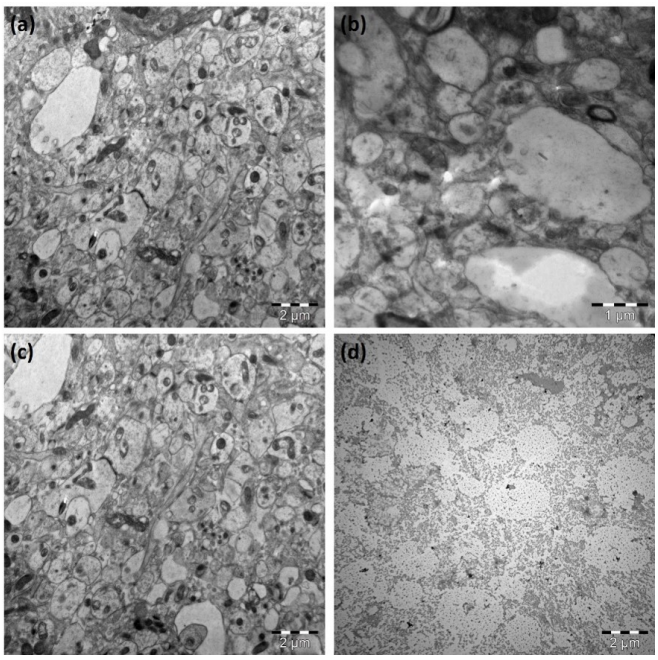

Figure B.9: TEM image of hippocampus of (a) control, (b) CuNP, (c) SnNP, and (d) AlNP groups. The arrows indicate the nanoparticles in hippocampus tissue samples. Nanoparticles were not determined in any of the nanoparticle-exposed groups.

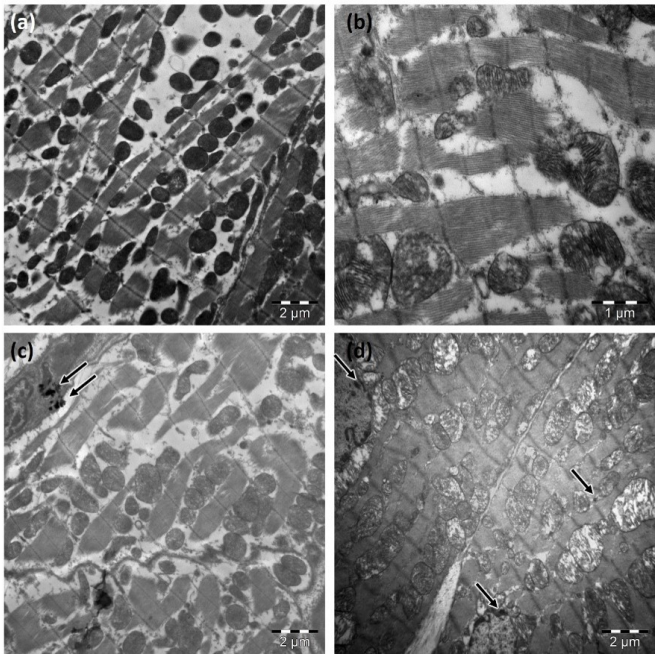

Figure B.10: TEM image of heart of (a) control, (b) CuNP, (c) SnNP, and (d) AlNP groups. The arrows indicate the nanoparticles in heart tissue samples. Nanoparticles were determined only in SnNP- and AlNP-exposed groups.

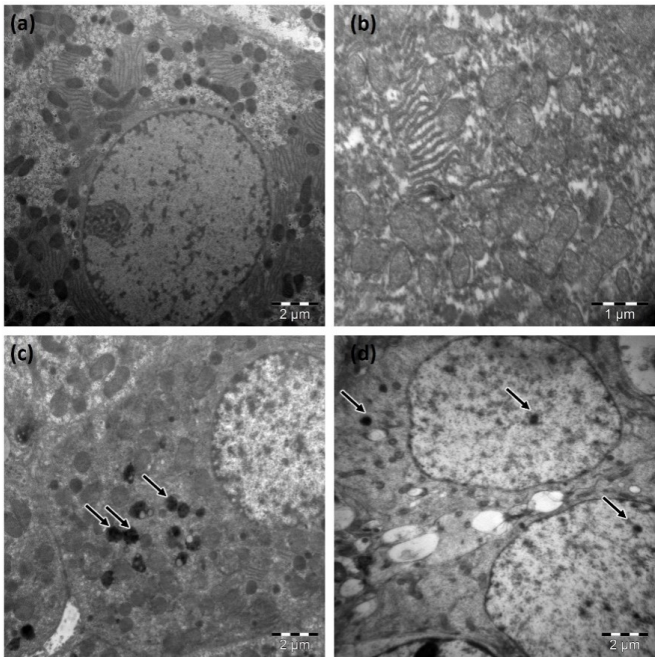

Figure B.11: TEM image of liver of (a) control, (b) CuNP, (c) SnNP, and (d) AlNP groups. The arrows indicate the nanoparticles in liver tissue samples. Nanoparticles were determined only in SnNP- and AlNP-exposed groups.

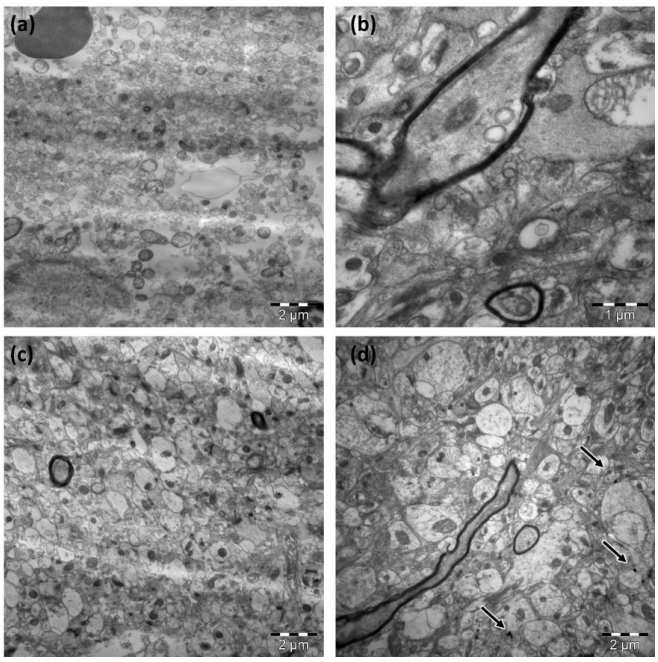

Figure B.12: TEM image of occipital lobe of (a) control, (b) CuNP, (c) SnNP, and (d) AlNP groups. The arrows indicate the nanoparticles in occipital lobe tissue samples. Nanoparticles were determined only in SnNP- and AlNP-exposed groups.

Table B.1: The concentrations of the copper, tin and aluminum in the rat organs exposed to CuNP, SnNP and AlNP in the laser material processing real time exposure setup.

	Copper (μg/g)		**Tin (μg/g)**		**Aluminum (μg/g)**	
	Control	**CuNP exposed**	**Control**	**SnNP exposed**	**Control**	**AlNP exposed**
Heart	0.64 ± 0.02	0.76 ± 0.04 *	0	0.04 ± 0.02	0	0.58 ± 0.16 ****
Lung	0.19 ± 0.02	1.85 ± 0.24 ****	0	471.26 ± 60.30 ****	0	123.44 ± 2.99 ****
Kidney	1.08 ± 0.07	1.03 ± 0.08	0	0.09 ± 0.01 ****	0	0.18 ± 0.08 *
Adrenal Glands	0.18 ± 0.20	0.17 ± 0.03	0	0.03 ± 0.01 **	0	0.77 ± 0.45 *
Liver	0.59 ± 0.02	1.49 ± 0.31 **	0	0.04 ± 0.01 **	0	0.06 ± 0.03 *
Testis	0.25 ± 0.02	0.29 ± 0.03	0	0.02 ± 0.00 *	0	0.08 ± 0.05
Spleen	0.19 ± 0.008	0.22 ± 0.01	0	0.06 ± 0.01 *	0	0.13 ± 0.02 ***
Intestine	3.39 ± 0.25	3.55 ± 1.05	0	0.02 ± 0.00	0.27 ± 0.01	0.26 ± 0.12
Olfactory bulb	1.38 ± 0.17	2.69 ± 0.80	0	0.06 ± 0.00 ****	0	0
Hippocampus	0.30 ± 0.	0.29 ± 0.02	0	0.01 ± 0.00	0	0.39 ± 0.14 **
Cerebellum	0.31 ± 0.01	0.39 ± 0.04	0	0.01 ± 0.00 **	0	0.18 ± 0.10 *
Hindbrain	0.25 ± 0.02	0.36 ± 0.07	0	0.01 ± 0.00 *	0	0.13 ± 0.06 *
Frontal Cortex	0.29 ± 0.01	0.33 ± 0.01 *	0	0.02 ± 0.00 **	0	0.20 ± 0.09 *
Occipital Lobe	0.26 ± 0.01	0.33 ± 0.02	0	0.04 ± 0.01 *	0	0.22 ± 0.17 **
Plasma	6.65 ± 0.14	9.48 ± 0.54 *	0.14 ± 0.03	0.20 ± 0.05	3.01 ± 0.26	2.78 ± 0.12

$^{*}p<0.05$, $^{**}p<0.01$, $^{***}p<0.005$, $^{****}p<0.001$ vs control

Appendix C

Appendix C Chapter 5

Table C.1: RNA concentrations and volumes used in cDNA Synthesis

Sample	**Concentration (ng/μl)**	**Used Volume for cDNA Synthesis (μl)**	**Final Concentration of RNA (ng)**
V1	468.4	2.14	1000
V2	240.2	4.16	1000
V3	371.3	2.70	1000
CuNP1	420.5	2.38	1000
CuNP2	86.3	5.80	500
CuNP3	162.9	6.14	1000
SnNP1	143.8	6.96	1000
SnNP2	80.8	6.18	500
SnNP3	32.2	7.76	250
AlNP1	89.2	5.60	500
AlNP2	53.2	4.70	250
AlNP3	188.8	5.30	1000

Table C.2: RNA concentrations and A_{260}/A_{280} and A_{260}/A_{230} ratios of RNA samples isolated from hippocampus tissue of controls and nanoparticle exposed groups.

Sample	**Concentration (ng/μl)**	A_{260}/A_{280} **ratio**	A_{260}/A_{230} **ratio**
V1	468.40	2.03	1.52
V2	240.20	1.97	1.39
V3	371.30	1.99	1.72
CuNP1	420.50	1.95	2.05
CuNP2	86.30	1.84	1.34
CuNP3	162.90	1.84	0.99
SnNP1	143.80	1.86	0.95
SnNP2	80.80	1.74	0.78
SnNP3	32.20	1.70	0.69
AlNP1	89.20	1.83	0.81
AlNP2	53.20	1.66	0.49
AlNP3	188.80	1.86	1.11

Table C.3: Concentrations of isolated proteins from SH-SY5Y cells administered with CuNP, SnNP and AlNP

Sample	**Cytosolic Protein Concentration (mg/ml)**	**Membrane-associated Protein Concentration (ng/μl)**
V1	3,45	3,17
V2	2,53	1,69
V3	3,30	2,87
CuNP1	0,54	0,59
CuNP2	0,69	0,66
CuNP3	0,31	0,37
SnNP1	1,76	1,32
SnNP2	2,23	1,62
SnNP3	1,30	1,40
AlNP1	3,53	2,43
AlNP2	3,15	2,21
AlNP3	3,45	2,36